COSMIC EVOLUTION AND THE DARK SECTOR: A PFS SSP FOR THE SUBARU TELESCOPE

The Subaru Prime Focus Spectrograph (PFS) Collaboration
The full list of members can be found in the Appendix

ABSTRACT

We propose a large-scale survey with PFS to address fundamental and important questions in the dark sector (dark matter and dark energy) with significant implications for cosmology, galaxy evolution and the origin of the Milky Way Galaxy. The unique wide-field and massively-multiplexed spectroscopic capability of PFS will maintain and strengthen Subaru's world-leading role in cosmology and astronomy for the next decade. Our experienced team of Japanese and international astronomers has developed an ambitious 360 night survey to be undertaken over 5 years which fully exploits the unique capabilities of PFS to address outstanding questions relating to the history and fate of the Universe as well as the physical processes and role of dark matter in governing the assembly of galaxies including our Milky Way. We commit to fully reducing the data from this landmark survey and making it available to the global astronomical community in a timely manner.

1. INTRODUCTION

Multi-band imaging surveys in recent decades, such as those conducted by the Sloan Digital Sky Survey (York et al. 2000), the Hubble Space Telescope (Scoville et al. 2007) and Subaru's Hyper Suprime-Cam (HSC) imager (Aihara et al. 2018a), have led to enormous progress in our understanding of the Universe. These data have enabled detailed studies of gravitational lensing signals which trace the spatial distribution of dark matter (DM), and census studies of Galactic structures and high redshift galaxies. Together with other cosmological probes, precise measures have been made of the amount of both non-baryonic DM and the dark energy (DE) that propels the cosmic acceleration. However, neither of these two dark constituents is physically understood. Likewise, the standard picture of galaxy evolution based on the hierarchical assembly of DM halos cannot fully explain observations of the evolving population of galaxies and the rich diversity of their present-day morphologies. While the dark sector clearly governs cosmic history, its role is not yet fully understood.

As the first massively-multiplexed spectrograph on a large aperture telescope, Prime Focus Spectrograph (PFS) on the 8.2m Subaru Telescope offers an unique opportunity to address these fundamental questions. Exploiting wide field catalogs produced by HSC, precise redshifts from PFS will chart large-scale structures and the spectra will reveal detailed galaxy properties over cosmic time. Radial velocities, metallicities and physical properties of faint stars in both the Milky Way and its nearest neighbor, the Andromeda spiral, will complement this story through more detailed measures of DM on smaller scales.

In the following we first describe scientific motivation, key questions and competitiveness of the PFS-SSP program in Sections 2–6 (referred to as "Part I") and then describe the technical feasibility, survey design and management plan for carrying out our program in Sections 7–10 ("Part II").

2. SUMMARY OF PFS-SSP PROGRAMS

Here we propose an ambitious "Subaru Strategic Program", a 360-night survey to be undertaken over 5 years with PFS (hereafter PFS-SSP) that promises a revolution in our understanding of the Universe. The proposal comprises three interlocking science themes – Cosmology, Galaxy Evolution, and Galactic Archaeology – which collectively address the over-arching theme of the role of the dark sector in cosmic evolution (see Figure 1).

The PFS Cosmology program will deliver four million redshifts of [O II] emitting galaxies over about 1100 deg^2 to make precise measurements of angular diameter distances and the cosmic expansion rate over the redshift range $0.6 \lesssim z \lesssim 2.4$, thereby constraining the nature of DE and the curvature of the Universe. The 3D clustering of galaxies and redshift-space distortions due to their peculiar velocities will determine the sum of neutrino masses to the precision of $\sigma(\sum m_\nu) \simeq 0.02$ eV.

The PFS Galactic Archaeology program will provide unprecedented datasets of chemical abundances and radial velocities for stars in various environments in the Milky Way, its satellite galaxies and the halo of Andromeda (M31) to determine the role of DM in the assembly history of these galaxies. Velocity dispersion and chemical abundance profiles for a sample of nearby DM-dominated satellites will constrain whether their puzzling cores arise from DM that is self-interacting, warm or wave-like (fuzzy), or are due to baryonic feedback.

Emission and absorption line data from the PFS Galaxy Evolution program will delineate the assembly history of galaxies for a nearly stellar-mass limited sample, comparable in size to that achieved locally by SDSS, in the formative era $1 \lesssim z \lesssim 2$. Spectra of fainter star-forming galaxies at $2 \lesssim z \lesssim 5$ will establish the connection to DM halos in the young universe including reconstruction of the associated 3D large-scale distribution of HI gas in the intergalactic medium (IGM) at $z \sim 2.5$. Large samples of Lyman-α emitters over $5 \lesssim z \lesssim 7$ selected from existing HSC narrow-band imaging data will probe the IGM at the end of cosmic reionization. Collectively the PFS Galaxy Evolution survey will reveal, for the first time, the interplay between the IGM and galaxy assembly. In summary the three themes of the PFS-SSP program will test the standard ΛCDM model in a comprehensive fashion from kpc to Gpc scales and cosmic epochs from the present to the end of cosmic reionization at $z \sim 7$.

Our PFS SSP survey strategy will select its spectroscopic targets from deep multi-color imaging taken with HSC. The unique instrumental combination of PFS+HSC will allow additional synergistic scientific opportunities. For example, weak

	Testing ΛCDM	Assembly history of galaxies	Importance of IGM
CO	• Nature & role of neutrinos • Expansion rate via BAO up to z=2.4 • PFS+HSC tests of GR • Curvature of space: Ω_K • Primordial power spectrum	• PFS+HSC synergy • Absorption probes with PFS/SDSS QSOs around PFS/HSC host galaxies	• Search for emission from stacked spectra
GA	• Nature of DM (dSphs) • Structure of MW dark halo	• Stellar kinematics and chemical abundances – MW & M31 assembly history	• dSphs as relic probe of reionization feedback • Past massive star IMF from element abundances
GE	• Small-scale tests of structure growth	• Galaxy-halo connection: $M_*/M_{\rm halo}$ • Outflows & inflows of gas • Environment-dependent evolution	• Physics of cosmic reionization via LAEs & 21cm studies • Tomography of gas & DM

Figure 1. An illustration summarizes the interlocking nature of the three themes – Cosmology (CO), Galactic Archaeology (GA) and Galaxy Evolution (GE) – in addressing the scientific objectives of PFS-SSP program.

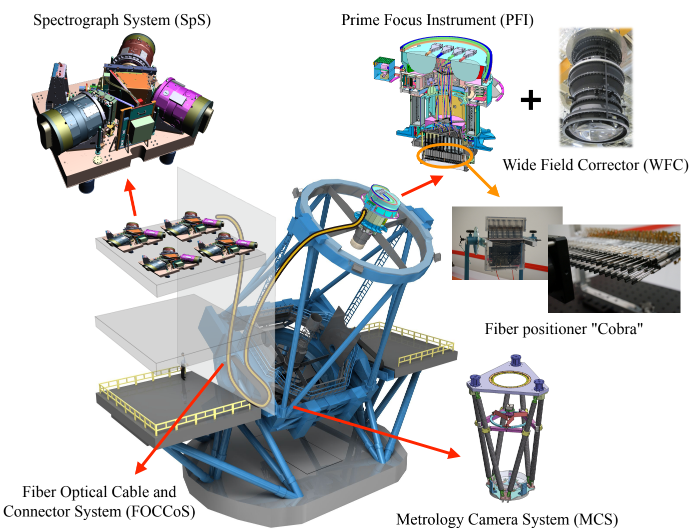

Figure 2. A schematic overview of PFS subsystems (see text for details).

lensing measures and photometric redshifts from HSC will chart, respectively, the DM distribution and associated faint galaxies with PFS survey galaxies of known redshift. Our carefully designed survey uses a sophisticated simulation tool to optimize the fiber allocation strategy taking into account the different visibilities, target surface densities and exposure times of the various targets, maximizing survey efficiency via a single coherent strategy. Our team comprises an international consortium including experienced astronomers drawn from the Japanese community, ASIAA in Taiwan, Caltech/JPL, Princeton University, the Johns Hopkins University, Laboratoire d'Astrophysique de Marseille (LAM), the Brazilian PFS Participant Consortium, MPA/MPE in Germany, the Chinese PFS Participant Consortium, and the North-East Participation Group in the USA.

3. THE INSTRUMENTS

The 8.2m Subaru Telescope has the largest prime focus field of any telescope of its class. Following the success of HSC, a wide-field optical imager, PFS – a massively multiplexed, optical and near-infrared (NIR) spectrometer – represents the next logical scientific step forward. Its focal plane is equipped with 2394 reconfigurable fibers distributed in the 1.38-degree wide hexagonal field of view. The spectrograph system covers a wide wavelength range, from 380nm to 1260nm in a single exposure. PFS and HSC share the same wide field corrector and collectively form the Subaru Measurement of Images and Redshifts (SuMIRe) project (PI: H. Murayama).

The PFS instrument is comprised of subsystems introduced below. Schematically, light from celestial objects is fed to fibers configured at the prime focus and transmitted via fiber cables to the spectrographs in the telescope enclosure building, and the spectra are recorded on optical and NIR detectors (see Figure 2).

The **Prime Focus Instrument** (PFI) comprises the fiber positioner system, science & fiducial fibers, Acquisition & Guide (AG) cameras, and a calibration system. The fiber positioner system consists of 42 modules each of which includes 57 "Cobra" rotary actuators populated with science fibers. Each science fiber is tipped with a plano-concave microlens to increase the focal ratio of the input beam.

The **Metrology Camera System** (MCS) is installed at the Cassegrain focus of the telescope. As the fiber positioners have no encoders, an external system is required to ensure accurate positioning. MCS takes images of both science and fiducial fibers back-lit from the other side of prime focus, enabling closed-loop operation of the positioners.

The **Spectrograph System** (SpS) includes a fiber feed, collimator, camera optics, dewars and detectors. The divergent beams from the science fibers aligned along slits are collimated and split into blue, red and NIR channels by two dichroic mirrors. The beams are then dispersed by VPH gratings and spectral images are formed on the detectors. A grating exchange mechanism allows a medium resolution option for stellar work in the red channel. There are four identical spectrograph modules each of which delivers ~600 spectral images.

The **Fiber System** (FS) consists of two short-fiber systems included in PFI and SpS respectively, and a long cable system is routed via the telescope to connect PFI to SpS via two sets of fiber connectors. One of these is at the telescope top end to allow PFS to be removed from the telescope, and the other is at SpS to ease its integration for operational and maintenance purposes. Table 1 summarizes the key characteristics of PFS.

The **Subaru Night Sky Spectrograph (SuNSS)** (not shown in Figure 2) is a pair of small (36mm) telescopes, each with a

Table 1
Instrumentation parameters

Prime Focus Instrument				
Field of view	∼ 1.38 deg (hexagonal - diameter of circumscribed circle)			
Field of view area	∼ 1.25 $\deg^2$			
Input f number to fiber	2.8			
Fiber core diameter[a]	127 μm (1.12 arcsec at the FoV center, 1.02 arcsec at the edge)			
Positioner pitch	8 mm (90.4 arcsec at the FoV center, 82.4 arcsec at the edge)			
Positioner patrol range	9.5 mm (107.4 arcsec at the FoV center, 97.9 arcsec at the edge)			
Minimum fiber separation[b]	∼ 30 arcsec			
Fiber configuration time	∼ 60–120 sec			
Number of fibers	Science fibers		Fixed fiducial fibers	
	2394		96	
Fiber density	∼ 2000 $\deg^{-2}$ or ∼ 0.6 arcmin^{-2}			
Spectrograph				
Spectral arms	Blue	Red		NIR
		Low Res.	Mid Res.	
Spectral coverage	380 – 650 nm	630 – 970 nm	710 – 885 nm	940 – 1260 nm
Dispersion	∼ 0.7Å/pix	∼ 0.9Å/pix	∼ 0.4Å/pix	∼ 0.8Å/pix
Spectral resolution	∼ 2300	∼ 3000	∼ 5000	∼ 4300
Detector type/read-out mode	CCD	CCD		HgCdTe/SUTR
Spectrograph throughput[c]	∼ 53% (@500nm)	∼ 52% (@800nm)	∼ 47% (@800nm)	∼ 34% (@1100nm)

[a] This is a diameter of the sky projected onto the fiber core through the microlens with a magnification of 1.28.
[b] The minimum separation includes a physical limitation and a margin for collision avoidance.
[c] These values include detector QEs. The typical total throughput including primary mirror reflectivity, WFC, fiber systems, spectrograph optics, detector QE, etc. in blue, red, NIR, and medium resolution arms are ∼22% (@500nm), ∼26% (@800nm), ∼19% (@1100nm), and ∼23% (@800nm), respectively.

bundle of close-packed 128 fibers subtending 1.2 degrees on the sky. The telescopes are permanently mounted on the top ring of the Subaru Telescope and can feed one PFS spectrograph, allowing observations in parallel with any other Subaru instrument. One SuNSS telescope studies spatial and temporal variations in night sky emission, and the second uses a diffuser to assess sky subtraction performance. As both SuNSS telescopes have the same focal ratio as the Subaru Telescope, the sky signal received through each SuNSS fiber is the same as that through the PFI.

The PFS instrument will play an unique role amongst a growing set of massively-multiplexed spectrographs (MMS) in the next decade. We conclude this section with a brief overview of its capabilities in the context of similar instruments under construction or being commissioned elsewhere.

The only other MMS exploiting an 8-meter aperture telescope on a premier site is the Multi-Object Optical and Near-Infrared Spectrograph for the 8.2m VLT (MOONS). In comparison to PFS, MOONS has a more modest multiplex gain (500/1000 depending on whether beam switching is employed), accesses a smaller field of view (0.14 $\deg^2$), and with a wavelength range of 0.6–1.8 μm. Although its coverage extends further into the near-infrared, its survey speed and limited access to the full range of optical spectral features limits its competitiveness in most of the science applications discussed in this proposal.

The Dark Energy Spectroscopic Instrument (DESI) (DESI Collaboration et al. 2022) is an optical instrument on the refurbished Mayall 4.0m telescope which is undertaking a number of related galaxy and quasar surveys for studies of cosmology and large-scale structure (LSS). The largest component is a survey of 18M emission-line galaxies aimed at tracing the baryonic acoustic oscillation feature over the redshift range $0.6 < z < 1.6$. The multiplex gain of DESI (5000) and its field of view (8 $\deg^2$) are superior to those of PFS. However, the infrared capability of PFS will enable similar galaxy surveys to be conducted to redshifts beyond $z = 1.6$. While DESI is a dedicated facility on the Mayall telescope, PFS has the benefit of the significantly larger Subaru aperture and clearer and darker Maunakea skies. We discuss the complementary and competitive aspects of PFS and DESI further in Section 4.

The 4-meter Multi-Object Spectroscopic Telescope (4MOST) and the WHT Enhanced Area Velocity Explorer (WEAVE) are optical MMS facilities on the 4.1m VISTA and 4.2m William Herschel telescopes at Cerro Paranal and La Palma, respectively. 4MOST plans to undertake a wide range of extragalactic, Galactic and transient object surveys for the ESO community. It has a similar multiplex gain to PFS but the telescope has a larger field of view (4.2 $\deg^2$). Its main distinguishing feature is a high resolution ($R \simeq 20,000$) capability for stellar work. WEAVE is a more versatile facility with multi-fiber, multi-IFU and a single large IFU capability. The instrument exploits a new 3.1 $\deg^2$ field corrector. Its maximum multiplex gain is 1000. 70% of WHT time will be dedicated to a variety of surveys. Both 4MOST and WEAVE plan to undertake a wider range of surveys suitable for their 4m aperture telescopes and can be considered to be complementary to the plans proposed herein for PFS.

4. PFS COSMOLOGY: DARK ENERGY, TESTS OF GRAVITY AND NEUTRINO MASS

4.1. *Primary Goals*

Cosmological studies are crucially important in astrophysics given major unresolved questions relating to the nature of the world model and the growth of structures. PFS has been designed to offer outstanding opportunities in this area. The PFS cosmology program will map the three-dimensional positions of about 4 million emission-line galaxies (ELGs) over 1100 $\deg^2$ and a wide redshift range $0.6 < z < 2.4$, with a high number density over a comoving volume of 7.1 $(h^{-1}\mathrm{Gpc})^3$. With this dataset, we will study the nature of DE, test General Relativity (GR), and constrain cosmological parameters including the sum of neutrino masses with exquisite precision.

The initial conditions of the Universe at the time of recombination ($z \simeq 1090$) are accurately known from cosmic microwave background (CMB) data (Komatsu et al. 2014; Planck Collaboration et al. 2020). We can use these to evolve the Universe forward, making predictions for late-time observables, including the statistics of the galaxy distribution. The PFS cosmology survey program will test these predictions in a variety of ways:

• We will measure both the Hubble expansion rate $H(z)$ and the angular diameter distance $D_A(z)$ to 3% fractional accuracies in each of 7 redshift bins over $0.6 < z < 2.4$, using the baryon acoustic oscillation (BAO) method and the Alcock-Paczyński (AP) effect.

• We will use the distance measurements to determine the curvature parameter $\Omega_{\rm K}$ to 0.3% accuracy and the DE density $\Omega_{\rm DE}(z)$ to about 7% accuracy in each redshift bin, by combining with lower redshift BAO measurements.

• We will measure the redshift-space distortion (RSD) on linear scales to determine the growth rate of LSS $f\sigma_8(z)$[1] to 6% accuracy up to $z = 2.4$.

• We will also measure the broad-band shape and amplitude of the galaxy power spectrum and bispectrum over $0.6 < z < 2.4$ to obtain tighter constraints on cosmological parameters.

With these measurements, we can make significant progress in our understanding of fundamental physics. We will constrain the total neutrino mass to a precision of $\sigma(\sum m_\nu) = 0.02$ eV. If the neutrino mass hierarchy is inverted, this will enable a 5σ *detection* of $\sum m_\nu$, rather than an upper limit. We will also constrain models of time-evolving DE and modifications to GR on cosmological scales out to $z = 2.4$. The neutrino component described above represents "guaranteed science", whereas the DE campaign offers a "discovery potential" uniquely accessible to PFS. We describe these scientific goals in further detail below.

Neutrino physics: Massive neutrinos retard the growth of cosmic structure because their large velocity dispersion makes gravitational potentials shallower and the growth of density fluctuations is suppressed on scales below the so-called "neutrino free-streaming length" (Takada et al. 2006; Lesgourgues & Pastor 2006). This leads to a scale- and redshift-dependent suppression of the matter power spectrum amplitudes relative to that with massless neutrinos. The PFS cosmology program is designed with a long lever arm in both spatial scale and redshift, allowing improved measures of the power spectrum and thus the neutrino mass constraint. The top panel of Figure 3 shows the expected precision on the total neutrino mass using both the PFS power spectrum and bispectrum up to $k_{\rm max} = 0.2\,h$/Mpc, as well as CMB data from Planck 2018 (Planck Collaboration et al. 2020), galaxy clustering from BOSS/eBOSS (Alam et al. 2021), the expected weak lensing power spectrum from the full HSC SSP data, and the cross-power spectrum of PFS galaxies and HSC weak lensing. With PFS, these collected datasets will measure the sum of the neutrino masses to a precision of $\sigma(\sum m_\nu) = 0.02$ eV (68% CL).

Given existing neutrino oscillation data, the minimum total neutrino mass assuming the normal hierarchy is $\sum m_\nu^{\rm normal} \approx 0.06$ eV, while that for the inverted hierarchy is $\sum m_\nu^{\rm inverted} \approx 0.1$ eV (Esteban et al. 2019; Choudhury & Hannestad 2020). The bottom panel of Figure 3 shows the probability with which we will be able to reject the inverted mass hierarchy as a function of the actual total neutrino mass, as well as its de-

[1] Here $f \equiv {\rm d}\ln D(a)/{\rm d}\ln a$ is the growth rate of the linear density fluctuations, $D(a)$ is the growth factor, and σ_8 is the present-day rms mass density fluctuations within a sphere of radius $8h^{-1}$Mpc.

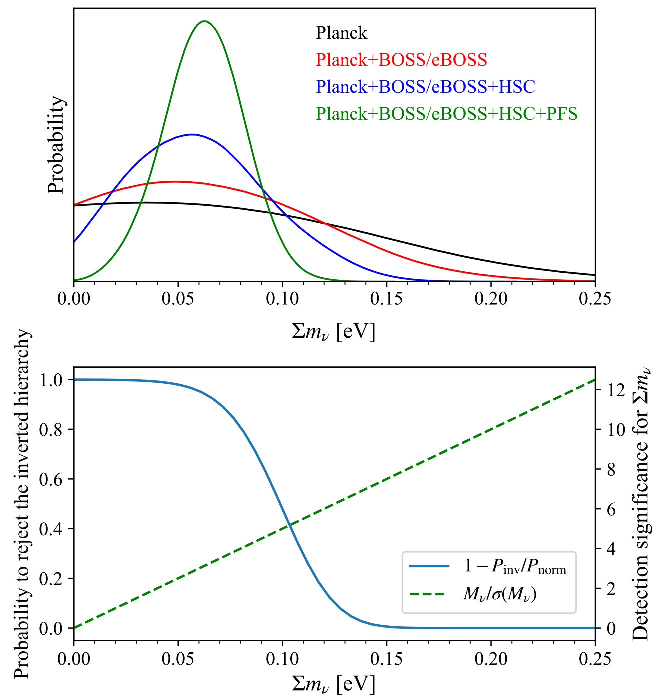

Figure 3. *Top panel*: Marginalised posterior distribution of the total neutrino mass from Planck 2018 data alone (black), Planck 2018+BOSS/eBOSS (red), Planck+BOSS/eBOSS+HSC forecast (blue), and Planck+BOSS/eBOSS+HSC+PFS forecast (green). $\sum m_\nu = 0.06$ eV is assumed for the input neutrino mass, corresponding to the lower limit for the normal mass hierarchy. The sum of neutrino masses will be constrained to 0.02 eV and 0.04 eV (68% and 95% confidence, respectively, from Planck+BOSS/eBOSS+HSC+PFS. The power spectrum and bispectrum are both used for the PFS forecast. *Bottom*: The probability with which the inverted mass hierarchy can be rejected (blue solid, left axis) and the detection significance number of sigma for the total neutrino mass (green dashed, right axis).

tection significance. The rejection probability is defined as $1-P_{\rm inv}/P_{\rm norm}$, where $P_{\rm inv}$ and $P_{\rm norm}$ are obtained by integrating the posterior of total neutrino mass at the mass range above $\sum m_\nu^{\rm inverted}$ and $\sum m_\nu^{\rm normal}$, respectively. If $\sum m_\nu = 0.06$ eV, the total mass can be detected with 3σ significance and the inverted mass hierarchy excluded at $> 2\sigma$ (1-$P_{\rm inv}/P_{\rm norm} = 0.95$). If $\sum m_\nu > 0.06$ eV, the normal and inverted hierarchies become indistinguishable but the mass detection significance increases. If $\sum m_\nu > 0.1$ eV, PFS will determine the total mass at $> 5\sigma$ significance. *In any of these cases, the results of the PFS cosmology survey will have profound implications for cosmology and particle physics.*

The expected constraints on $\sum m_\nu$ from PFS, DESI and Euclid are comparable because, for such small neutrino masses, they are limited by the uncertainty in the optical depth of the CMB, τ (Allison et al. 2015; Boyle & Komatsu 2018). Although DESI will have issued its first year (Y1) data release by the time the PFS survey commences (see below) and the Euclid survey will follow with its cosmology results, each of these surveys will likely reach $\sigma(\sum m_\nu) = 0.02$ eV on a similar timeline. Indeed, any claimed detection of the total neutrino mass will need confirmation from multiple experiments. In this sense, PFS, DESI and Euclid are complementary and thus each is indispensable.

DE vs. modified gravity: DE affects the angular diameter dis-

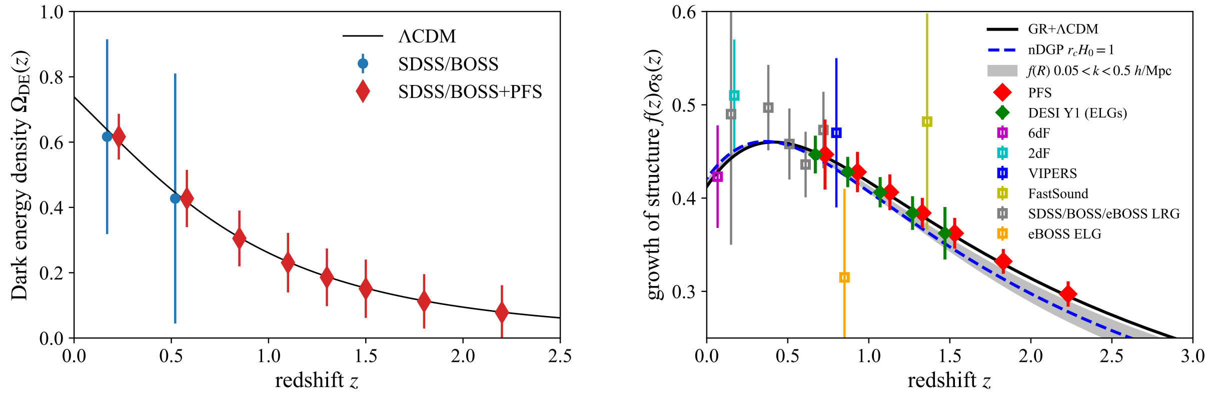

Figure 4. *Left panel*: Expected accuracy with which the PFS BAO-measured $D_A(z)$ and $H(z)$ will determine the DE density parameter $\Omega_{\rm DE}(z)$, as a function of redshift, assuming as input a flat ΛCDM model (solid curve). *Right*: Expected 1σ constraints on $f\sigma_8$ as a function of redshift, from PFS combined with Planck 2018, as well as existing constraints. The solid line assumes standard cosmology (GR+ΛCDM). The PFS forecast is based on both the power spectrum and bispectrum.

tance $D_A(z)$ and the expansion rate $H(z)$, which can be derived from the BAO and AP measurements (Eisenstein et al. 2005; Percival et al. 2010). While it is common to parameterize the properties of DE with the equation of state parameter $w_{\rm DE}$, it is more useful to evaluate a direct reconstruction of the DE density parameter $\Omega_{\rm DE}(z)$ as a function of redshift, as shown in the left panel of Figure 4. PFS will extend this measurement to $z = 2.4$, well beyond the DESI ELG sample. Because $D_A(z)$ depends on the integral of $1/H(z)$, it is sensitive to $\Omega_{\rm DE}(z)$ over a range of redshifts. Thus PFS will also improve the precision of $\Omega_{\rm DE}(z)$ at low redshifts. Measuring $\Omega_{\rm DE}(z)$ over a wide redshift range will constrain various DE models. For example, $w_{\rm DE}(z)$ is predicted to oscillate around -1 in models in which a continuous shift symmetry of the DE field is broken to a discrete symmetry (Frieman et al. 1995; Dodelson et al. 2000; D'Amico et al. 2016; Schmidt 2017). For a flat model with a constant equation of state, the geometrical constraints expected from PFS correspond to a precision $\sigma(w_{\rm DE}) \simeq 0.02$.

In April 2024, the DESI collaboration reported first-year cosmology results from their BAO measurements. These measurements alone are consistent with the standard flat ΛCDM cosmological model with $w_{\rm DE} = -0.99^{+0.15}_{-0.13}$, but hint at the possibility of a time-evolving dark energy when combined with CMB and/or Type Ia supernovae constraints (DESI Collaboration et al. 2024). The significance of this tantalising claim depends on the choice of the combined dataset. Nonetheless, given the importance of such a result, if correct, the PFS Cosmology program is uniquely placed to provide independent BAO measurements that would verify or otherwise falsify this claim. Of particular importance is the fact that PFS will chart the expansion history using a single tracer (ELGs) over an extended redshift range $0.6 < z < 2.4$, whereas DESI utilises a mixture of luminous red galaxies (LRGs) over $0.6 < z < 1.1$ and the Lyman-α forest over $1.8 < z < 4$. BAO measurements from different tracers will robustly test whether DE is a time-dependent phenomenon.

Another major question is whether the cosmic acceleration does not indicate the presence of DE but rather arises from a modification of GR on large scales. Such a modified theory of gravity would affect the growth rate of cosmic structures, which can be tested by measuring the RSD effect (Peacock et al. 2001). General Relativity predicts the growth index $\gamma = 0.55$ for $f \approx \Omega_{\rm m}(z)^{\gamma}$. However, a recent study (Nguyen et al. 2023) constrained the growth index $\gamma = 0.633^{+0.025}_{-0.024}$ using CMB data from Planck and LSS data from weak lensing, galaxy clustering, and RSD. All these data combined favor growth suppression stronger than the growth predicted from General Relativity. Currently this result is not based on any measurements above $z > 1.6$. The right panel of Figure 4 shows the expected constraints from PFS on the linear growth rate of structure, $f\sigma_8$, as a function of redshift. The PFS cosmology program will measure $f\sigma_8$ to $\sim$6% precision, which is better than existing constraints from any other surveys, and will be comparable to the constraint from the DESI Y1 analysis at $z \lesssim 1.2$. However, we can measure $f\sigma_8$ up to $z \simeq 2.4$, thereby extending observations into a hitherto uncharted redshift range and providing a powerful test of GR on growth of structure.

In summary, the PFS cosmology survey will chart the large-scale distribution of galaxies out to $z = 2.4$ with unprecedented fidelity over an enormous cosmic volume. This will enable studies of the *time evolution* of structure over 80% of cosmic history for the first time. In addition to measuring the *sum of the neutrino masses* to a precision of $\sigma(\sum m_\nu) = 0.02$ eV, PFS will provide a convincing test of the cosmological model beyond standard ΛCDM.

4.2. *Uniqueness of the PFS Cosmology Program*

In comparison to other spectroscopic surveys, such as DESI and Euclid, that will be underway at the same time, the PFS cosmology program is distinctive in three respects: (i) its extensive redshift coverage $0.6 < z < 2.4$, (ii) its high number density of galaxies ($\bar{n}_{\rm g} \gtrsim$ a few $\times 10^{-4}$ $(h^{-1}{\rm Mpc})^3$) at $z \gtrsim 1.5$, and (iii) its synergy with the deep HSC imaging survey. Below we describe the advantages of (i) and (ii), deferring discussion of (iii) until the following sub-section.

The PFS cosmology program samples its large redshift range $0.6 < z < 2.4$ with a *single* LSS tracer, ELGs, which is key for minimizing systematic effects. As cosmological measurements have become more precise, tensions have begun to appear between different probes. For example, the Hubble constant (H_0) measured using local distance-ladder techniques differs by 4.4σ from the Planck value (Bernal et al. 2016; Freedman 2017; Riess et al. 2019; Abdalla et al. 2022). PFS's measurements of $H(z)$ across a wide redshift range will address this tension by placing stringent constraints on the evolution of the late-time universe. A further tension arises from the con-

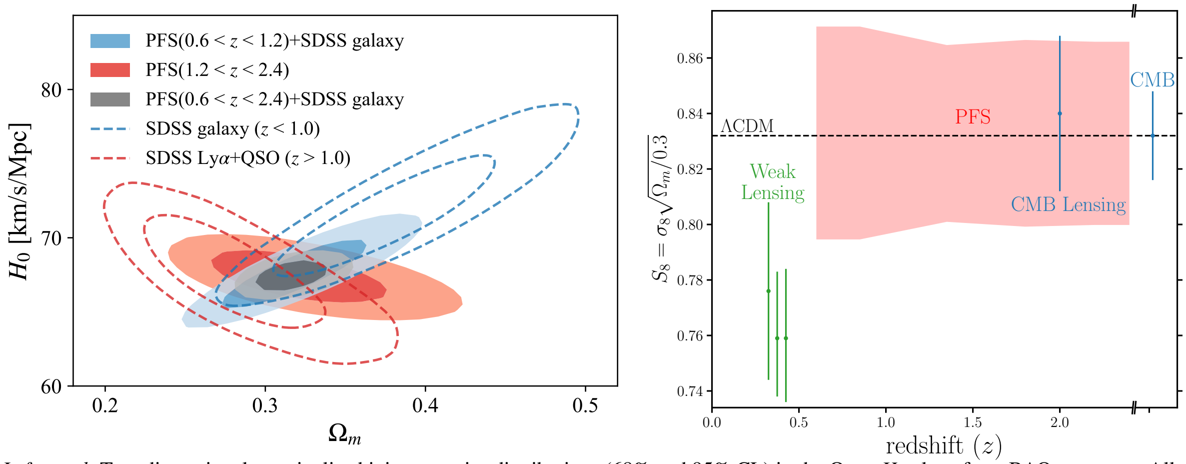

Figure 5. *Left panel*: Two-dimensional marginalised joint posterior distributions (68% and 95% CL) in the $\Omega_m - H_0$ plane from BAO measures. All constraints adopt a Big Bang nucleosynthesis (BBN) prior $\sigma(\Omega_b h^2) = 0.02$. Dashed lines show constraints from current data (Alam et al. 2021): BAO at $z < 1.0$ (red) and line-of-sight BAO (quasar and Lyman-α) above $z = 1.0$ (blue). Filled contours show expected constraints from PFS BAO measurements in low-z ($0.6 < z < 1.2$; blue) and high-z ($1.2 < z < 2.4$; red) bins. The gray contour shows the combined constraint. *Right panel*: Expected 1σ constraints on S_8 as a function of redshift from PFS (red shaded region) as well as the current constraints from different cosmological probes: weak lensing (green) and CMB (blue). The PFS forecasts include both the power spectrum and bispectrum.

straints on Ω_m and H_0 within a flat ΛCDM model between BAO measurements from the SDSS BOSS and eBOSS galaxies at $z < 1.0$, and those derived from the Lyman-α forest seen in quasars at $z > 1.0$ (the left panel of Figure 5). This tension between probes at low and high redshift could be an indication of new physics beyond the standard ΛCDM model. Alternatively, it may simply represent systematic effects arising from the use of different tracers. Note that the degeneracies in the $\Omega_m - H_0$ plane (the left panel of Figure 5) are different at low and high redshifts. *Thus, by undertaking measurements over a wide redshift range with a single tracer, PFS can break such degeneracies and directly address such tensions free from systematic biases.*

In addition to the use of a single tracer, PFS will make a robust measurement of $f\sigma_8$ using the RSD effect whereas, at high redshift, other surveys must use less precise methods. For example, for $z > 1.6$ DESI aims to utilize the Lyman-α forest where extracting $f\sigma_8$ is not straightforward because of radiative transfer uncertainties.

Along these lines, PFS will also robustly measure $S_8 = \sigma_8\sqrt{\Omega_m/0.3}$, the amplitude of the matter clustering, across $0.6 < z < 2.4$. Recent weak lensing analyses (Troxel et al. 2018; Asgari et al. 2021; Amon et al. 2022; Li et al. 2023; Dalal et al. 2023; Miyatake et al. 2023) and galaxy clustering analyses (Kobayashi et al. 2022; Ivanov et al. 2023) that probe LSS at $z \sim 0.5$ have found S_8 values that are in $\sim 2\sigma$ "tension" with the S_8 value expected from the best-fit ΛCDM cosmology from the Planck CMB (Planck Collaboration et al. 2020) and from the CMB lensing measurement (Madhavacheril et al. 2024). The right panel of Figure 5 shows the expected S_8 constraints from PFS as a function of redshift, as well as the existing constraints from weak lensing and CMB experiments. The PFS cosmology program will measure S_8 beyond the redshift ranges of DESI ELGs ($z > 1.5$ compared to $z_{\rm DESI} \lesssim 1.5$) and Euclid H$\alpha$ emitters ($z > 1.7$ to $z_{\rm Euclid} \lesssim 1.7$). Measurements from PFS will fully bridge the gap between S_8 constraints from the late and early Universe and produce stringent tests of the ΛCDM model.

A further advantage of the PFS cosmology program is the high number density of galaxies at $z \gtrsim 1.5$ which permits the study of under-dense regions (voids), providing complementary constraints and crucial internal consistency checks on the cosmological parameters. A high number density will be maintained throughout the redshift range, sufficient to robustly identify more than 10^3 voids per $(h^{-1}\mathrm{Gpc})^3$ volume at $0.6 < z < 2.4$ (whereas DESI expects a similar number only up to $z \sim 1.3$). The void size function constrains the DE equation of state and alternatives to GR (Pisani et al. 2015; Cai et al. 2015), while measuring the AP and RSD effects using voids will provide complementary constraints on Ω_m and the growth rate of structure (Sutter et al. 2014; Hamaus et al. 2017, 2020; Pisani et al. 2019). PFS RSD and AP void statistics will measure f/b (where b is the linear bias parameter) to a precision of 8%, and Ω_m to 3%. In addition, the void size function improves the neutrino mass constraints to $\sigma(\sum m_\nu) = 0.017$ eV when combined with galaxy clustering and weak lensing data (Massara et al. 2015; Kreisch et al. 2019; Zhang et al. 2020; Bayer et al. 2021; Kreisch et al. 2022).

PFS's high galaxy number density will also enable the extraction of cosmological information on small scales, thereby improving the measurement precision of both the rate of structure growth and the neutrino mass. Recent advances in emulators (Miyatake et al. 2022; Kobayashi et al. 2022) demonstrate that the power spectrum analyses can be extended to non-linear scales. For example, by extending the power spectrum analysis to $k_{\rm max} = 0.5\ h/\mathrm{Mpc}$ from a fiducial value of $k_{\rm max} = 0.2\ h/\mathrm{Mpc}$, the neutrino mass constraint from the power spectrum, bispectrum and galaxy-lensing cross-spectrum improves to $\sigma(\sum m_\nu) = 0.017$ eV, and growth rate constraints improve by $\sim 30\%$ in all redshift bins. The neutrino mass constraints will further improve if measures of the bispectrum on yet smaller scales are included (Hahn & Villaescusa-Navarro 2021; Chudaykin & Ivanov 2019). Information on higher-order statistics can also be extracted by reconstructing the density fields, the accuracy of which is ensured by the high number density of PFS galaxies.

4.3. *Synergy with the HSC and Other Datasets*

Although the PFS cosmology program exploits statistics of the galaxy distribution, by surveying the same cosmological volumes exploited by weak gravitational lensing campaigns, PFS will uniquely provide joint (and thereby improved) cos-

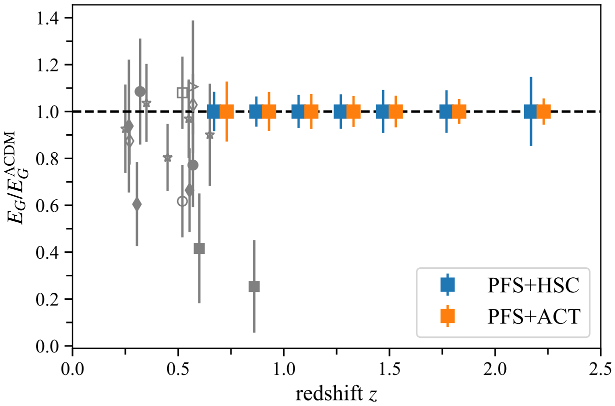

Figure 6. Expected 1-σ constraints on the $E_G(z)$ statistic (see text) relative to that of the GR prediction (the fiducial ΛCDM model), from PFS in combination with lensing data from HSC and ACT. As E_G does not depend on σ_8, the size of the error bar shows how well PFS *model-independently* constrains the growth rate, hence the theory of gravity. Gray points show existing EG measurements at low redshifts (Reyes et al. 2010; Blake et al. 2016; Pullen et al. 2016a; Alam et al. 2017; de la Torre et al. 2017; Amon et al. 2018; Singh et al. 2019; Jullo et al. 2019; Blake et al. 2020). To be conservative, only large-scale PFS measurements are used in these predictions: $\ell_{\max} = 350$ for $0.6 < z < 0.8$ and 780 for $2.0 < z < 2.4$. If smaller scale RSD and lensing measurements are included, the precision of E_G improves further.

mological constraints, test systematic effects via independent approaches, and calibrate key lensing uncertainties such as those arising from the use of photometric redshifts and intrinsic galaxy alignments. These synergies are particularly relevant for the now-completed HSC imaging survey.

The HSC imaging data, which reaches $i \simeq 26$ (5σ for a point source and $2''$ aperture) in 5 passbands (*grizy*) over 1100 deg^2, is the deepest available over large areas and will not be surpassed until the era of LSST. These multi-color data are used to select target galaxies for the PFS survey. The photometric accuracy, uniformity and depth of this parent catalog provides precise colors, ensuring the selection of an uniform ELG sample with a high redshift success rate. The expected throughput of the PFS instrument implies that ~ 75% of the targeted galaxies will have [O II] emission detected at S/N> 6 (see Section 7.2 for details), and thus have an accurate redshift. Simulations suggest that less than 0.22% of the redshifts will be incorrectly measured, thereby meeting the requirements necessary for accurately measuring the growth rate of structure (Pullen et al. 2016b). For comparison, Euclid's low-resolution grism will likely suffer from higher redshift misidentifications (Addison et al. 2019).

PFS clustering measurements will be biased low by the limited patrol areas of the robotic positioners, as well as the mild sparse sampling (70%) of our targets. Both effects would lead to a systematic incompleteness of close pairs of galaxies. However, our simulations indicate that weighting galaxies by the inverse of the probability that they are observed accurately mitigates this effect (Sunayama et al. 2020; Makiya & Sunayama 2022; Bianchi & Verde 2020). For this mitigation scheme to work, the photometric error in the parent sample must be less than a few percent and the HSC data readily satisfy this stringent condition.

PFS measurements of the large-scale galaxy distribution can be combined with complementary weak lensing information from the HSC survey. Such joint measurements significantly improve the cosmological and structure growth constraints and, crucially, reduce uncertainties arising from galaxy bias and nonlinear effects that are otherwise major sources of systematic error in all spectroscopic surveys (de la Torre et al. 2017). By cross-correlating the HSC weak lensing data with the 3-dimensional positions of PFS galaxies, we can measure the galaxy-matter correlation as a function of redshift, i.e., tomography of weak lensing data, yielding signal-to-noise ratios of 20 and 5 at the lowest ($z = 0.7$) and highest ($z = 2.2$) redshift bins, respectively (Makiya et al. 2021).

The synergy with HSC lensing data is particularly powerful when testing GR: galaxy positions tell us how galaxies move in response to gravitational potentials, whereas lensing tells us how light is bent by gravity in the same cosmic volumes. GR makes specific predictions for how these two gravitational effects are related. A joint analysis of redshift-space galaxy clustering and lensing thereby provides a model-independent test of gravity on cosmological scales much larger than the Solar System. Specifically, we can use the statistic $E_G(z) = \nabla^2(\psi - \phi)/f\delta_m$ (Zhang et al. 2007; Reyes et al. 2010), which is directly observable given that lensing and RSD measurements will both be available for the PFS galaxies. GR predicts a specific form for $E_G(z)$, and its measurement is free from uncertainties in the galaxy bias.

The PFS survey regions also overlap with those of ongoing and upcoming ground-based CMB experiments, including the Atacama Cosmology Telescope (ACT) and the Simons Observatory. These datasets will provide mass maps through weak lensing of the CMB from $z \approx 0.5$ to 3. Figure 6 shows the expected constraints on $E_G(z)$ from the combination of PFS, HSC, and ACT relative to that of the fiducial ΛCDM model. Any significant deviation from unity in this plot would represent a possible signature of modified gravity. Current measurements have large uncertainties and a limited redshift range, but hint at possible deviations. In combination with HSC and ACT, PFS will extend these measurements to high redshifts ($0.6 < z < 2.4$) with unprecedented precision (~ 5% in each of 7 redshift bins) and provide decisive evidence for, or against, modified gravity.

Cross-correlating PFS spectroscopic data with photometric HSC galaxies will calibrate the photometric redshifts of HSC galaxies and more accurately model the effect of intrinsic alignments, thereby improving cosmological analyses of the HSC weak lensing measurements (Hikage et al. 2019; Oguri & Takada 2011). Furthermore, cross-correlation of the PFS galaxies with HSC and CMB lensing data will permit calibration of various systematic effects inherent in each method and dataset (Schaan et al. 2017). These improvements will lead to more robust and accurate constraints on S_8, where, as mentioned above, the Planck and the cosmic shear measurements are currently in tension. In addition, the PFS ELG sample can be used to calibrate the selection function of ELGs in the shallower DESI and Euclid surveys.

Thus, the PFS cosmology program promises to advance our understanding of the nature of DE, to confirm robustly whether the H_0 and S_8 tensions are significant, and to obtain stringent constraints on cosmological parameters including the neutrino mass.

5. PFS GALACTIC ARCHAEOLOGY: THE STRUCTURE AND ASSEMBLY OF GALAXIES AND THEIR DARK MATTER HALOS

5.1. *Primary Goals of the PFS Galactic Archaeology Program*

Much of the DM physics is manifest on the scales probed by individual galaxies (e.g. Ostriker & Steinhardt 2003). This has the consequence that different types of DM make different predictions for observationally accessible properties of the stellar populations within Milky Way mass (and below) DM halos. However, the physics of baryonic matter also plays an unavoidable major role in determining these same properties of the light sector. We have devised a program with PFS that exploits its unprecedented field-of-view, depth and spectroscopic multiplexing capabilities to obtain the required large samples of precise stellar line-of-sight velocities and chemical abundances in galaxies of the Local Group, to disentangle the effects of the dark and light sectors and hence constrain the nature of DM.

We propose to target stars in selected galaxies within the Local Group and compare their derived properties with predictions from the concordance ΛCDM model of structure formation, plus alternative models with lower power on small scales. The three primary goals are:

• **Determination of the DM density profile in dwarf spheroidal galaxies (dSphs) with a range in stellar mass and star-formation history.** As is well-established, these extremely DM-dominated systems are the best-suited targets for testing the robust prediction of ΛCDM that the density profile, in the absence of baryons, should be cusped (Navarro et al. (1997), NFW). However, time-dependent gravitational perturbations will modify this profile; e.g., bursts of star formation could erase cusps in DM profiles (Mashchenko et al. 2008). Our science goal requires spectroscopic samples of thousands of stars, which PFS will provide. As discussed in more detail below, we will apply several different analysis techniques to our sample of dSphs, including an essentially model-independent determination of the inner slope of the density law introduced by Walker & Peñarrubia (2011), and two methods that break the mass-velocity dispersion anisotropy of classical spherical Jeans analyses.

• **Comparison of the stellar populations in M31 with those of the Milky Way, through the first chemodynamic spectroscopic survey of individual stars in our companion large disk galaxy.** PFS's unique ability to measure [α/Fe] for tens of thousands of stars in M31 will reveal both its major and minor merger histories. The major-merger history since $z \sim 2$ inferred for the Milky Way (MW) (e.g., Wyse 2001; Helmi et al. 2018) is unusually quiescent for typical ΛCDM galaxies (e.g., Evans et al. 2020). The proposed PFS measurements of kinematics and chemical abundances in M31 will further contextualize the MW's merger history and will provide the most detailed information for the assembly history of a galaxy outside the MW to date. Key observables are the patterns of [α/Fe] against [Fe/H] for the stars in the disk(s) and stellar halo. PFS will provide the chemical and kinematic data needed to test theories of disk formation that require a major merger (e.g., Renaud et al. 2021) or not (e.g., Vincenzo & Kobayashi 2020). Similarly, the chemical and kinematic structure and substructure in M31's halo will reflect the minor-merger history, as seen the "low-alpha" halo stars in the Milky Way that are likely debris from the Gaia-Enceladus Sausage (GES) merger (Helmi et al. 2018). The copious evidence of more recent accretion into M31, such as the Giant Southern Stream and the Northwest Stream, could potentially imprint a complex chemical pattern into the halo, that would contrast with that of the MW halo, which is dominated by a single, ancient merger (GES).

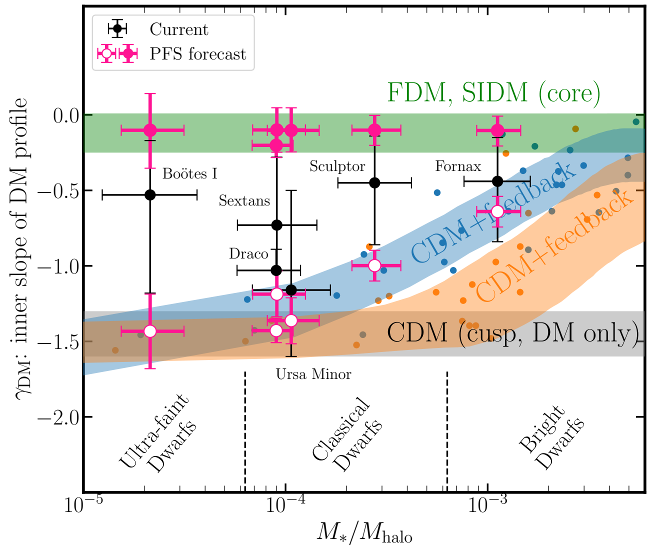

Figure 7. The inner DM density profile slope ($\gamma_{\rm DM}$) derived for our selected sample of dSphs vs. their stellar-to-halo mass ratio [Hayashi et al. (2020) with the addition of Boötes I]. ΛCDM predicts NFW cusps $\gamma_{\rm DM} \lesssim -1$ (*gray shading*). Hydrodynamical simulations (FIRE-2, *orange*: NIHAO, *blue*) predict that strong, episodic baryonic feedback can modify cusps into cores. However, most current estimates of $\gamma_{\rm DM}$ in MW dSphs (*black points*) are shallower than can be explained even with baryonic feedback, albeit with large error bars. PFS will give much more precise measurements, allowing us to distinguish between CDM+feedback models and non-standard models (*green shading*). The open and filled magenta points illustrate how PFS inferences of $\gamma_{\rm DM}$ would appear in these two respective cases. PFS will also infer the burstiness of SFHs – an indicator of the strength of feedback – from measurements of the [α/Fe] ratios of individual stars. Thus, we can test whether burstier SFHs result in a larger deviation from a cusp.

• **Investigation of the physical mechanisms that determine the ongoing build-up of the outer regions of the Milky Way.** We will use the unique combination of depth and areal coverage of PFS to target faint main-sequence turn-off stars in the outermost regions of the disk(s) and stellar halo, where dynamical times are longest and signatures of substructures persist. Main sequence turn-off stars provide an unbiased sampling of the underlying population and crucially allow for the determination of ages from isochrone fitting and spectrophotometric distances together with line-of-sight kinematics and chemical abundances from the spectra. We will be able to investigate relationships between stellar age, chemical abundance and kinematics, each as a function of Galactocentric distance. These will constrain dynamical heating mechanisms (such as those from fuzzy DM) and disk radial growth/rearrangement. The data will also allow an improved understanding of the edge of the stellar halo and of the thick-disk/halo interface in kinematic/chemical phase space, providing new constraints on their formation mechanism(s).

5.2. *Dwarf galaxies: Cusps, Cores, and Starbursts*

PFS will conduct an unprecedented survey of the density profiles of six dSphs, thereby determining whether the dSphs' density profiles support ΛCDM or alternative DM models. The unique strengths that allow PFS to probe DM on small scales are (i) 4000 – 15000 stars per dSph, (ii) wide-area coverage well suited for the angular extent of dSphs, (iii) velocity precision (significantly less than 3 km/s for most stars) much smaller than the velocity dispersion of a dSph (6 – 10 km/s), (iv) detailed abundance measurements, and

Table 2
Dwarf Galaxies Targeted by PFS

Galaxy	Distance [kpc]	$r_{\rm tidal}$ [′]	M_* [$10^6 M_\odot$]	⟨[Fe/H]⟩ [dex]	age	$N_{\rm literature}$	$N_{\rm pointings}$	$N_{\rm PFS}$
Boötes I	66	33	0.034	−2.6	ancient	118	4	2000
Draco	76	42	0.32	−1.9	ancient	269	4	7400
Ursa Minor	76	51	0.54	−2.1	ancient	190	8	3000
Sextans	86	83	0.70	−1.7	ancient	441	15	6500
Sculptor	86	77	3.9	−1.9	ancient	1497	8	6900
Fornax	147	71	24	−1.0	moderate	2603	8	14000
NGC 6822	460	···	83	−1.0	young	299	1	1000

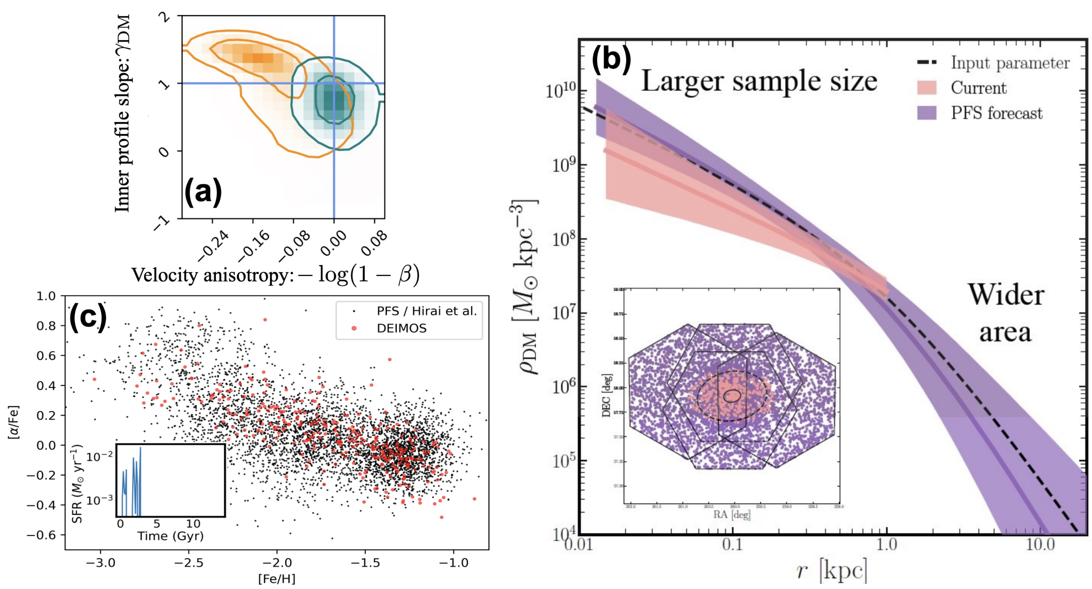

Figure 8. For each target dSph, PFS will provide large samples with very wide-area coverage, precise velocities, elemental abundance measurements and excellent membership probabilities, allowing us to undertake several new chemo-dynamical analyses. (a) MCMC posteriors on the inner profile slope (γ) and velocity anisotropy (β) from the Jeans analysis using only the 2nd velocity moment (orange) and both the 2nd and 4th velocity moments, i.e., including non-Gaussianity (cyan). The non-Gaussian model breaks the degeneracy between γ and β and better reproduces the input values ($\gamma = 1, \beta = 0$) (Wardana et al. 2024). (b) DM density profiles derived by non-spherical, 2nd-velocity-moment Jeans analysis. The underlying, Draco-like model is shown as a dashed line. The shaded curves correspond to the recovered density profiles using "Current" ($N = 500$) and "PFS forecast" ($N = 5,000$) samples, as shown in the inset. The ellipses correspond to the half-light and tidal radii. The extensive PFS sample size and spatial coverage will uniquely and accurately recover the density profile. (c) [α/Fe] vs. [Fe/H] for currently available spectroscopic data in a dSph (red, Kirby et al. 2011) and those anticipated from PFS (black) based on a cosmological simulation (Hirai et al. 2022) with bursts that could affect the DM profile. The clumping of the black points illustrate the effect of repeated starbursts (inset). Such clumping will only be revealed with PFS's large sample.

(v) synergy with Subaru/HSC broad-band and narrow-band pre-imaging.

The current, limited inferences for the inner density slopes, $\gamma_{\rm DM}$, in several dSphs are in tension even with the cored profiles predicted by hydrodynamical simulations that include baryonic feedback (Figure 7). Extremely low-luminosity galaxies, such as Boötes I, seem to have shallow slopes despite the comparative lack of baryons that could erode a cusp. More luminous gas-poor dSphs, such as Sculptor, seem to indicate slopes even shallower than the hydrodynamical simulations. This might hint that DM is not the usually adopted weakly interactive massive particle, but rather DM is fuzzy (FDM) or self-interacting (SIDM), which would induce a central core (Hui et al. 2017; Spergel & Steinhardt 2000; Chan et al. 2022). Alternatively, these results could merely reflect the limitations of the extant data or shortcomings in our understanding and modeling of baryonic feedback.

We will quantify the density distributions of our sample of dSphs using several independent techniques. First, Walker & Peñarrubia (2011, WP11) successfully used separate chemodynamical populations to quantify $\gamma_{\rm DM}$ in Fornax and Sculptor. The WP11 technique infers the inner density slope without any reliance or sensitivity to a choice of DM model, and it is not very sensitive to the velocity anisotropy. It requires that the galaxy has multiple stellar populations that have distinct sizes (half-light radii), kinematics (inner velocity dispersions), and chemistry (e.g., metallicity). The ability to identify multiple chemodynamical populations and to measure their velocity dispersion profiles requires thousands of stars with velocity precision better than 3 km s^{-1} and abundance precision better than 0.2 dex. PFS will meet these criteria in two crucial ways that improve on the existing implementations of the WP11 technique: (i) PFS will observe not just the inner regions of dSphs but also stars out to (and generally beyond) the nominal tidal edge, giving the best opportunity to identify and quantify multiple populations. (ii) PFS's ability to measure detailed elemental abundances will allow us to determine the existence of multiple chemical populations not just in metallicity but also in the space of [α/Fe] vs. [Fe/H].

The WP11 technique is powerful, but limited to estimations of enclosed mass at each sub-population's half-light radius. Therefore, we will also infer density profiles by directly modeling the velocity profile of each dSph via Jeans modeling. Typically, Jeans modeling assumes spherical symmetry, which is not a good assumption for ΛCDM halos. Therefore, we will employ non-spherical Jeans modeling (Hayashi et al. 2020), which breaks the degeneracy between mass and velocity anisotropy. Jeans modeling is also typically only applied to the velocity dispersion profile. By exploiting the large stellar samples, we will instead model the full line-of-sight velocity distributions (LOSVDs). The LOSVD technique requires samples of thousands of stars and secure membership determination. PFS uniquely satisfies both criteria for the five classical dSphs in Table 2 (the ultra-faint galaxy Boötes I contains too few stars). Coupled with the LOSVD analysis, the sample sizes will be sufficient to break the mass–velocity anisotropy degeneracy (see Figure 8 and Read et al. 2021). This technique can distinguish cusps from cores even if nature did not provide distinct chemodynamical stellar populations, and it gives the density profile over the full range of radii probed by the spectroscopic sample. Panels (a) and (b) of Figure 8 demonstrate the various techniques for measuring density profile applied to mock PFS data for the Draco dSph.

Several complications can confound an accurate measurement of the density profile. For example, binary stars alter the velocity distribution. Through detailed simulations of binary orbits and of PFS observation strategies, we determined that we can suppress the effect of binaries simply by observing each dSph twice, separated by about one year. More complex observational strategies have only marginal benefits. Rather than discarding binary stars, we will construct a Bayesian model to infer their center-of-mass velocities for input into the mass modeling. Another effect is dynamical disequilibrium, e.g. tides. By observing dSphs beyond their nominal tidal radii, derived from King-model fits to the light profiles, we can determine the degree to which the galaxy is out of equilibrium and adjust the models accordingly.

We have chosen a sample of six dSphs (Table 2) that span a range of $M_*/M_{\rm halo}$ and a range of SFHs. At the high-luminosity end, Fornax is expected to be heavily affected by baryonic feedback. At the low-luminosity end, feedback in Boötes I is expected to be too weak to erode an NFW cusp. The star formation histories (as derived from Subaru and HST imaging; Okamoto et al. 2017; Weisz et al. 2014) span from being nearly continuous (Fornax) to being truncated 10 Gyr ago (Sculptor, Boötes I). The sample includes three galaxies – Draco, Sextans, and Ursa Minor – with very similar $M_*/M_{\rm halo}$ but with disparate chemical and orbital properties, suggesting that the galaxies could have differing SFHs that could have influenced the density profiles differently.

We have imaged each of these galaxies in multiple bands with HSC, including the NB515 narrow-band filter which is sensitive to stellar surface gravity (Komiyama et al. 2018). This allows us to efficiently pre-select member red giant branch stars (RGB) and de-prioritize foreground MW dwarfs.

In addition to addressing the nature of DM, the PFS sample will also allow us to study dwarf galaxy physics with unprecedented detail. We will measure [Fe/H] for 40,000 stars and [α/Fe] and individual elemental abundances (C, Mg, Ni) for 18,000 stars across all seven dwarf galaxies. These measurements add information about the SFH and nucleosynthesis beyond what is available with [α/Fe]. Furthermore, we can estimate the relative ages of RGBs by combining their colors (measured by HSC) and elemental abundances (measured by PFS) and comparing with isochrones, giving further independent measures of the SFHs (Hirai et al. 2024).

Our sample also includes NGC 6822, a dIrr that is not a MW satellite and thus serves as a comparison for the dSphs, whose dynamical and chemical properties have been shaped by the MW. Previous spectroscopic samples for this galaxy have been limited to the center of the galaxy or to sparse single-slit spectroscopy, sufficient only to establish that this system has a complex dynamical structure (Valenzuela et al. 2007). PFS will measure the velocities and metallicities for 1,000 stars over the entire galaxy. This sample will hold the key to understanding the unusual red giant population that is misaligned with the H I disk, as well as the apparent dynamical instability in the outskirts of that disk (de Blok & Walter 2000).

5.3. *M31: Assembly of Luminous and Dark Halos*

PFS will conduct a massive large-scale spectroscopic survey of the internal kinematics and detailed chemistry of a spiral galaxy other than the MW. PFS will measure velocities (precise to 3 km s^{-1}) and open a new chemical dimension by providing [α/Fe] ratios (precise to 0.15 dex) of 30,000 member stars in M31. This sample size is orders of magnitude larger than existing samples of stars with comparable spectroscopic measurements (e.g., fewer than 1000 stars analyzed by Escala et al. 2022; Wojno et al. 2023). Figure 9 shows the wide coverage of the halo and outer disk to be targeted.

Dey et al. (2023) recently demonstrated how massively multiplexed spectroscopy from DESI can illuminate the accretion history of M31 by revealing the kinematic signature of a merger event. PFS will further revolutionize the study of M31 not only by measuring [α/Fe] but also by reaching up to one magnitude deeper than DESI (for bluer RGB stars; we will reach 0.5 mag deeper for the red RGB stars that were the primary targets of Dey et al. 2023).

A galaxy's accretion history imprints itself on the [α/Fe] abundance pattern of its stars. For example, the quiet accretion history of the MW means that the GES stands out clearly in the [α/Fe] vs. [Fe/H] diagram of the stellar halo. The result is a bimodal distribution of [α/Fe] at fixed [Fe/H]. If M31 had a more active recent accretion history, it would have a less ordered halo [α/Fe] distribution, with multiple overlapping tracks whose relative contributions would vary with location and kinematic cuts, reflecting the individual stellar populations and orbits of the accreted systems. The existing [α/Fe] measurements (e.g., Gilbert et al. 2019) are insufficient to indicate whether M31's halo has a component with GES-like chemistry. PFS will definitively reveal chemical subpopulations (see right panel of Figure 9).

The accretion history affects the chemical composition of the disk, in addition to the halo. More frequent or more massive mergers cause more vertical heating (Hayashi & Chiba 2006), which can displace older, α-enhanced stars. The existing resolved spectroscopy in M31 gives conflicting results about whether the disk possesses a bimodality similar to the MW. Although planetary nebulae (Arnaboldi et al. 2022, interpreted in Kobayashi et al. 2023) show evidence for a bimodal distribution of [O/Ar] at fixed [Ar/H] – a proxy for [α/Fe] vs [Fe/H] – JWST/NIRSpec spectroscopy of red giants (Nidever et al. 2024) does not confirm this bimodality. The measurement of [α/Fe] over the face of M31 sets PFS apart from these studies and from other massively multiplexed spectrographic surveys targeting M31, such as that with DESI (Dey et al. 2023).

PFS stellar velocities will allow us to distinguish between high angular momentum (disk) and dispersion-supported (halo) components of M31, allowing us to untangle the disturbed disk from disrupted satellites. In addition to quantifying the

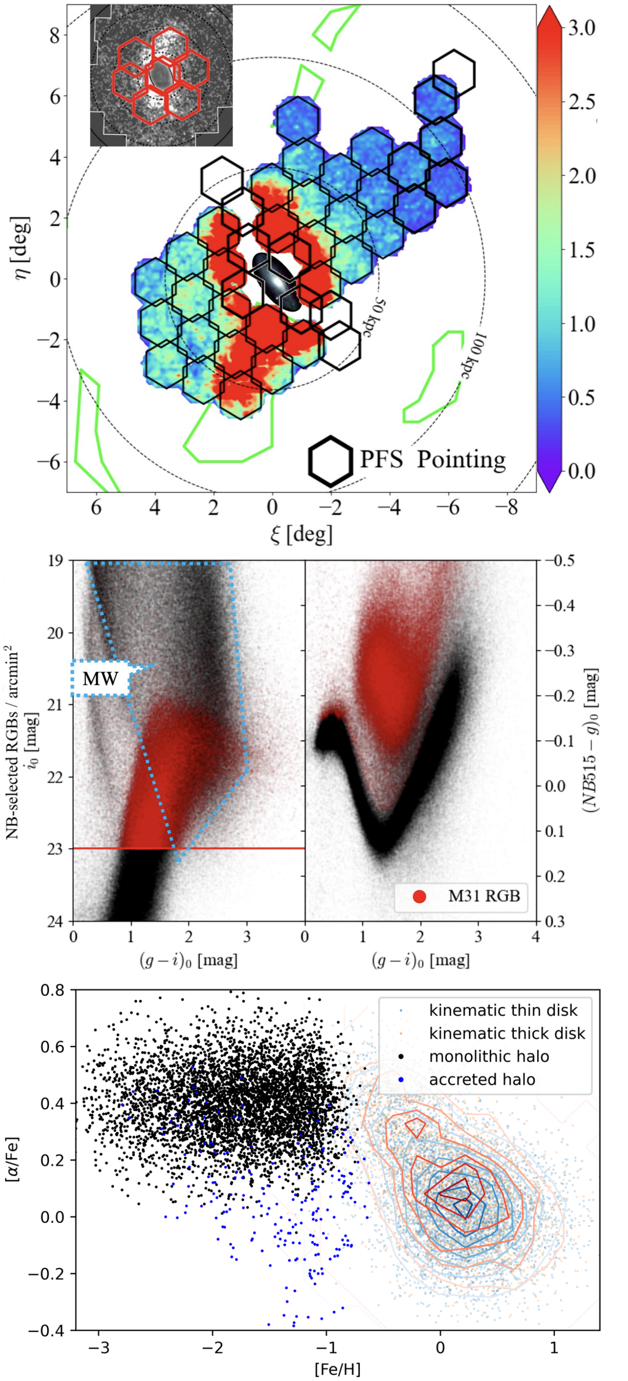

Figure 9. *Top panel*: Proposed PFS pointings (*red hexagons*) in M31 and M33 (inset). The coloring gives the stellar density of candidate member stars selected with HSC broadband and narrow-band imaging. *Middle*: HSC color–magnitude and color–color diagrams for stars in M31. Candidate red giant members (*red points*) are identified through color–color selection (note that the redder, fainter RGB and dwarf stars will be classified using machine-learning techniques). *Bottom*: Abundances for a mock PFS observation of M31. PFS can distinguish between an accreted and a monolithic halo, even if the accreted component is only 5% of the total halo. PFS could also detect a MW-like chemodynamic bimodality in M31's disk when the stars are differentiated by line-of-sight velocity.

accretion history with [α/Fe], we will also model the DM profile out to 60 kpc by measuring the velocity dispersion of the halo as a function of projected radius. The sample will inevitably contain a great deal of kinematic substructure in the form of stellar streams. Published kinematics for stars in the Giant Southern Stream (GSS) have only been derived from pencil-beam spectroscopy at strategic locations (Gilbert et al. 2019), while PFS will cover the entire structure. The PFS footprint also includes the Northwest Stream, which has very limited spectroscopy at present. The measurements of velocities and elemental abundances will allow us to infer the orbits, stellar masses, and SFHs of the progenitor galaxies – or galaxy (see, for example, Hammer et al. 2018).

As for the MW dSphs (Section 5.2), we have observed almost all M31 fields with HSC broadband and narrowband filters to identify foreground dwarf stars (Ogami et al. 2024), whose color–magnitude and color–color selection are indicated in the middle panel of Figure 9 (note that the redder, fainter RGB and dwarf stars will be classified using machine-learning techniques; Ding, Filion & Wyse, in prep.).

M31 is distinct from the MW in possessing a *bona fide* spiral galaxy satellite, M33. We include pointings in M33 to examine the structure of a galaxy intermediate in mass between the MW/M31 and the dwarf galaxies of Section 5.2. The outskirts of M33 are not well-observed, either photometrically (McMonigal et al. 2016) or spectroscopically (Gilbert et al. 2022). This is despite ΛCDM's prediction that such a low mass galaxy should have a stellar halo (Deason et al. 2022). We propose to observe a few thousand candidate member stars to test this definitively. Using kinematics we will quantify the total mass of M33 and uncover its accretion history through elemental abundances.

5.4. *To the Outer Limits of the Evolving Milky Way*

PFS will provide precise chemodynamic data for unbiased tracers (main-sequence stars) in each of the stellar components of the MW galaxy to unprecedented distances. We propose a deep, multi-pencil-beam study of the disks and halo targeting primarily distant main sequence FGK dwarf stars, to obtain line-of-sight velocities, elemental abundances, spectrophotometric distances and isochrone-based age estimates, out to distances of $\sim$ 30 kpc.

The main science goal is to determine the dominant mechanisms by which the MW evolved through the analysis of the chemodynamics and age distributions of unbiased tracers of the stellar populations in the outer parts (main sequence stars). As discussed above, the growth of our Galaxy since redshift > 2 was most likely dominated by smooth accretion from the circumgalactic medium and minor mergers – an ongoing process given the assimilation of the Sagittarius dwarf and interactions with the Magellanic Clouds. Structures in chemo-dynamical (and coordinate) phase space persist in the outer Galaxy, reflecting the longer dynamical times there, and thus the outer Galaxy contains clues about the emergence of the present-day MW.

For example, the spatial distribution of bright tracers, such as Blue Horizontal Branch stars, have indicated that there is a "pile-up" at $\sim$ 30 kpc (Deason et al. 2018), which could be due to an apocenter turnaround of the now-disrupted GES progenitor galaxy (see also Deason et al. 2020). PFS will provide spectra for main-sequence stars at Galactocentric radii out to, and including, this putative "pile-up", allowing us to characterise it more fully. Further, the main-sequence stars that are our primary targets reach out to the distance regime where

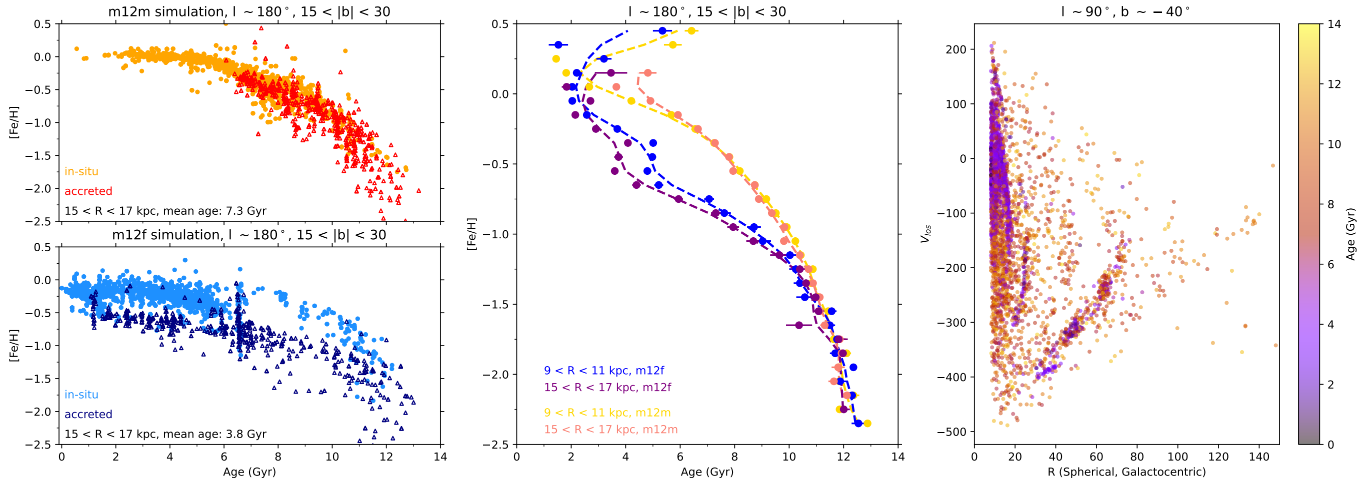

Figure 10. PFS allows unprecedented analyses of the furthest regions of the Milky Way using main-sequence stars as tracers of the dominant population. *Left and middle panels*: The large samples of stars with estimated distances, ages and iron abundances in our proposed low-latitude fields will reveal the build-up of the outer disk. The two leftmost panels show scatter plots of predicted age/iron abundance from two FIRE-2 simulations indicating how the merger history is discernable. The middle panel shows predictions of the mean age at given iron abundance at two Galactocentric radii. The turnaround at the highest iron abundance is an indication of radial migration redistributing older more metal-rich stars outwards. *Right*: Predictions for higher-latitude halo stars based on FIRE-2 simulations. The scatter plot shows the distinct 'chevron' pattern in line-of-sight velocity as a function of (spherical) Galactocentric distance resulting from radially biased merger(s). The addition of age via main-sequence tracers will allow the merger to be delineated more clearly, as illustrated by the color-coding in the figure.

the dynamical perturbation from the Large Magellanic Cloud should be evident in their kinematics (e.g., Erkal et al. 2021). Much remains uncertain about the LMC-MW interaction, as discussed in the recent review by Vasiliev (2023).

The debris from a disrupted satellite on a radial orbit will create a "chevron" pattern in a plot of V_r, the component of velocity towards/away from the Galactic center, against Galactocentric distance, r, as seen in the FIRE simulation (Figure 10, right panel). This reflects wrapping of the debris' phase-space density and has recently been discovered for the local Gaia sample (Belokurov et al. 2023). Our data will enable us to quantify the phase-space structure of this debris out to the probable furthest apocenter passage of the parent dwarf galaxy and thus reveal the early evolution of the merger.

The disk-halo interface is of particular interest in terms of separating the disturbed disk from substructure in the halo (see e.g., Li et al. 2017) and the strategy we have adopted includes continuous coverage of the latitude range 15° to 40° in key directions towards both that of Galactic rotation ($\ell = 90°$) and the anti-center ($\ell = 180°$), where line-of-sight velocities are dominated by contributions from V_ϕ and V_R respectively (see also Part II of this proposal).

Similarly, we will use our derived ages, distances, chemical abundances and line-of-sight velocities (combined with proper motions where available) in lower-latitude fields to trace the growth of the disk. The data will allow analyses of trends such as the age-metallicity relation as a function of Galactocentric distance (see left and middle panels of Figure 10), and as functions of α-abundance and kinematics, to distinguish thick and thin disks, for which different modes of formation and evolution have been proposed. The existence (or not) of distinct α-sequences in the outermost disk can thus be quantified, significantly extending the influential analysis of Hayden et al. (2015). We will compare the data with models for the thin disk that combine radial migration – bringing older, more metal-rich stars from the inner disk – with recent star-formation from gas mixed with primordial inflow – adding younger, more metal-poor stars. Our use of main-sequence stars means that we can add the dimensions of age and chemical abundances to the analysis of the kinematic phase-space structure of the outer disk, significantly enhancing the information to be extracted (see Laporte et al. 2022 for how ages discriminate between competing interpretations of the kinematic phase-space structure in the outer disk). PFS will also allow a first estimation of age-velocity dispersion relations for main-sequence stars in the outer disk(s), an important test of fuzzy DM models (Chiang et al. 2023). As Chiang et al. (2023) discuss, it is particularly important to obtain data at large Galactocentric distances, $R > 12$ kpc, where the disk is expected to no longer be self-gravitating and lacks internal perturbations such as giant molecular clouds, but beyond the reach of current analyses (cf. Mackereth et al. 2019).

Furthermore, the chemodynamic data and age estimates will allow us to evaluate and compare models in which (i) the early MW formed as a thick, kinematically hot, stellar disk (e.g. Bird et al. 2021) or (ii) one in which stars generally form in thin kinematically cold disks (e.g. Tamfal et al. 2022).

Fields at intermediate latitude probe the thick disk-halo interface and together with the high-latitude fields will provide the data to test the suggestion, based primarily on the local Gaia sample, that the *in situ* halo is largely the kinematic extreme of the thick disk – the "Splash" of Belokurov et al. (2020). This component of the halo should be more centrally concentrated than the accreted debris of GES, as it should reflect the radial profile of the pre-existing stellar disk that was heated kinematically by the merger event. Our data will test this through analysis of the chemodynamic phase-space structure of the *in situ* stellar halo, using main sequence stars rather than the rarer, brighter tracers of previous analyses (see bottom panel of Figure 10).[2]

The high latitude fields along the lines of sight of distant (> 10 kpc) streams will be used to constrain the Galactic acceleration field in the outer halo (Ibata et al. 2021). Those streams provide a new constraint on the dynamical structure of the MW, including its reflex motion in response to the approach

[2] For example, the H3 survey, which similarly explores the structure of the distant stellar halo, uses giant stars as tracers (e.g., Han et al. 2022, and in particular their selection function in the Appendix.)

of the LMC (Erkal et al. 2019).

Our multi-faceted approach to the characterization of the properties of stars in Local Group galaxies should reveal the interplay between stars and DM on critical scales for tests of the nature of DM.

6. PFS GALAXY EVOLUTION STUDIES

The evolution of galaxies is inextricably linked to the cosmic web (Somerville & Davé 2015). After inflation, the primordial density fluctuations grow via gravitational instability, amplifying the DM density contrast, and eventually forming a cosmic web of sheets, filaments, and nodes containing virialized DM halos. Baryons flow with the DM on large scales, and some are incorporated into the halos. Unlike DM, baryons can lose energy by radiation, and sink deeper into the potential well. In the simplest picture, this inflow is halted by centrifugal forces and the baryons form a disk (Mo et al. 1998; Burkert et al. 2016). Galaxies continue to grow over billions of years, primarily though continuing accretion of gas from the web, and secondarily through mergers with other DM halos and their baryonic contents (e.g., Vogelsberger et al. 2014). This accretion fuels the formation of stars and supermassive black holes, and the feedback from these play critical roles in the regulation of the galaxy properties over cosmic time, and in the ionization and enrichment of the intergalactic medium. (e.g., Croton et al. 2006).

While this conceptual picture provides a good foundation, there are many important questions that are not yet answered:

- How and when was the intergalactic medium re-ionized?
- How does the interplay between dark and baryonic matter shape the evolution of galaxies?
- How do gas and metals flow into and out of galaxies?
- How do tight relations between fundamental galaxy properties arise and evolve?

These questions about galaxy formation cannot be answered without a large spectroscopic survey at $z \gtrsim 0.7$. Spectra provide a rich suite of diagnostics of the fundamental properties of galaxies and their environments. The sample must be sufficiently large to map out the distributions of, and causal connections between, these properties, and to chart their evolution in redshift. In order to optimally measure the galaxy properties, the spectral resolution must be matched to the internal velocity dispersions of galaxies and the signal-to-noise ratio must be sufficient to measure the key spectral diagnostics. To connect the properties of galaxies to the large-scale cosmic web, the spectroscopic survey must probe a large volume, and do so with sufficient spatial sampling.

In this section we describe a program that is motivated by these considerations through an optimal use of the capabilities of PFS (see also Greene et al. 2022).

6.1. *Setting the Stage*

6.1.1. *Survey Design*

With $\sim$ 2000 science fibers deployable over 1.3 deg^2 FoV, and wavelength coverage out to 1.26 μm, the PFS spectrograph is uniquely positioned in the coming decade to probe the evolution of typical Milky Way-like galaxies from the epoch of reionization at $z \sim 7$ to the present, in the context of the cosmic web. The PFS Galaxy Evolution (GE) survey will accomplish this with complementary sub-samples, each designed to fully leverage the instrumental capabilities and capture the physical properties of galaxies at critical moments in cosmic history (see Figure 11 and Table 3).

Table 3
Galaxy samples and depths

Type	Redshift range	Selection	Exp. Time (hrs)	Expected # of spectra ($\times 10^3$)
Continuum	0.7 – 2	$y, J < 22.8$	2, 12	261, 14
IGM	2.1 – 3.5	$y < 24.3, g < 24.7$	6, 12	30.3, 14
LBG	3.5 – 7	$y < 24.5$	6	22
LAE	2.2, 5,7, 6.6	$L_{Ly\alpha} > 3\times10^{42}$ erg s^{-1}	3, 6, 12	7.4, 4.5, 2.8
AGN	0.5 – 6.0	various (see text)	1 – 5	4.2

We will study the peak epoch of star formation using "*continuum-selected galaxies*" with J_{AB}<22.8, which will capture ~90% of the $M_* \gtrsim 3\times10^{10} M_\odot$ population at redshifts of $z \lesssim 2$. This main sample of 360,000 galaxies will have a ~70% average completeness and thus include multiple galaxies in group-scale halos down to $M_{\rm group} \sim 10^{13.5} M_\odot$. Exposure times of 2-hour integrations will provide a high spectroscopic redshift completeness. We will integrate for 8–12 hours on an additional 10,000 galaxies to measure stellar ages, chemical abundance ratios, stellar velocity dispersions, outflow properties, and faint emission lines such as [O III] λ4363.

The overarching connection of galaxies to LSS will be extended out to z~6. In particular, the distribution of neutral hydrogen in the cosmic web at z=2.1−2.5 will be mapped at a co-moving scale of ~4 Mpc through an "*IGM tomographic experiment*" based on the detection of Lyman-α absorption seen in the spectra of background galaxies at $2.5 \lesssim z \lesssim 3.5$. At the furthest distances, we will use a sample of ~15k "*Lyman-α emitters*" (LAEs) at 6<z<7 selected from the Subaru/HSC narrow-band imaging to connect early galaxies to the cosmic web and probe the epoch of reionization.

Together, these samples will allow us to jointly address two main themes from $z \sim 0.7$ to 7. On the largest scale, we will map the cosmic web through the distribution of gas and galaxies (Section 6.3). On smaller scales, we will measure the evolution of the properties of the stars and gas in galaxies to elucidate the underlying physical processes driving their formation and growth (Sections 6.4 and 6.5). The detailed design of our survey will be described in Part II of this SSP proposal, guided by the above considerations.

6.1.2. *The PFS GE Program in Context*

This survey represents a dramatic improvement in sample size, spectral resolution, and target density over previous spectroscopic surveys of the critical epoch of galaxy formation (z>1). Previous studies have been limited to lower redshifts, e.g., zCOSMOS (Lilly et al. 2007) and VVDS (Le Fèvre et al. 2005), or at higher z to much smaller, biased samples, e.g., KBSS (Steidel et al. 2014), MOSDEF (Kriek et al. 2015), and FMOS-COSMOS (Silverman et al. 2015), or low spectral resolution, e.g., 3D-HST (Momcheva et al. 2016), as illustrated in Figure 12.

Our survey is also highly complementary to the other upcoming massively multiplexed spectroscopic survey studying the properties of $z = 1 - 6$ galaxies, MOONRISE (Maiolino et al. 2020). VLT/MOONS will cover the rest-frame optical lines to $z \approx 2$, allowing for better characterization of ISM physics at cosmic noon, but (unlike PFS) does not cover the

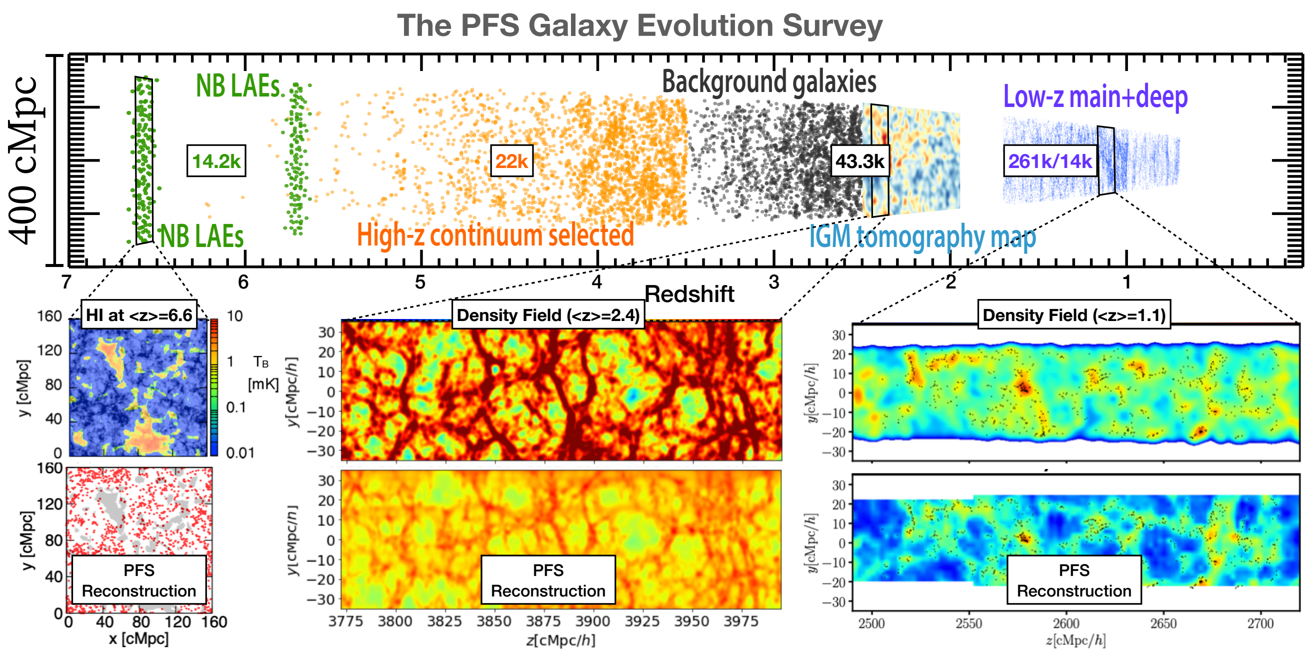

Figure 11. Number of spectra in each subset of the PFS GE survey (top) and a representative light cone to demonstrate the key redshift regimes it will probe (middle). Pop-out panels depict the recovery of cosmic structures from the PFS SSP (top panels: truth, bottom panels: recovered) at $\langle z \rangle = 1.1, 2.4$ and 6.6. The top left panel shows reionization bubbles in the HI 21cm brightness temperature distribution from Kubota et al. (2020), while the bottom panel shows the LAE distribution observed by PFS spectroscopy, which is anti-correlated with the ionized bubbles in this particular model. The top middle and right panels show the simulated density fields from the Horizon AGN simulation at $\langle z \rangle = 2.4$ and $\langle z \rangle = 1.1$, while bottom middle and right show the reconstructed density from the PFS galaxy redshift distribution and IGM absorption data using the TARDIS (Horowitz et al. 2019) and ARGO (Ata et al. 2015) algorithms.

Table 4
Large-Scale Structure probed by the GE Survey

Component of the Web	Expected Number
$M_{\rm halo} \gtrsim 10^{13} M_\odot$	2200
$M_{\rm halo} \gtrsim 10^{13.5} M_\odot$	450
$M_{\rm halo} \gtrsim 10^{14} M_\odot$	35
Voids ($z < 2$, $r > 7$ cMpc)	132,000
Voids ($z < 2$, $r > 20$ cMpc)	3,000
Voids ($z > 2$, $r > 7$ cMpc)	1000
Protoclusters	100

rest-frame far-UV at this epoch. PFS will have roughly twice the number of fiber-hours (~1.3 million hours versus 500,000 hours for the MOONRISE XSwitch strategy) and blue spectral coverage. Together these allow us to perform an IGM tomography survey (characterizing the cosmic web and the IGM at cosmic noon), go deep on continuum-selected galaxies at $z \approx 1.5$, map the Circum-Galactic Medium (CGM) at $z \approx 1$ to 2, and probe Lyman-α emission in galaxies at $z \gtrsim 2$. Relative to MOONRISE, we also benefit from the superb HSC multi-band imaging data for our galaxies. Finally, our high spectral resolution and broad wavelength coverage will also be complementary to the Euclid and Roman Space Telescope grism surveys.

6.2. *How and When was the Universe Re-ionized?*

The re-ionization of the universe represents a crucial phase transition in its baryonic content, and traces the formation of the first stars, galaxies, and black holes at very early times. This implies a close connection between these galaxies and the cosmic web from which they formed.

At $5.5 \lesssim z \lesssim 7$, spanning the epoch of reionization, we will map the galaxy-web connection by measuring the spatial cross-power spectrum between the ionizing galaxies, detected by PFS as LAEs, and the HI gas in the cosmic web detected in redshifted 21 cm emission by the SKA1 array. Theoretical models predict that cross-power spectrum transits from positive on small scales to negative on larger scales. Models predict that on small scales (single ionized bubbles), one-halo clustering introduces a positive correlation. Beyond the bubble radius, an anti-correlation will result if reionization proceeds from regions of high to low density. The amplitude of the signal, the spatial scale at which the correlations become negative, and the overall shape of the cross-power spectrum, all constrain the reionization history of the Universe. The detection of this signal will be a definitive confirmation of the 21-cm signal from the EOR and an independent measurement of the ionization history of the universe.

6.3. *How does the interplay between dark and baryonic matter shape the evolution of galaxies?*

In this section we describe how the PFS data will reveal the relationships between dark and baryonic matter over a wide range of scales and redshifts. We begin with the largest scales (the cosmic web) and then move to smaller scales (DM halos).

The growth of LSS drives the evolution of DM halos and the flow of gas between and into galaxies, and therefore is the fundamental process behind the formation and evolution of galaxies themselves. On the largest scales, we have strong theoretical reasons to believe that galaxies evolving in voids will have different star formation histories and angular momentum distributions from those in filaments or nodes. We know that the orientation of filaments does impact the spins of galaxies (e.g., Kereš et al. 2005; Pichon et al. 2011), and possibly their star formation histories (e.g., Kraljic et al. 2018),

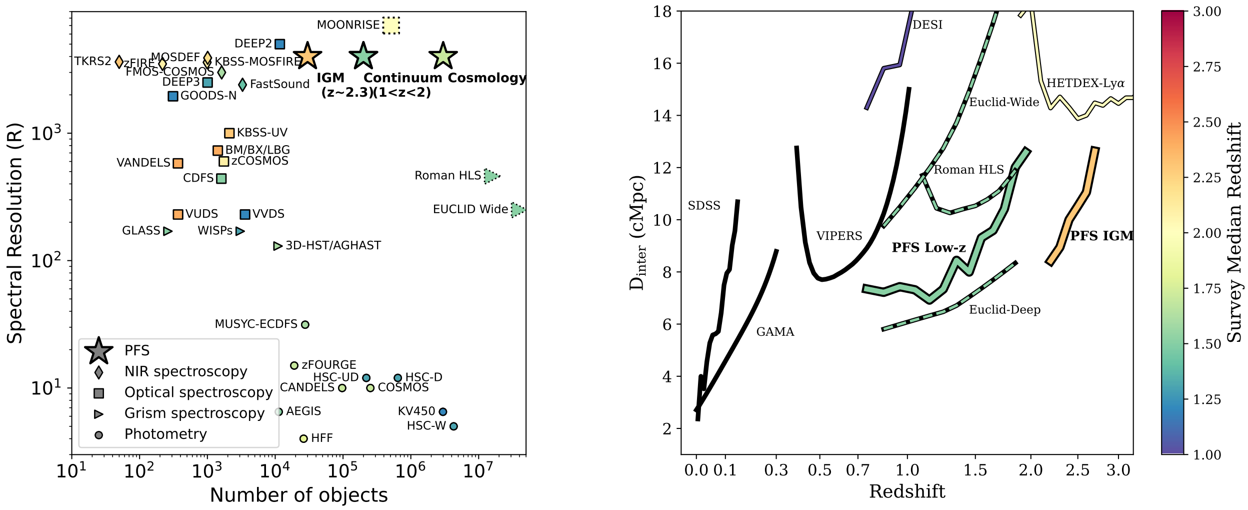

Figure 12. *Left panel*: The combined spectral resolution and statistical samples produced by the PFS GE survey components would lie in unprecedented parameter space at $z \gtrsim 1$ (compilation adapted from Förster Schreiber & Wuyts 2020). *Right*: $D_{\rm inter}$ is the average distance between galaxies, highlighting that the dense sampling and large volume probed by the PFS sample will extend maps of the cosmic web beyond the local Universe.

while mergers which take place as galaxies move along filaments will change the angular momentum direction and may lead to quenching (e.g., Dubois et al. 2014). Large galaxy redshift surveys like VIPERS and zCOSMOS at $z \approx 0.7$ make preliminary detections of these effects (Malavasi et al. 2017; Laigle et al. 2018).

Prior to PFS it was not possible for a single survey to test this at earlier times with simultaneously (i) wide enough area to probe the rarest overdensities and overcome cosmic variance and (ii) dense enough sampling to trace the LSS on $\sim$1$-$3 Mpc scales. Thanks to our unprecedented multiplexing and wavelength coverage, we will perform the redshift survey needed to make a high-fidelity map of the LSS in the distant Universe and situate the galaxy properties within that context (Table 4).

We will be able to connect galaxies to the cosmic web at two key epochs. We have already described in section 6.2 above how we will map the connection between galaxies and the cosmic web during the EOR, using the cross-correlation between PFS LAEs and HI gas.

At cosmic noon, the IGM tomography sample will not only trace the cosmic web, but also provide new insight into the state of the gas in and around galaxies. A critical component of our program is the measurement of foreground galaxy redshifts, i.e., 25k continuum-selected galaxies, 9.2k LAEs, and 1.3k active galactic nuclei (AGNs), that lie within the HI web. With this sample, we will use morphological features identified through HSC (and later Roman) imaging to constrain possible intrinsic alignments with respect to the cosmic web traced by the HI tomography. We will also measure the 3D cross-correlation between the galaxies and HI absorption to constrain the underlying bias (and hence halo mass) of the galaxies as a function of stellar mass, star-formation rate, metallicity, and other properties. Cross-correlations can also be extended to metals near galaxies, allowing the study to extend down to CGM scales in conjunction with detailed hydrodynamical simulations (Fujita et al, in prep.).

On intermediate spatial scales, the DM distribution leads to variations in galaxy overdensity, ranging from clusters to groups to isolated galaxies. With PFS we can robustly measure the evolution in the stellar mass function and the distribution of specific star-formation rates as a function of the local mean over-density, to extend known trends between quenching and environment at $z < 1$. There are tantalizing clues that the sign of the morphology-density relation may change at higher redshift, with strong star formation occurring in proto-cluster cores at $z \gtrsim 2$ (e.g., Wang et al. 2016). We can also test whether the 3D location in the web (e.g. distance from the nearest filament) plays an additional role in affecting galaxy properties at a range of epochs (Laigle et al. 2018).

Finally, on smaller spatial scales, the connection between the galaxies and their host DM halos has provided a compelling framework to understand the overall efficiency of galaxy formation (e.g., Wechsler & Tinker 2018). The most basic measure of this relation is the stellar mass-to-halo mass (SMHM) relation, which captures the overall efficiency of star formation over the entire history of the Universe (Behroozi et al. 2013). This relation is often derived using two-point statistics to compare the biased clustering of galaxies at a given stellar mass to compute the average masses of host DM halos (upper panel of Figure 13). The default analytic models used to describe the "galaxy-halo connection" rely on deterministic mappings (including scatter) between $M_{\rm halo}$ and M_* (e.g., Berlind & Weinberg 2002), but increasing evidence suggests that additional secondary factors, such as relative halo assembly history, are important in driving the timing and efficiency of galaxy formation. Empirically, this "assembly bias" manifests as stronger clustering of older (or less-star-forming) galaxies at fixed stellar mass (lower panel of Figure 13) (e.g., Gao & White 2007). No other photometric or spectroscopic survey at $z > 1$ would have the necessary statistics, accurate 3D positions, stellar masses, star formation rates, and halo masses derived from clustering measurements and halo occupation distribution models (e.g., Durkalec et al. 2015; Kashino et al. 2017) to measure the SMHM relation and test for the importance of assembly bias in understanding the galaxy-halo connection in the early Universe.

6.4. *How do gas and metals flow into and out of galaxies?*

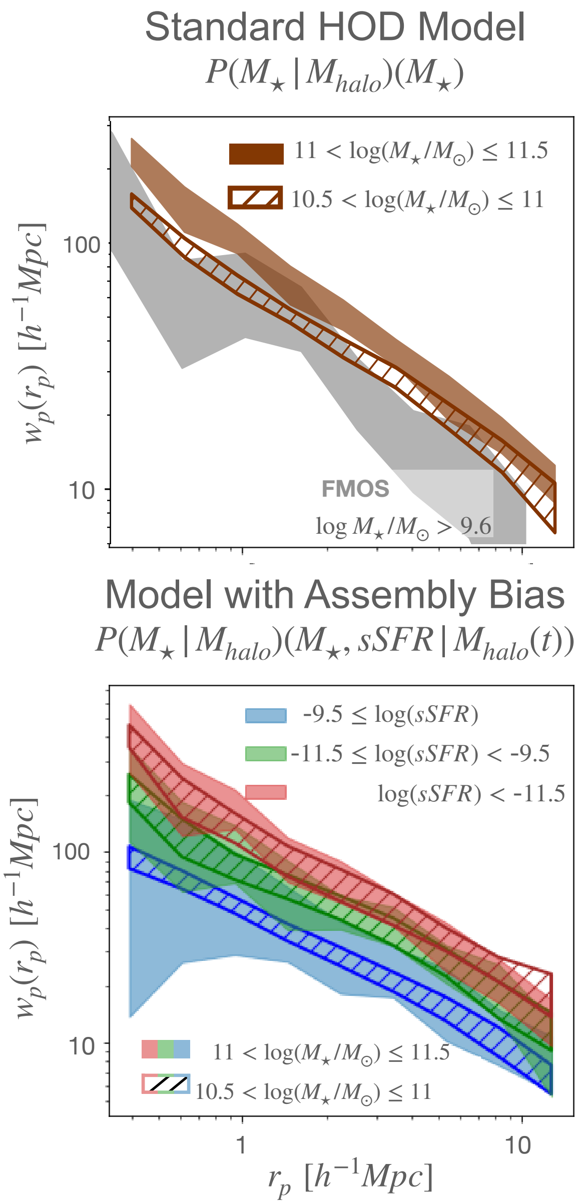

Figure 13. Two-point correlation functions of spectroscopic samples of galaxies provide a robust statistical measurement of host DM halo mass, thus constraining the SMHM relation; PFS will constrain this relation from $0.7 \lesssim z \lesssim 4.5$. Furthermore, we will test models of the overall efficiency of galaxy formation, testing the existence of assembly bias in the mapping from galaxy stellar mass to halo mass.

Galaxies grow primarily through the accretion of gas from the cosmic web. This inflow fuels new star formation and black hole growth, which in turn can drive outflows that may change the dynamical and thermal state of the inflowing gas. This cycle likely plays a key role in the self-regulation (and quenching) of star formation and black hole growth. The PFS galaxy evolution program is designed to document these flows by acquiring spectra of about 360,000 galaxies from redshifts ~ 0.7 to 5.5. This will enable us to quantify the strength and prevalence of outflows on galactic and circum-galactic scales, and seek evidence for gas inflows with the CGM.

With PFS, feedback from both massive stars and AGN can be characterized by measuring the incidence rate and outflow velocities of warm ionized gas as traced by blue shifted interstellar absorption lines. This will require stacking to achieve the necessary S/N, but the PFS sample size is so large that the stacking can be done in many bins in the 4D space of redshift, stellar mass, SFR, and AGN luminosity. This will enable direct tests of competing feedback models: momentum-driven (e.g., Murray et al. 2005) vs. energy-driven winds (e.g., Chevalier & Clegg 1985), that predict how outflow velocities should depend on these quantities.

The interface where the inflow meets feedback is the CGM, a region with a scale of roughly the virial radius, and which contains a baryonic mass comparable to the stellar component (Tumlinson et al. 2017). PFS will probe the CGM around the $z\sim1$ continuum-selected galaxy sample using the Lyman-α tomography sample as backlights, reaching expected equivalent widths of 0.3 Å within 200 kpc impact parameters for 100-galaxy stacks. The Cosmology sample will also be probed by SDSS quasars as backlights, reaching 0.10 Å equivalent widths in the stacked spectra. At intermediate redshifts, there is tantalizing evidence for outflows in the region of the CGM located along the minor axis of the galaxy, and inflows along the major axis (Lan & Mo 2018; Schroetter et al. 2019; Ho & Martin 2020). Our data, combined with HSC and Roman images, will allow us to map these anisotropic outflows and inflows and determine how they evolve between $z \sim 0.7$ to 1.6.

At the same time, as described in the next subsection, we will have access to the detailed star formation and chemical enrichment histories of the target galaxies to connect with these gas flows.

6.5. *How do tight relations between fundamental galaxy properties arise and evolve?*

Perhaps the most critical key to understanding the evolution of galaxies is the existence of tight correlations between all the most fundamental properties of the baryonic component of galaxies: mass, star-formation rate (SFR), size, velocity dispersion and/or rotation speed, and chemical composition. The PFS GE program will tackle this by providing a robust description of the nature of these relationships and their evolution over cosmic time. This is made possible by the size of the sample, its completeness, and the quality of the spectra. Here we highlight those aspects where we expect PFS to have the largest impact.

6.5.1. *Star-Formation Histories*

The bulk of star formation over cosmic time occurs in galaxies on the "Star Forming Main Sequence", a correlation between SFR and stellar mass (M_*) that evolves strongly towards higher SFR with increasing redshift (e.g., Speagle et al. 2014). While this evolution can be largely understood as tracing the overall cosmic rate of accretion and merging, the processes that lead to a relatively small dispersion in the relation at a given redshift are poorly understood. Additional populations lie above and below this relation; starburst galaxies responsible for $\sim$10% of the global star formation and populations of quenching and fully quenched galaxies dominate at the highest masses today. Understanding the mechanism(s) by which star-formation is quenched is especially important.

With the PFS dataset, the distribution of galaxies along and across the main sequence, and the fraction of star-forming, starburst, quenching, and quenched galaxies will be determined as a function of redshift. For the subset with deep (12 hour) spectra, the continuum spectra will hold critical information to describe higher order moments of the star formation histories

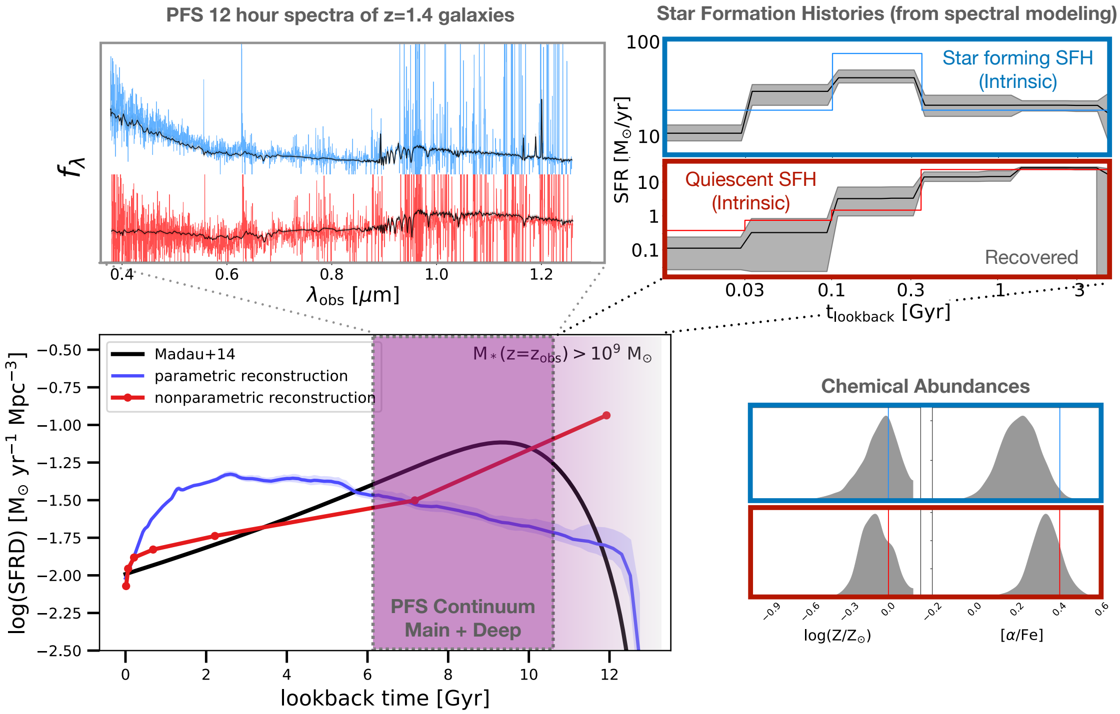

Figure 14. Star formation histories inferred from local galaxies fundamentally fail to capture the full growth of galaxies, and particularly diverge at Cosmic Noon (Adapted from Leja et al. 2019). PFS spectroscopy from the Deep sample (top left) will directly probe average and higher order moments of the instantaneous and recent ($\lesssim$2 Gyr) star formation histories at this crucial epoch. The red models represent non-parametric reconstructions (top right) that manage to recover the main features of the input star formation histories. [Fe/H] and [Mg/Fe] are recovered within the uncertainties as well.

of galaxies, where photometric measurements are fundamentally limited by the adopted priors (e.g., Carnall et al. 2019), as illustrated in Figure 14. Thus, we will begin to quantify the extent of ongoing star formation, the importance of rejuvenation, and time the quenching for >10,000 galaxies between $0.7 \lesssim z \lesssim 2$.

There is good evidence that the quenching process has evolved significantly between $z \sim 1$ and $z \sim 0$ (Behroozi et al. 2019). As described in Section 6.3, PFS will provide environmental metrics on scales from individual DM halos to large scales (e.g., filaments and voids) and galaxy star formation histories. This will be used to test the role of the environment in galaxy quenching.

We will also explore the role of AGN in halting star formation. The main sample of AGNs will be drawn directly from the galaxy sample, making it straightforward to quantify incidence rates in the 3D parameter space of stellar mass, SFR, and redshift (Kauffmann et al. 2004; Silverman et al. 2009). The measurements of star formation histories describe above will allow us to test the idea that powerful AGN are preferentially associated with rapidly-quenching galaxies (Wild et al. 2010). This will provide complementary insights to those gleaned from the direct observations of AGN-driven outflows described in Section 6.4 above. This sample will be supplemented by AGNs selected by a diverse set of multi-wavelength criteria, designed to fully probe the population of AGNs at these redshifts.

6.5.2. *Chemical evolution*

The chemical abundances of galaxies provide powerful constraints on their prior star-formation histories and on the roles of inflows of low-metallicity gas and outflows of high-metallicity gas (Maiolino & Mannucci 2019). Historically, the state-of-the-art for studying chemical abundances of galaxy populations has been the measurement of the correlation between galaxy stellar mass and metallicity (Garnett 2002; Erb 2008; Finlator & Davé 2008). With PFS, the statistical characterization of the mass-metallicity relation at $z \sim 0.7 - 1.7$ will for the first time be comparable to the analysis that has been possible for almost two decades at $z \sim 0$ using SDSS. This represents a significant advance over what is currently possible with smaller and more heterogeneously-selected samples at intermediate redshifts (e.g., Lamareille et al. 2009; Zahid et al. 2011). Because of the dramatic changes in galaxies' star-formation histories during this period, completing a detailed, robust census of enrichment as a function of galaxy properties will serve as an important benchmark for theoretical predictions.

In addition to single element gas-phase abundances like [O/H] or [Fe/H], PFS will also enable the determination of abundance ratios such as [O/Fe], [N/O], and [C/O] with sufficient S/N. Iron abundances can be determined from stellar continua in deep individual spectra or in spectral stacks. Both N and C are primarily measured using emission lines in individual galaxy spectra: the [N II]$\lambda\lambda$6549, 83 doublet can only be observed with PFS at $z \lesssim 0.9$, but beyond $z > 1.1$ the C III]$\lambda\lambda$1907, 9 and O III$\lambda\lambda$1661, 66 doublets can be used to determine [C/O] (Berg et al. 2019). The ratio of α abundances to Fe that we can recover from the Deep spectra (Figure 14) probe the most recent episode of star formation, distinguishing between contributions of Type Ia supernovas from low-mass stars with that of Type II from high-mass stars. Elements like C and N, which are thought to be formed in intermediate-mass stars, trace timescales in between core-collapse and Type Ia supernovae. With PFS, this analysis can be performed with stacked deep spectra in bins of stellar mass, star-formation rate, and, uniquely, with redshift.

6.6. *Summary and Connections with Galactic Archaeology and Cosmology Pillars*

We propose an ambitious galaxy evolution survey designed to tackle the most important questions about galaxy evolution. It will study half a million galaxies with $0.7 \lesssim z \lesssim 7$, in order to (i) probe the physics of the reionization of the universe, (ii) chart the co-evolution of the cosmic web, DM, and galaxies, (iii) detect and characterize the flows of gas into and out of galaxies, and (iv) connect together fundamental galaxy properties, including star-formation histories, gas-phase metallicities, outflows, and AGN content as functions of galaxy mass and redshift.

Our main science themes connect naturally with the goals of the PFS Cosmology and Galactic Archeology surveys. All themes rely on galaxies as a tracer of the underlying DM structure at different epochs. Our survey of galaxy evolution will chart the path of a galaxy like the Milky Way through time, while the Galactic Archaeology survey will focus in detail on the fossil record of the Milky Way and its massive neighbor Andromeda. The Cosmology survey is interested in evolution in the cosmic web on very large scales, using galaxies as baryonic signposts. The redshift range and galaxy masses probed by the survey are mapped by the Galaxy Evolution survey as well, especially in the Lyα tomography program. Moreover, the high-quality spectra from the GE survey will help us understand the properties of the cosmology tracer galaxies, ELGs. At the same time, the PFS team will exploit the large area of the cosmology survey to sample rare populations such as luminous AGN or foreground/background galaxy pairs needed to probe the CGM.

7. SURVEY DESIGN AND STRATEGY

We now provide a detailed description of the proposed Subaru Strategic Program (SSP) that will allow us to attain the science goals described in Sections 4–6 in the most efficient manner. We are proposing a 360 night survey to be undertaken over a 5 year period. The various science projects we discussed above fully utilize the capabilities of the unique PFS instrument we have constructed. They range from 15 minute exposures of emission line galaxies as tracers of LSS and probes of cosmology, to 12 hour exposures of more distant galaxies seen when the universe was still in its infancy. Likewise, our Galactic Archaeology program also exploits a purposely-designed medium resolution grating to provide accurate measures of kinematics and chemical abundances of stars in a range of nearby stellar systems. At this writing, the PFS instrument is nearing the end of engineering/commissioning observations. As we detail below, we have demonstrated that the instrument throughput, fiber pointing accuracy, and fiber configuration time are essentially at specifications, and that sky subtraction accuracy is close to photon-limited. While we have obtained data to test our target selection algorithms (Section 7.2.1), we anticipate refining these algorithms during the first year of the survey.

To construct a coherent and efficient observing program given the range of magnitude limits, target surface densities and exposure times, we have developed a detailed and highly-flexible software system to design our SSP program. Incorporating the expected and measured performance of the PFS instrument discussed below and the HSC-based photometric catalogs of our targets, we have constructed an end-to-end survey plan that takes full account of the necessary exposure times for each of the various components of our scientific plan and the visibility of the survey fields throughout each time allocation period, thereby ensuring realistic estimates of the overall completeness of the SSP during its survey lifetime. In the following we describe and illustrate each of the above points.

7.1. *Rationale*

Whereas it was organizationally helpful in Sections 4–6 to describe our scientific goals in terms of the three topics of cosmology, Galactic archaeology and galaxy evolution, as Figure 1 emphasizes, our program has an over-arching scientific theme addressing cosmic evolution and the role of the dark sector. This coherence is also reflected in our integrated survey plan which has been designed to exploit the numerous unique characteristics of the PFS instrument, the widely-distributed survey fields ensuring synergy with exquisite HSC imaging, and a range of target brightness essential for exploiting both dark and grey periods of allocated lunations.

We have designed PFS to be a versatile instrument enabling rapid on-sky re-configuration of the fiber positioner which is particularly necessary for an efficient survey of 4 million galaxies for the cosmology program. The high instrument throughput and exceptional wavelength coverage from 380nm through 1.26μm, together with Subaru's 8.2m aperture, offers unique opportunities for surveys of faint, high redshift galaxies for the galaxy evolution program. The Galactic archaeology program exploits both spectroscopic resolutions available and can make valuable use of grey time. Moreover, noting the shared survey fields, we can fully utilize PFS' multiplex gain by sharing fibers across different survey components. As with our scientific vision for the SSP, we have successfully integrated each survey component in an optimum manner. To downgrade any component would not only fail to fully exploit PFS, but would significantly reduce the efficiency of the overall program as well as weaken it scientifically.

Finally, our survey planning software also allows us to optimally prioritize components of our SSP survey for which there is competition from other massively-multiplexed spectroscopic instruments (discussed in Section 3). Since PFS has greater multiplex and wider FoV advantages and covers the blue spectral region, this will enable GE science that cannot be done by MOONS (see Section 6). Likewise, Subaru's 8.2m aperture ensures our planned PFS Galactic Archaeology program is not threatened by 4m facilities such as 4MOST and WEAVE. As discussed in Section 4, the primary challenge lies in PFS Cosmology where DESI is targeting similar science goals. Although a 4m telescope facility, DESI has a larger multiplex gain and a two year head-start on PFS. Our planning tool enables us to demonstrate how we can remain competitive with DESI whilst still achieving the required completeness for the overall program.

7.2. *Survey Parameters*

We begin with a brief overview of the integrated SSP. The PFS Cosmology program aims to observe four million emission line galaxies in the redshift range $0.8 < z < 2.4$ drawn from the 1100 deg^2 HSC Wide Survey with relatively short 15 minute exposures. The PFS Galactic Archeology (GA) component mostly targets high Galactic latitude fields, selected satellite dwarf galaxies and M31 making effective use of the medium resolution mode. The PFS Galaxy Evolution (GE) component is multi-facetted and involves a range of targets spanning the redshift range $0.7 < z < 7$ drawn from the HSC Deep Survey which, collectively, spans 15 deg^2.

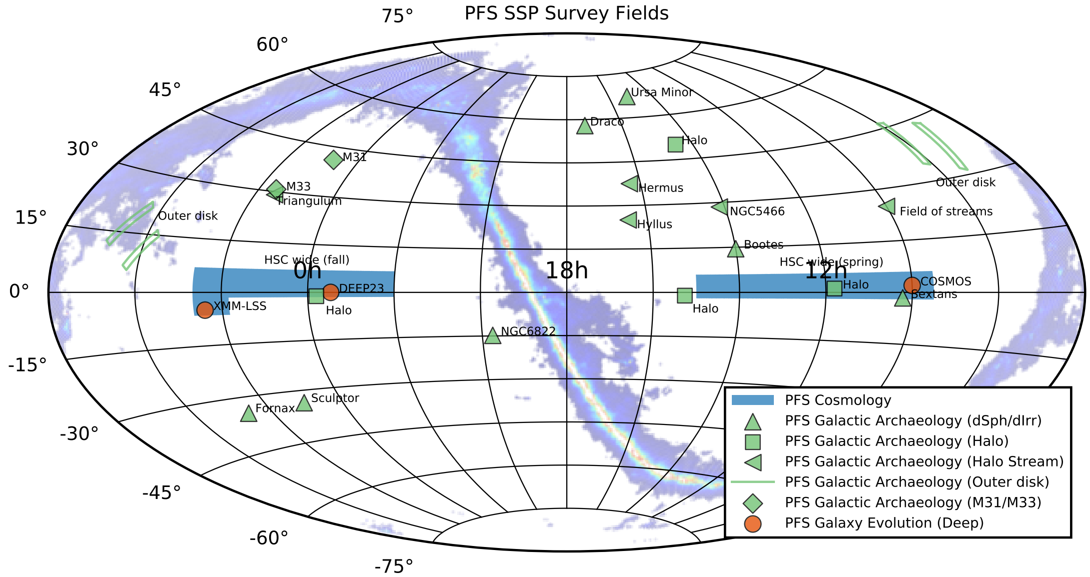

Figure 15. Sky distribution of the PFS survey fields. All targets are drawn from multi-color HSC data.

Table 5
Sample and Depths

Layer	Field	Selection	exp. time[a]	# of FoVs[b]	nights[c]	# of spectra	Requirement(s)[d]	Main science[e]
Cosmology	HSC-W	*grizy*	15 min	~ 1100	~70	~ 4M	redshift ([O II])	BAO, RSD, LSS
ancillary targets	HSC-W	*gri*(*zy*)+ext. data (*Gaia*, etc.)	15–30min	~ 1100	–	~ 100K	–	GA (stars, WDs), GE (e.g., QSOs)
gals $z \lesssim 1$	HSC-D	$i < 23$	2 hrs	11	~ 3.5	~ 28K	spectral features	GE (control sample, deep)
gals $0.7 < z < 1$	HSC-D	$y < 22.5+z_{\rm ph}$	2 hrs	11	~ 8.5	~ 68K	spectral features	GE ($0.7 < z < 1$)
gals $1 < z < 2$	HSC-D	$y < 22.5 + z_{\rm ph}$	2 hrs	11	~ 8.7	~ 69K	spectral features	GE ($1 < z < 2$)
	HSC-D	$y > 22.5, J < 22.8 + z_{\rm ph}$	2 hrs	11	~ 12	~ 96K	spectral features	GE ($1 < z < 2$, main)
gals $0.7 < z < 2$	HSC-D	$J < 22.8 + z_{\rm ph}$	12 hrs	11	~ 16	~ 14K	spectral features	GE ($0.7 < z < 2$, deep)
gals $2.1 < z < 2.5$	HSC-D	$y < 24.3 + z_{\rm ph}$	6 hrs	11	~ 8.3	~ 22K	spectral features	GE (IGM/foreground)
gals $2.5 < z < 3.5$	HSC-D	$y < 24.3, g < 24.2 + z_{\rm ph}$	6 hrs	11	~ 3.1	~ 8.3K	spectral features	GE (IGM/background)
	HSC-D	$y < 24.3, 24.2 < g < 24.7 + z_{\rm ph}$	12 hrs	11	~ 10.5	~ 14K	spectral features	GE (IGM/background)
gals $3.5 < z < 7$	HSC-D	$y < 24.5 + z_{\rm ph}$	6 hrs	11	~ 8.3	~ 22K	spectral features	GE (high-z)
$z \sim 2.2$ LAEs[f]	HSC-D	NB387, $L_{\rm Ly\alpha} > 3 \times 10^{42}$	3 hrs	11	~ 1.4	~ 7.4K	spectral features	GE, cosmic reionization
$z \sim 5.7, 6.6$ LAEs	HSC-D	NB816,921, $L_{\rm Ly\alpha} > 5 \times 10^{42}$	6 hrs	11	~ 1.7	~ 4.5K	redshift (Lyα)	cosmic reionization
	HSC-D	NB816,921, $L_{\rm Ly\alpha} = 3 - 5 \times 10^{42}$	12 hrs	11	~ 2.1	~ 2.8K	redshift (Lyα)	cosmic reionization
AGN $0.5 \lesssim z \lesssim 6$	HSC-D	$i < 24$(*grizy*)	1–4hrs	11	~ 1.8	~ 9.7K	spectral features	GE, CGM, IGM
MW-dSphs/dIrr[g]	HSC[h]	$g < 23$	3 hrs	48[i]	25.3	~ 60K	$S/N\vert_{\rm cont.} > 10$	DM profiles, [Fe/H] and [α/Fe] dist.
M31/M33[g]	HSC[h]	$i < 23$	5 hrs	52	33.4	~ 13K	$S/N\vert_{\rm cont.} > 10$	assembly history, DM subhalos, M33
MW[g]	HSC	$g < 22$	3 hrs	89	32.5	~ 26K	$S/N\vert_{\rm cont.} > 10$	MW grav., macro DM (incl. PBH)

Notes – [a] The total exposure time for each sample on source. [b] The number of pointings (roughly corresponding to survey area). [c] The primary requirement on spectroscopic observation for each sample. [d] The primary science drivers. [e] The main science. [f] The units of $L_{\rm Ly\alpha}$ are [erg s^{-1}]. [g] Medium-resolution mode spectroscopic observation is included. [h] Including NB515 narrow-band imaging to discriminate member giants from foreground dwarf stars. [i] Two visit observation for 18 pointings within nominal tidal radii to identify binary stars.

Table 5 summarises each sub-component of the Cosmology, GA and GE programs. This is the essential input into the survey planning software. The areal number density for each sub-component is estimated using the actual HSC photometric catalog together, for the Cosmology component, with the COSMOS mock catalog used to gauge the likely rate of occurrence of strong [O II] emission for the proposed photometric color selection. The software delivers, as its output, a semester-by-semester timetable of observations (survey field, target configuration, exposure time) and the running completeness for each component of the science program. In this section, we describe the necessary input data for this exercise and the assumptions made prior to defining a proposed plan over 5 years in the following subsection.

7.2.1. *Target selection and survey fields*

PFS observations for the Cosmology, GA and GE programs have targets selected from pre-existing HSC images. A summary of the survey fields for each of the Cosmology, GA and GE programs is provided in Figure 15. We now discuss the photometric selection and depths of the various components with reference to Table 5.

Cosmology program: We fully exploit the multicolor (*grizy*) imaging data of the HSC-Wide area over 1100 deg^2 with depths *gri* $\simeq$ 26 (5σ detection for a point source as shown in Aihara et al. 2018b) to optimally and securely select targets of [O II] emission-line galaxy candidates over the redshift range $0.6 < z < 2.4$. The wide wavelength coverage of the PFS red and near-infrared arms allows us to detect [O II] emitters over this large redshift range. In addition, the HSC depth minimizes contamination from photometric errors and ensures uniform sampling across different fields which is crucial for high-precision measurements of redshift-space galaxy clustering (Sunayama et al. 2020) (also see discussion in Section 4.3).

The survey will undertake pairs of 15-minute spectroscopic exposures in each pointing, yielding a total of ~ 4000 galaxy redshifts. Given the absence of reliable [O II] fluxes for the faint high-redshift galaxies we wish to target, we have adopted the improved COSMOS mock catalog, "EL-COSMOS" (Saito et al. 2020; Gao & Jing 2021) to develop our target selection strategy. From the mock catalog, we find that the following magnitude and color cuts securely select [O II] emitter candidates:

$$\begin{aligned}&23 < g < 24.5 \;\; \text{AND} \;\; g - r > 1.33g - 31.95\\&\text{AND NOT} \;\; (g > 23.8 \;\; \text{AND} \;\; r - i > 0.25)\\&\text{AND} \;\; (i - z > 0.286(g - r) - 0.014 \;\; \text{AND} \;\; 0 < g - r < 0.4).\end{aligned}$$

The first and third cuts select blue galaxies and remove those with weak emission lines and those outside the redshift range $0.6 < z < 2.4$, while the second condition prioritises galaxies at $z > 1.6$ (Takada et al. 2014). In this way 85% of the selected galaxies in the simulation have a predicted [O II] line strength consistent with a PFS S/N> 6, thereby yielding a precise redshift. However, the predicted constraints on [O II] emitters at $z > 1.5$ are less reliable and thus we propose to refine our target selection criteria once the commissioning observation or survey is underway. This can be efficiently done by analysing the spectra of a representative sample selected from wider magnitude-color cuts in the HSC catalog.

GA program: The Milky Way dwarf galaxies and M31 – The extragalactic portion of the GA program involves observations of individual giant stars distinguished from foreground Milky Way dwarfs using narrow-band HSC imaging data obtained via Keck/Subaru time exchange programs. The relevant narrow-band filter NB515 measures the gravity-sensitive Mg b triplet, weak in giants and strong in dwarfs, enabling a robust probabilistic separation. A final membership criterion will be based on a hierarchical Bayesian mixture model of the stellar populations in each dwarf galaxy and for the Milky Way foreground (Dobos et al. 2024) which incorporates all sources of uncertainty in a consistent statistical framework and includes ancillary information as priors. The application of deep neural networks and other machine learning techniques makes it possible to determine membership from quickly reduced, low signal-to-noise spectra. This will enable an adaptive targeting strategy whereby fibers originally assigned to stars that turn out to be non-members can be reassigned between exposures. Note that non-members that are field halo stars will continue to be observed. The PFS pointings for seven dwarf galaxies are listed in Table 2.

The Milky Way outer disk – The outer disk lines of sight are centered on Galactic longitudes of $\ell = 180°$ and $\ell = 90°$, with latitudes in the range $15° \le |b| \le 30°$, in bands of eleven contiguous PFS fields above and below the plane. Uniform Pan-STARRS photometry (PS1, Chambers et al. 2016) of sufficient depth and quality to be used for the selection of target FG main sequence stars to $g_{\rm HSC} \sim g_{\rm PS1} = 21$ is available for all such lines of sight. The targeted magnitude range $g_{\rm PS1} \sim 18 - 21$ corresponds to heliocentric distances of $\sim 6 - 25$ kpc. At these characteristic distances, a single PFS FoV corresponds to ~ 0.1 to ~ 0.6 kpc, respectively, and the planned observations probe vertical heights of $z \sim 2$ kpc to ~ 10 kpc. The estimated number of color-selected FG-MS stars brighter than $g_{\rm PS1} = 21$ ranges from $\sim 2,000$ to $\sim 9,000$ per PFS FoV (increasing with decreasing $|b|$ and ℓ). The PS1 photometry will be corrected for extinction as appropriate.

The Milky Way field halo – We select 8 halo fields: the fields reflecting Galactic rotation and radial motion [$(\ell, b) = (90°, \pm60°)$, $(270°, 60°)$ and $(0°, 45°)$] and the intermediate directions including halo streams, NGC5466 $(42°, 74°)$, Hermus $(70°, 44°)$, Hyllus $(55°, 43°)$ and Triangulum $(133°, -32°)$. Three contiguous PFS pointings are allocated to each field, with target stars selected from PS1 photometry to $g_{\rm PS1} = 22$. The majority of contaminating thin disk stars will be removed using multi-band colors, parallaxes and proper motions from PS1 photometry and *Gaia* astrometry. We expect ~ 1000 halo stars (main-sequence and red giants) beyond 10 kpc for most of the lines of sight. A similar strategy will be adopted for the pointings in the "Field of Streams".

GE program: The GE program has several components but all will be drawn from targets in three of the HSC-Deep fields; these contain multi-band near-infrared photometry to $J_{\rm AB} \gtrsim 23$ and Spitzer 3.6 and 4.5 μm IRAC data to similar depths [SERVS/DeepDrill, Lacy et al. (2021), Annunziatella et al. (2023), PI: M. Lacy, Mauduit et al. (2012), S-COSMOS, PI: D. Sanders, SPLASH, PI: P. Capak, Steinhardt et al. (2014), SpIES, Timlin et al. (2016), PI: G. Richards, Cycle 14 "Missing Piece", PI: A. Sajina]. U band data over 20 deg^2 to $U_{\rm AB} \sim 27$ mag (5σ) in sub-arcsec seeing has been taken from the CFHT Large Area U-band Deep Survey (CLAUDS) (Sawicki et al. 2019). For the Lyman α emitters surveys, Subaru narrow-band data is available at central wavelengths of 3870, 8160, and 9210Å.

Targeting for the continuum survey at $z < 2$ ("gals $z < 1$" to "gals $0.7 < z < 2$" in Table 5) will be based on HSC photometric redshifts using the $UgrizyJ$ + 3.6μm + 4.5μm photometry. Magnitude limits are determined by the band that contains the 4000Å break (e.g. y at $z < 1$, J at $z > 1$), to facilitate a uniform selection of galaxies by their total stellar mass. The depths are tuned such that we reach $\sim L_*(\sim 3 \times 10^{10}\, M_\odot)$ at $z \sim 1.5$. The sampling of 70% is set to ensure that we will have more than one spectrum per group in $M_{\rm h} \sim 10^{13}\, M_\odot$ groups, to give high-fidelity group catalogs.

Targeting for the IGM tomography survey ("gals $2.1 < z < 2.5$" and "gals $2.5 < z < 3.5$" in Table 5) is determined by the need to probe enough background sightlines ($\sim 1000\,{\rm deg}^{-2}$) to produce IGM maps that reconstruct the underlying matter density field at a Pearson coefficient of $r > 0.70$ over spatial scales of 3.9 cMpc. Galaxy targets at $z > 3.5$ ("gals $3.5 < z < 7$" in Table 5), primarily dropouts based on HSC photometry ($y < 24.5$), will be observed to reach a similar S/N of 2 per resolution element as the $z \sim 2.5$ tomographic sample. We plan to target all Lyman-α emitters at $z = 2.2, 5.7, 6.6$. This high sampling is needed to probe the correlations between sources and derive the spatial scale of reionization.

For the collective PFS program, in terms of Right Ascension (RA), the survey fields are widely distributed; some are accessible at any time during a given semester but, overall, there are fewer fields for observation during June and July when the Galactic plane is most prominent on the sky. In terms of scheduling, the survey requires slightly more nights in the autumn season (semester 'B'), largely as a result of the focus on the M31 halo region and the need to simultaneously maintain progress in the Cosmology and GE fields. Two dwarf galaxies, Fornax and Sculptor, have Declinations $\delta \simeq -40°$

reaching elevations of ≤ 30°. Careful scheduling is essential to ensure adequate data quality. Our survey planning software takes proper account of these and other constraints as indicated below.

7.2.2. *Completeness and fiber assignment*

Each of the three programs has specific requirements in order to achieve its respective scientific goals. The Cosmology program requires an efficient and fast survey operation and both a high completeness (fraction of photometrically-defined targets observed with PFS) and a high success rate (fraction of observed galaxies yielding successful redshifts). As the survey is magnitude limited, relative bright galaxies will be observed in grey time, drawing additional bright sources (quasars and extremely metal-poor stars) from other SSP components.

Much higher signal/noise spectra are required for stars in the GA program where bright and faint targets can be similarly assigned to grey and dark nights, respectively. However, in this case, there is less scope for fillers from other programs given the specific nature of the chosen survey fields. For the GE program, a uniform completeness (or sampling rate) with respect to the input photometric catalog is required for reliably tracing LSS and conducting statistical analyses without significant selection biases. Accurate sky subtraction (discussed in Section 8.1) will be critical in ensuring high-quality spectra for both the faintest high redshift targets and those for which reliable continuum measurements are needed. Most of the GE observations require dark nights.

An Exposure Targeting Software (ETS) simulates the fiber assignment to targets with a purposely-designed optimization algorithm that takes into account user-supplied priorities, the geometry of the focal plane, the configuration and patrol region of science fibers and the characteristics of each fiber including the risk of collisions. Where necessary, the schedule includes repeat visits and new fiber configurations to attain the required completeness. In this way is it possible to track, semester-by-semester, how the SSP survey is progressing to a satisfactory conclusion.

The GE component employs the same ETS, but optimizes the source-by-source trade-off between scientific usefulness and necessary exposure time. The latter is estimated from the S/N achieved for the relevant spectral features measured from multiple realizations of realistic noisy mock spectra. We are exploring a machine-learning approach to map photometric measurements from HSC onto proposed fiber assignments. It maximizes the overall scientific utility of the resulting sample achievable with the PFS fiber layout over the total time allocation. As an additional benefit of the end-to-end optimization of the fiber allocation process, the final sample selection can be understood and reproduced by the wider community from a given photometric catalog.

7.3. *Current PFS Performance*

The PFS team has been analysing the commissioning data to verify the performance of the various instrument components. In this section, we discuss performance metrics that validate the efficiency of PFS in the context of its targeted specifications.

7.3.1. *Demonstration of System Throughput*

The PFS team has determined the overall throughput of the entire system (atmosphere+telescope+PFS) based on the latest commissioning data (May 2024), as shown in Figure 16.

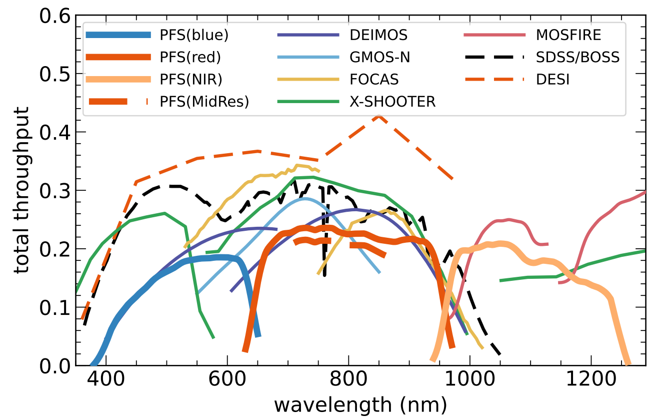

Figure 16. Total system throughputs for the PFS blue, red and NIR arms, based on commissioning data up to May 2024 (Yabe et al. in prep.). For comparison, we also show throughputs for selected spectrographs on other 8-10m facilities and the SDSS/BOSS spectrograph.

Satisfactorily, the measured throughput is within the margins of the original design specifications for each of the three spectrograph arms. As further commissioning data is taken and analysed, more accurate estimates will be determined enabling us to refine the survey strategy. However, we do not envisage significant changes at this stage.

The required exposure time for each type of target in Table 5 is based on an Exposure Time Calculator (ETC) developed by our team using a throughput consistent with the most recent measurements. The ETC incorporates a night sky model that includes both continuum and airglow emission lines, the elevation-dependent effects of seeing and atmospheric attenuation, lunar phase and moon-target distance, and the overall instrument throughput. A statistical error of 1% rms due to scattered light from the night sky is incorporated in calculations of the S/N (a detailed discussion of the sky subtraction performance of PFS is given in Section 8). The left panel of Figure 18 shows the limiting magnitude of continuum at a signal/noise S/N=5, after 3 pixel binning, in a 1 hour exposure as a function of wavelength.

7.3.2. *Demonstration of Fiber Positioning Performance*

Using the commissioning data in May 2024 run, the PFS team has verified, as shown in Figure 17, that each of the fiber positioners can be accurately placed to an accuracy of 17μm or better in the focal plane, corresponding to about 0.17 arcsec on the sky. This positioning accuracy includes the precision arising from field acquisition, auto-guiding and coordinate transformations between the guiding camera system, the Metrology system, and the focal plane of PFI. The overall accuracy is close to that in the original PFS specifications, verifying the validity of detailed algorithms developed for the system control software (see Section 3).

Furthermore, the commissioning data has also verified that the fiber configuration time for a new field is about 130 sec, again very close to the original specification (2 min). This reconfiguration time is sufficient to ensure a rapid survey speed for the PFS Cosmology program that has shortest exposures (15 min) among our programs.

7.3.3. *Spectral Performance of PFS*

Having demonstrated the actual performance of key PFS components, (i) the system throughput, (ii) the fiber positioning accuracy, and (iii) the survey speed (fiber reconfiguration time),

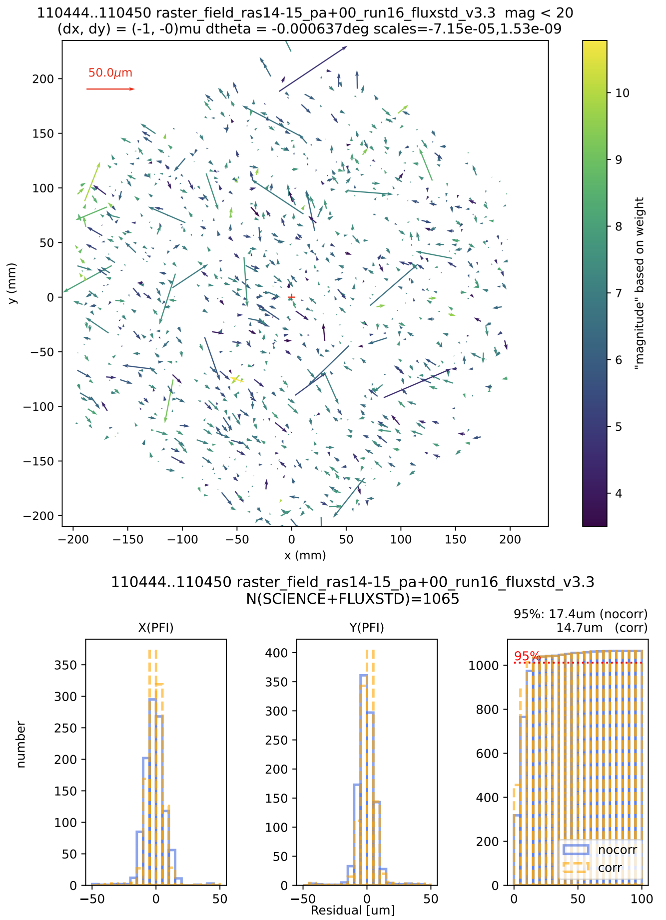

Figure 17. *Upper panel*: Results of a fiber "raster"-dither test undertaken in the May 2024 commissioning run: the observations were made at the fiducial pointing and each of the hexagonal vertices around the pointing center with a 1 arcsec pitch separation. Each arrow shows the amplitude and direction of the offset of each fiber in focal plane coordinates, reflecting the difference between the fiber position and the best-fit value estimated from the dither data. Different colors denote the magnitudes of the stars estimated from their measured spectrum, as denoted in the color bar. For reference, an offset of 50μm (0.5 arcsec) is indicated by an arrow in the upper-left corner. Note that the fiber diameter is 127μm (1.12 arcsec, see Table 1) and some large offsets likely arise from contamination by nearby bright stars. *Lower panel*: The histograms of the offset in the x- and y-axis directions. Note that "corr" denotes the residual after fitting the global trend incorporating shift, rotation and scale factors. The lower-right panel shows the cumulative distribution; about 95% of fibers achieved about 14.7μm position accuracy which is close to the original PFS specification.

we below discuss the required exposure time and show the simulated and actual spectra for each type of target in Table 5, using ETC. We discuss the quality of spectra and the data analysis tools we will use in order to justify the scientific practicality of our proposed PFS campaign.

In the case of the Cosmology program which targets [O II] emission-line galaxies, we adopt a detection threshold of S/N $\simeq$ 6 for a 15 min exposure for each target. The right panel of Figure 18 demonstrates the detection limit or selection function of [O II] emitters as a function of wavelength or the redshift of [O II] emitters based on the on-sky PFS performance (Figure 16).

For the GA targets, we will measure stellar parameters (v_r, $T_{\rm eff}$, [Fe/H], [α/Fe], etc.) using state-of-the art algorithms. We have developed two pipelines for this purpose: one based on physics-informed deep learning which delivers the radial velocities and the stellar atmospheric parameters, then a second pipeline, based on classical spectral synthesis, that delivers the elemental abundances.

The deep learning method builds a principal component analysis (PCA) over very high-resolution model spectra in each region. We feed the PCA coefficients to a Deep Learning Neural Net. This set of parameter values is then used to determine the radial velocity (v_r) with an optimized maximum likelihood code, based on point source detection (Kaiser 2004). We can predict the uncertainty in v_r from the Fisher matrix (Szalay et al. in preparation). A PCA expansion of the log fluxes in the vicinity of the best model spectrum, Doppler-shifted by the now established velocity, can be used with a neural net to infer the stellar atmospheric parameters. Finally, we estimate the log likelihood and the Fisher matrix around these parameter values with high precision. This technique will use the correlated patterns of different absorption lines, extracting features commonly used, rather than just using the raw pixels, and combines the speed and simplicity of Deep Learning with the rigor of accurate confidence intervals from well-understood statistical techniques.

From here, the second pipeline uses spectral synthesis (e.g., Kirby et al. 2010; Escala et al. 2019) to measure [Fe/H], [α/Fe], and individual abundance ratios. We can verify the measured abundances using synthetic spectra of K-giants (for the dSph and M31 projects) and G-dwarfs (for Milky Way studies) with metallicities between [Fe/H] = -2.0 and -0.5 in 0.5 dex increments, by using the spectrum synthesis code Turbospectrum (Plez 2012). The synthetic spectra scaled to various g-band magnitudes are then used to calculate continuum S/N ratios and simulated PFS spectra with an appropriate exposure time with the ETC under the assumption of a dark night and at the field center.

The upper panel of Figure 19 demonstrates the quality of spectra for a 3 hour exposure in medium-resolution mode for a K-giant. The lower panels show the expected statistical precision (excluding systematic errors expected to be of order 0.1 dex) of chemical abundances estimated from 100 realizations of the simulated spectra for each parameter combination. These measurement algorithms are discussed in Section 8. The PFS blue arm will provide carbon abundances (from the CH G-band at 4300 Å) and iron in very metal-poor stars (from a calibration of the Calcium I K line).

In the GE case, mock spectra are based on the 30-band COSMOS+UVISTA photometric catalog (Muzzin et al. 2013). Adopting the relevant redshift and apparent magnitude limits, these are matched to the PFS instrumental parameters. Stellar continua are based on the Bruzual & Charlot (2003) synthesis code using the MILES stellar library (Falcón-Barroso et al. 2011). Rest-frame optical emission-lines are included adopting prescriptions from Valentino et al. (2017) for physical properties derived from the COSMOS+UVISTA photometry. In the case of weaker lines, we adopt line ratios from Strom et al. (2017). In the rest-frame near-UV (185–300 nm), we exploit the SDSS-IV eBOSS survey (Dawson et al. 2016) using both emission-line galaxies (Comparat et al. 2016; Raichoor et al. 2017) and luminous red galaxies (Prakash et al. 2016). In the far-UV, to match the superior spectral resolution of PFS, we interpolate continuum-normalized spectra of $z = 1-3$ galaxies from Steidel et al. (2016). IGM absorption features are incorporated using the UVES Spectral Quasar Absorption Database (SQUAD; Murphy et al. 2019).

As shown in Figure 20, our mock spectra demonstrate the

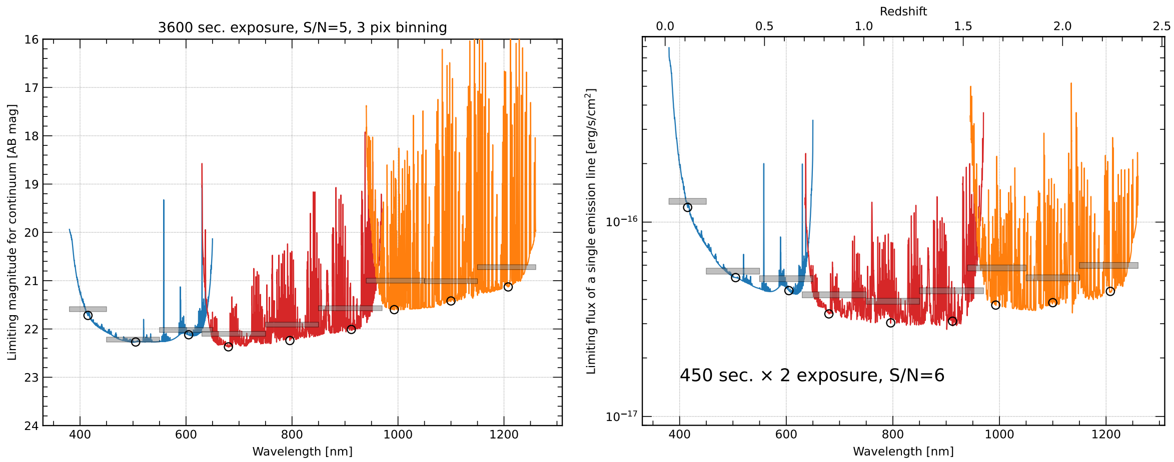

Figure 18. Left panel shows limiting magnitude for the continuum with 3 pixel binning in the wavelength direction for an on-source exposure time of 1 hour, while right panel shows the limiting flux of a single emission line corresponding to a S/N=6 for an on-source exposure time of 15 min (2×450 sec) as a function of wavelength or redshifts of [O II] emitters, which mimics the expected observation of the PFS Cosmology program. These results are based on the verified on-sky throughput in Figure 16. The gray horizontal bar indicates the average value within the range while the open circle shows the representative value at the specific wavelength where the spectrum is not affected by the sky line. The simulation assumes a seeing of 0.8 arcsec FWHM and a point source observed at new moon at a zenith angle of 45 degrees in 0.675 degrees from the field center. The fraction of incoming flux into the fiber aperture is assumed to vary from $\sim$ 62% at the field center to $\sim$ 54% at the field edge. Galactic extinction and fiber positioning error are ignored. The sky subtraction model assumes a systematic error of 1% and scattered light corresponding to 2% of the incoming sky flux. Detector dark currents [e$^-$/pix/s] are 0.0002 (blue and red) and 0.01 (NIR); read-out noise [e$^-$RMS/pix] are 3.0 (blue and red) and 4.0 (NIR).

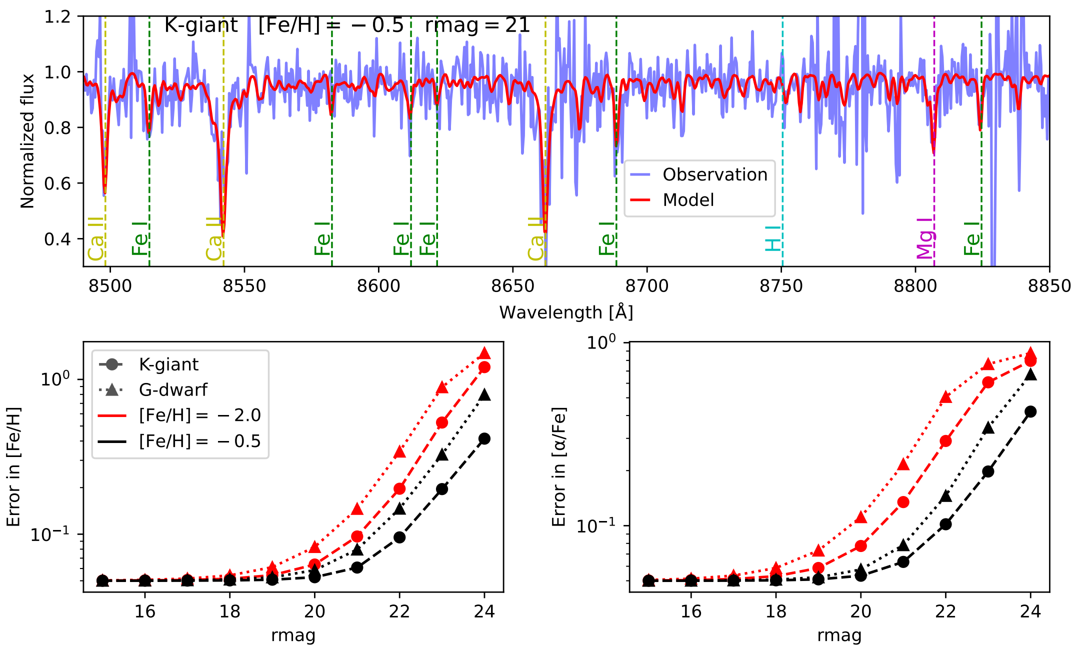

Figure 19. *Upper panel:* Small portions of a simulated observation of an r-mag 21 K-giant ($T_{\rm eff}$ = 4316 K, log(g) = 1.69) in a 3 hr exposure with PFS. The best-fit model is overplotted and some key atomic features are highlighted and labeled. *Lower left:* Expected errors in the inferred metallicity as a function of magnitude. The random errors are taken as the standard deviation of the best-fit parameters over 100 noise realizations. A systematic contribution of 0.05 dex derived from PFS commissioning observations of globular cluster member stars was added in quadrature. *Right right:* Corresponding results for α-enhancement. All simulations were carried out in the medium resolution mode.

required precision for key spectral diagnostics such as the 4000Å break, Hδ absorption equivalent width, emission flux, outflow velocities from features such as Mg II, and both stellar and gas-phase velocity dispersions. In combination with HSC photometry, we predict stellar masses to < 0.2 dex for $J_{AB} < 23$ and 4000Å break measures to 10% for most galaxies. Deeper 12 hour spectra will constrain Hδ equivalent widths to < 12% and enable stellar and gas-phase dispersions to < 25%. By stacking $\approx$ 100 galaxies we will be able to measure average outflow velocities in UV ISM absorption lines such as Mg II to better than $\approx$ 50 km/s enabling studies of feedback as a function of galaxy properties.

7.3.4. *Calibrations*

The ETC enables calculation of the required exposure time for a given S/N for any target given our demonstrated throughput (Figure 16), and our efficacy of sky subtraction (Sec-

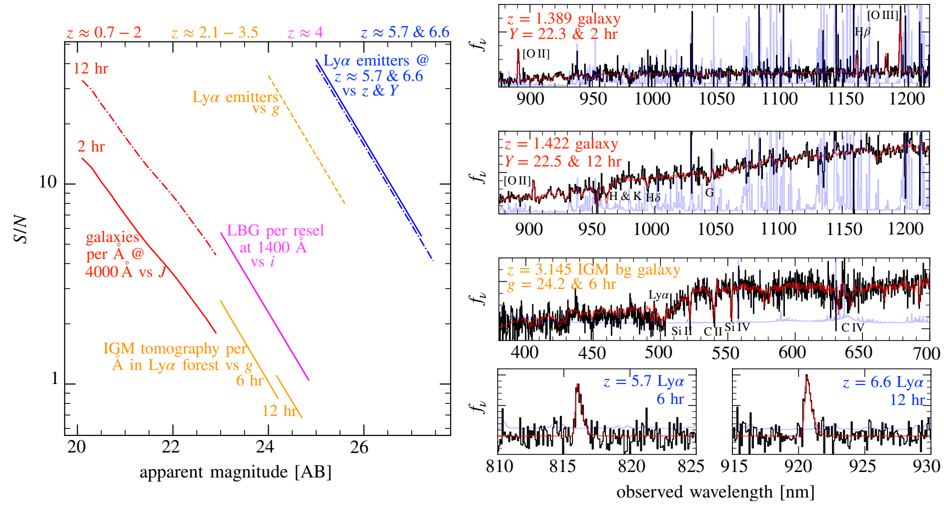

Figure 20. *Left panel*: Expected signal-to-noise ratio for key components of the Galaxy Evolution survey as a function of magnitude. Note that these calculations are based on an expected throughput that is indeed quite close to what has been delivered. Achieving this depth is critical to deliver our promised observables, as outlined in Table 6. *Right panels*: Expected spectral quality for galaxy types that the GE survey will target with the simulated spectrum in black, the expected 1-sigma error array in blue, and the best fit model in red. From top to bottom, the panels show a star-forming galaxy at z = 1.389, a quiescent galaxy at z = 1.422, an IGM tomography background galaxy, and two examples of Lyα emitters at z = 5.7 (left) and 6.6 (right). The top three panels are binned for display purposes by a factor of 5, 7, and 4 times the native PFS pixel scale, respectively. The panels are labeled with their exposure times, and the continuum selected galaxies (top three) are also labeled with their apparent magnitudes.

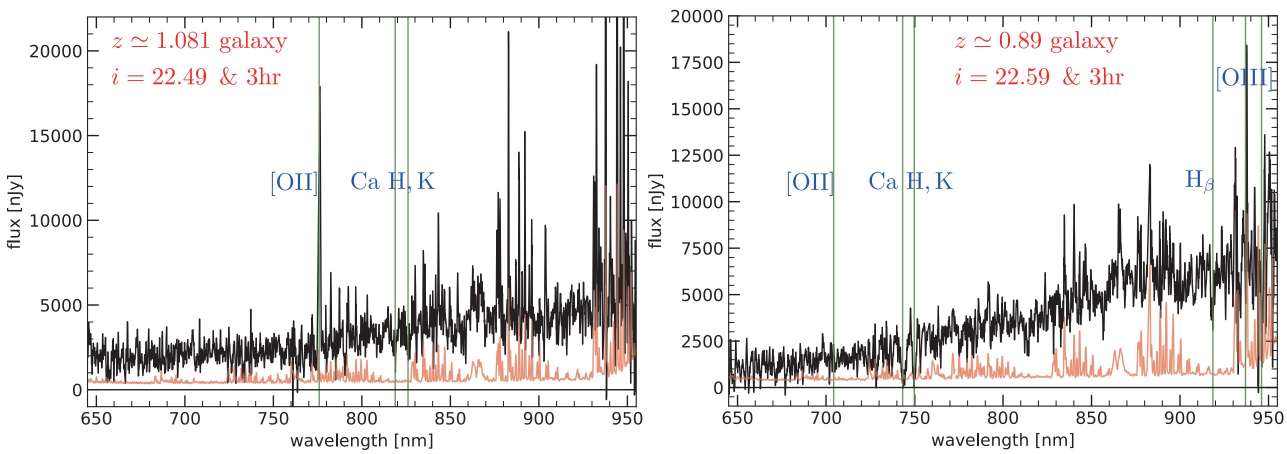

Figure 21. Representative examples of "on-sky" emission- and absorption-line spectra for $i \sim 22.5$ galaxies with about 3 hour exposures, obtained from PFS commissioning observations. These can be compared in quality with the simulated spectra in Figure 20. Here we used the PFS data reduction pipeline to obtain the spectra, and used the 5 and 7 pixel binning scheme in the left and right panels, respectively, similarly to the right-top two panels in Figure 20. Some key features are highlighted. The red curve in each panel denotes the statistical noise level.

tion 8.1). However, a full demonstration of the performance of PFS requires on-sky observations, especially for the more demanding SSP programs which include redshifts and emission line measures for the faintest, highest redshift galaxies, and absorption line studies of brighter, intermediate redshift sources. Due to the challenges of weather and technical issues with the Subaru primary mirror, we have obtained only a limited number of exposures of up to three hours integration on faint targets. Nonetheless, the resulting spectra demonstrate adequate calibrations with wavelengths accurate to 1-2 km/s and relative fiber-to-fiber throughputs calibrated to better than 1%. This follows precise dark/bias corrections, wavelength calibration and dome flat exposures taken during the daytime before and after each observing night for every science fiber. For dome flats, we have constructed a special screen and arc lamp system which ensures a uniform illumination. Figure 21 shows representative examples of both emission and absorption line spectra of $i \sim 22.5$ galaxies with 3 hour exposures obtained from commissioning observations. These faint spectra represent the most challenging aspects of the PFS-SSP survey, and can be readily compared in quality with the simulations shown in Figure 20. The comparison demonstrates our data reduction pipeline ensures adequate calibrations with a sufficient signal-to-noise to measure the required spectroscopic features.

7.4. *Survey Strategy*

With the above inputs, we are able to develop an optimal survey strategy for a SSP of 360 nights conducted over 5 years. We assume a classical observing mode (i.e., SSP observations are not shared with other programs on a given night) and up to 10 non-contiguous nights every month spanning dark and grey time. Exposure times allow for airmass, moon phase and seeing variations (the latter based upon Maunakea statistics),

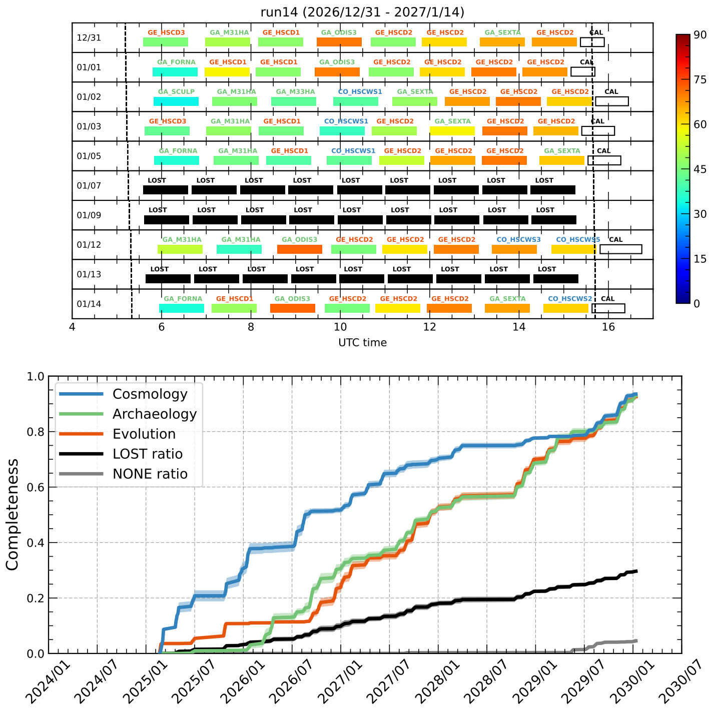

Figure 22. *Upper panel*: An example of night allocation of the PFS survey fields for one realization of the PFS survey assuming an allocation of 10 nights within each two weeks PFS run in Jan 2026. Observing blocks assigned to each survey component are shown by colored bars, where the color indicates the elevation angle of the observed component. The name of the observed survey component is labelled above each block, where CO_, GA_, and GE_ means the Cosmology, Galactic Archaeology, and Galaxy Evolution component, respectively, LOST means that the observing block was not observed due to lost to weather, and CAL means the blocs for taking calibration data. By having three programs, we can keep a high elevation of each target field for the PFS observation. *Lower panel*: A simulation of the survey completeness with allocated survey nights. Here, LOST is the ratio of lost observing time due to weather condition, NONE is the ratio of observing time which cannot be assigned to any fields. We take a survey strategy to prioritize Cosmology survey in early stage, but we secure ~10 nights each for Galactic Archeology and Galaxy Evolution survey, and we achieve the final completeness of $\gtrsim 95\%$ for all survey components.

and include all observing overheads (telescope slewing, instrument rotator, field acquisition, fiber positioner configuration and detector readout time). Finally we assume 30% of the nights are lost due to weather averaged over the entire survey.

Figure 22 presents a highly realistic plan for our proposed SSP program using the survey simulation techniques and input parameters discussed above. A variety of survey realizations (differing in random seeds of weather conditions and priorities of different target fields or science programs) demonstrate that the strategy robustly leads to >90% completeness over a 5 year 360 night survey for each of the Cosmology, GE and GA programs (lower panel of Figure 22).

Early priority is given to the Cosmology targets and GA dwarf galaxy targets, which have complementary RA distributions, to ensure that the PFS Cosmology is timely and remains complementary to DESI. This enables us to meanwhile fully evaluate and fine-tune the sky subtraction performance for the more demanding components of the GE program. Within the first two years we can still ensure at least $\simeq$5 nights per semester to the GE component which would lead to 20 – 30 K spectra; this is equivalent to the zCOSMOS catalog (~ 30 K spectra) that was collected over several years with VLT (Lilly et al. 2009). The early-year GE survey will spend these nights (i) obtaining 1-2 visits in each pointing, to secure LSS measurements and observe the brightest exemplars in all object classes, and (ii) probing the full color-space (i.e., without photometric redshift selection) of galaxies down to $J = 22.8$.

The major advantage of our survey planning software is its ability to rapidly adjust the survey strategy and re-prioritize targets to take account of (i) improved information on the target selection and the quality of PFS data obtained in early commissioning, (ii) survey progress as affected by weather losses or competition with independent projects, and (iii) other technical or time allocation changes. Our team will continue to maintain an optimal survey design to maximize the scientific returns given our science goals.

8. SOFTWARE AND SURVEY DELIVERABLES

The PFS project will deliver fully wavelength-calibrated, flux-calibrated and sky-subtracted spectra for each object observed, together with a meaningful estimate of the uncertainty per pixel. For galaxies, redshifts and their errors will be measured, in addition to emission-line strengths and properties. For targets with higher S/N spectra, we will additionally measure detailed spectral characteristics such as velocity dispersions and outflow velocities. For stars, we will measure radial velocities, surface temperatures, surface gravities, and metallicities, again with meaningful errors. These data, both calibrated spectra and tables of measured quantities, will be initially made available to collaboration members and the Japanese astronomical community, via a sophisticated database unifying HSC and PFS data, and then will be distributed to the world in public data releases. In what follows, we describe the software pipelines that will bring us from raw data to these measured quantities, the performance of the algorithms, and the database machinery we are building.

8.1. *Calibrated, Wavelength-Corrected, Sky-Subtracted Spectra*

Given the faintness of the star and galaxy targets that PFS will observe, the major challenge is to extract the spectra and accurately subtract the sky. For the wavelength range of the PFS, the sky spectrum is a smooth continuum with a large number of superposed bright emission lines, in particular from ~6000Å to the NIR end of the PFS coverage at 1.26μm, due to non-thermal rotational/vibrational transitions of the OH molecule (Rousselot et al. 2000; Hart 2019). Any given sky emission line observed through a single fiber will appear as a two-dimensional Point Spread Function (*PSF*) on the detector. Our approach is to forward-model the *detector map* (the two-dimensional position on the detector of a given wavelength through a given fiber), the *PSF*, and the intrinsic sky spectrum. We will then subtract the strongest few hundred lines of the sky spectrum, extract the object spectra, and then model and subtract the remaining sky continuum, weaker lines, and residuals using a PCA approach. This follows the spirit of the "Spectro-Perfectionism" approach (Bolton & Schlegel 2010), but with significantly smaller computational costs.

The spectral extraction code accurately maps the two-dimensional position of a given wavelength through a given fiber on a detector, and models the wings of the *PSF* to high accuracy, recognizing the modest overlap of the wings of the profiles of adjacent fibers on the detector (separated by only ~ 6 pixels from one another). The *PSF* is modeled including the contributions of telescope pupil illumination, optical aberrations in the spectrographic cameras, and focal ratio degradation (FRD) in the fibers. The code also measures the relative transmission of each fiber by referencing all flux measurements to the flux from a quartz flat-field exposure. This is then converted to physical units using flux standards observed in each field.

During commissioning of PFS, we assessed the accuracy of the sky subtraction algorithms through direct observations of the night sky, in which all fibers except for a small fraction reserved for engineering were pointed on blank patches of the sky (as selected from HSC imaging data). To test the sky subtraction routines, the background sky spectrum was determined from 10% of the fibers; the remaining 90% of the fibers were treated as science targets. In Figure 23, we show results from Spectrograph 1 of a single representative sky plate observed in the July 2023 commissioning run for a 450-second exposure. After fiber reassignment, there are 548 science fibers and 49 sky fibers.

Neglecting pixel-pixel correlations, the sky-subtracted spectra should be consistent with zero, retaining only the residuals of sky-subtraction, read noise, and Poisson noise. As a low-order test of sky subtraction quality, we consider each fiber's pixel-level distribution of χ, the ratio of the residual flux to the uncertainty in that pixel, estimated by the pipeline. The upper panels of Figure 23 shows these distributions separately for each arm for each of the 548 fibers. The distributions are well-described by a Gaussian centered at 0 with a standard deviation of 1. To simulate longer exposures, we averaged the sky-subtracted residuals across all 548 fibers, creating an effective exposure time of 2.5×10^5 seconds, almost 70 hours. The result is shown in the lower panel, and is compared with the average sky spectrum (gray line) scaled down by a factor of 100. This demonstrates that the remaining systematic errors in the sky subtraction are of order 1% of the sky flux, as we had hoped. Detailed tests (not shown) of the sky residuals show that the χ distributions remain close to Gaussian even in the cores of strong sky lines, and that there is no significant structure to the residuals associated with the lines. We anticipate that the results will continue to improve as we further refine our sky subtraction algorithms.

8.2. *Measurements of Redshifts and Spectral Properties*

The pipeline described above will deliver fully flux- and wavelength-calibrated 1D spectra of each object. The redshifts of galaxies will be measured with a code, "Algorithms for Massive Automatic Z Evaluation and Determination" (AMAZED; Schmitt et al. 2019), which has been used extensively for ground-based multi-object surveys such as those by VIMOS, and will be used to analyze data from the Euclid survey. AMAZED models galaxies as a superposition of continuum, emission lines, stellar and interstellar absorption lines, and including a model for the Lyα forest as a function of redshift. These models are fit to the data by minimizing χ^2, resulting in an estimate of the redshift and its uncertainty, as well as emission-line and absorption-line parameters. We have tested this approach extensively on simulated PFS spectra, which include realistic distributions of underlying galaxy populations from both the Cosmology and GE components of the survey. We have found that 90% of a simulated Galaxy Evolution sample (see Section 7.2) with $z < 2.1$ have measured redshifts with $\Delta z/(1 + z) < 5 \times 10^{-4}$, and 98% have errors less than 10^{-3} as shown in Figure 24. Similarly, 97% of a simulated sample of objects targeted with the Cosmology algorithm have correctly measured redshifts.

We have developed a separate dedicated pipeline to measure stellar atmospheric parameters (effective temperature, surface gravity, and Fe and alpha abundances) for objects in the GA survey, based on algorithms described in Escala et al. (2019) and Kirby et al. (2009). After shifting the spectrum to the rest frame using the radial velocity determined by our own code (Dobos et al. 2024) and normalizing by the continuum, the code fits the spectrum to a grid of synthetic spectra calculated based on the ATLAS9 (Kurucz 1993; Castelli et al. 1997) model stellar atmospheres. The code additionally makes use of photometric information for the stellar parameter determination by comparing them with stellar isochrone models. The performance of this pipeline is described in Section 7.2.

Table 6 summarizes main deliverables we measure from each of the PFS Cosmology, GA and GE programs.

8.3. *Database and Distribution*

As described above, the principal outputs of the pipelines will be fully calibrated 1D spectra of every object observed, as well as redshifts/radial velocities, emission and absorption line properties for galaxies, and effective temperatures, surface gravity, and metallicities for stars. In addition, extensive metadata from each PFS exposure, and intermediate data products (such as the calibrated spectra from each arm of the spectrograph) will be useful for science analyses. Furthermore, as PFS target selection is largely based on imaging data from HSC, the PFS data will need to be closely coupled to the HSC photometric catalogs. The database will also include extensive metadata from each PFS exposure, intermediate data products (such as the calibrated spectra from each arm of the spectrograph), and detailed targeting information.

We have developed an extensive data access framework built on a modern science platform to serve these massive datasets to the members of the collaboration and the Japanese astronomical community. The PFS science platform allows a user to access the HSC and PFS data directly with no overheads; the user can perform science analyses directly on the data and no massive data transfer is required to their local machine. Its capabilities complement the tools that the HSC collaboration has already built, such as `HSCMap`, a powerful visualization interface for the HSC images. The PFS science platform adds a file sharing service, a Jupyter notebook analysis system that allows notebooks to be executed in interactive mode, and a spectrum analysis tool called `Spectrum Viewer` that can be invoked in standalone mode as well as from a Jupyter notebook. The third generation of the prototype system has been released internally, and the system will be ready for extensive data analyses by the time the PFS survey begins.

The HSC collaboration has distributed the data from their 330-night survey in a series of public data releases (Aihara et al. 2018a, 2019). This has been highly successful; the data are being used by astronomers all over the world, and the public releases have significantly increased the visibility of the HSC survey. At this writing the HSC collaboration and the world-wide community has written over 500 refereed papers based on the survey. Building on the HSC experience and success, we plan to make fully public releases of PFS data to the world every other year through the five years of the PFS survey to further contribute to the world-wide community.

9. TEAM EXPERTISE & MANAGEMENT PLAN

Many team members have extensive experience in the management of large collaborative efforts including those of the

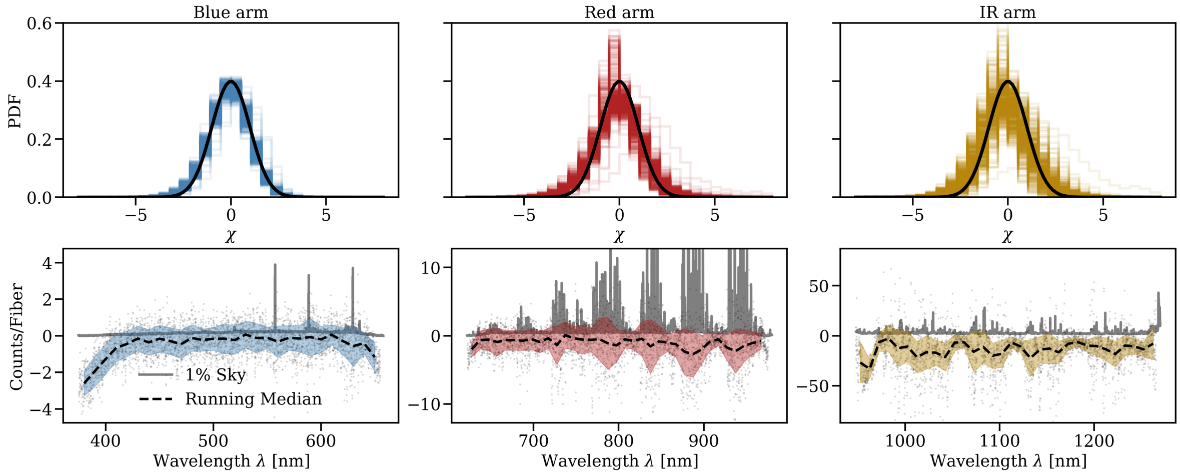

Figure 23. Sky subtraction diagnostics from a representative commissioning sky plate. *Top row*: summary of the χ distributions for the sky-subtracted spectra by spectrograph arm; each of the 548 curves is the pixel level χ distribution for a single fiber. The columns correspond to the blue, red, and near-infrared arms of the spectrograph, respectively. A Gaussian centered at 0 with a standard deviation of 1 is plotted as a black line. *Bottom row*: the average over 548 spectra (corresponding to a total exposure time of almost 70 hours) of sky-subtracted residuals is shown as gray points; the running median and 1σ confidence interval are shown as a dashed line and the shaded region, respectively. For reference, the gray line is a high-signal sky spectrum scaled down by a factor of 100.

Table 6
Deliverables of PFS SSP Survey

Sample	z-range	#	Deliverable	Precision	Note
[OII] ELGs	$0.8 \le z \le 2.4$	$\sim$ 4M	z	$\Delta z/(1+z) \lesssim 5\times10^{-4}$	$\gtrsim$ 70% success rate
			$f_{[\mathrm{OII}]}$	$\Delta f_{[\mathrm{OII}]}/f_{[\mathrm{OII}]} \lesssim 0.2$	
$0.7 < z < 1.7$ gals	$0.7 < z < 1.7$	~200K	z	$\Delta z/(1+z) \lesssim 5\times10^{-4}$	~90% sampling rate
			M_*, SFR, τ_*, b, (O/H), v_{outflow}	$S/N \approx 2\,\text{Å}^{-1}$, for the main sample	
			[Fe/H], [α/Fe], T_e	$S/N \approx 6\,\text{Å}^{-1}$, for the deep sample	
$z \gtrsim 2$ gals	$2.1 \le z \le 7$	$\sim$ 60K	z	$\Delta z/(1+z) \lesssim 10^{-3}$	$\sim$ 75% sampling rate
			τ_{L_α}, M_*, SFR, b, (O/H), v_{outflow}	$S/N \approx 2\,\text{Å}^{-1}$	
LAEs	$z = 2.2, 5.7, 6.6$	$\sim$ 15K	z	$\Delta z/(1+z) \le 10^{-3}$	$\sim$ 100% sampling rate
			f_{L_α}	$S/N \approx 10$	
stars in MW/dSphs/M31	$z = 0$	$\sim 75K$	radial vel.	3–10 km/s	
			[Fe/H], [α/Fe]	0.2	

highly successful Subaru Hyper Suprime-Cam campaign, the Sloan Digital Sky Survey, the AAT 2 degree Field Redshift Survey and the HST-based COSMOS survey. We have structured our PFS management plan based upon lessons learned from the foregoing surveys and closely followed the arrangements that worked successfully for the HSC SSP.

The overall PFS SSP operation and issues related to instrument performance will be overseen jointly by the PFS Project Manager, Naoyuki Tamura (NAOJ), the Commissioning Observation Lead, Yuki Moritani (NAOJ), and the Survey Operation Lead, Kiyoto Yabe (NAOJ). The data pipeline and processing will be overseen by Robert Lupton (Princeton) and Kiyoto Yabe, and data archiving managed by Masayuki Tanaka (NAOJ). The PFS science program and its priorities will be overseen by co-science leads Masahiro Takada (Kavli IPMU) and Richard Ellis (UCL). Any issues related to the interests of the international PFS science team will be addressed by PFS Steering Committee comprising a member from each participating institution and NAOJ chaired by Hitoshi Murayama (Kavli IPMU). Issues related to the participation of the Japanese community can be relayed through the Subaru Advisory Committee (SAC) to both NAOJ and the Steering Committee.

As discussed in Section 8, all data will be distributed simultaneously to the international PFS team members and, after an agreed proprietary period, to the global astronomical community via a sophisticated database at NAOJ, similar to that developed for the HSC collaboration (Aihara et al. 2019). The proposed SSP plan (Figure 22) will enable important scientific progress from each component (Cosmology, GE and GA) using the first year of data, thereby stimulating the PFS team to work continuously as more data arrives. Our team is already organized in highly structured working groups around the broad science themes described in this proposal as well as ones responsible for technical aspects, publication and team membership policies. All PFS team publications will be subject to a collaboration-wide data policy, with clear guidelines on communication and authorship that encourage junior scientists to lead scientific projects and become first authors on the resulting papers.

10. ANCILLARY SCIENCE

Clearly a powerful instrument such as PFS SSP will provide unique opportunities for ancillary science beyond the main focus of the SSP described in this proposal. As the Cosmology program will undertake a comprehensive campaign over about 1100 deg^2, it offers the opportunity for spectroscopic observations of additional rare bright objects thereby strengthening synergistic aspects of our scientific themes (see Figure 1). Examples where the Cosmology survey can lead to such syn-

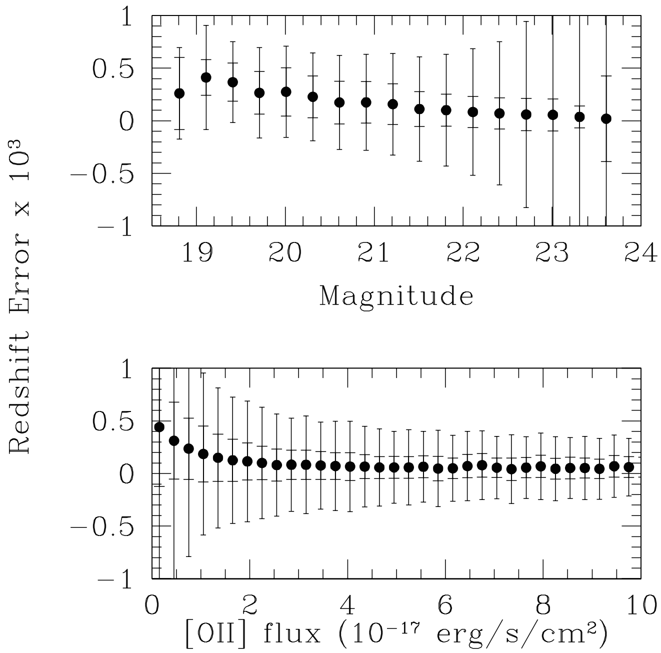

Figure 24. The median (points), interquartile range (smaller errorbars) and range including 90% of the points (larger errorbars), of the difference between true and inferred redshift for a sample of simulated GE galaxies (Section 7.2). Results are shown as a function both of galaxy magnitude and [OII] emission-line strength. The vast majority of galaxies have redshifts determined to within $|\Delta z| = 10^{-3}$.

ergies include studies of (i) AGN/quasar candidates identified from multi-color HSC datasets (Matsuoka et al. 2018) providing complementary information on the co-evolution of super massive black holes and their host galaxies, (ii) low-surface brightness galaxies (Greco et al. 2018) uniquely identified by HSC datasets whose redshifts will aid in studies of this intriguing population, (iii) galaxies/quasars in strong lens systems (Sonnenfeld et al. 2019) whose characterization will lead to improved constraints on the Hubble constant (H_0), complementing those derived from baryonic acoustic oscillations derived from the primary cosmology program, and (iv) extremely metal-poor halo stars and white dwarfs whose physical properties and radial velocities will complement studies in specific fields in the GA program.

Additional "ancillary science" targets are collated from PFS team members and prioritised for each pointing in the Cosmology survey. Our fiber assignment algorithm has the capability of prioritising cosmology targets ([O II] emitter candidates) and ancillary targets in order to ensure the required completeness and success rate of the former whilst avoiding biases arising from their 'artificial clustering'.

The PFS team recognizes there are likely to be many Open Use requests for PFS observations in the popular COSMOS and SXDS GE fields. By design however, it is unlikely that our GE campaign will have any spare fibers for such observations to be added, even if the relevant exposure times were to match. However, if the Subaru Advisory Committee requests some form of coordination of the SSP with such Open Use programs, it may be possible to re-arrange the SSP GE strategy to accomplish such a trade, so long as the total SSP time remains unchanged via subsequent allocations of time and the GE survey is optimally completed within the SSP survey period.

Finally, the team requests that the Subaru TAC protects the dwarf galaxy pointings in the GA program from Open Use programs. The selected dwarf galaxies (see Table 2) represent a flagship science component of the PFS SSP which could be readily challenged by even a single night's observation. No such protection from Open Use science programs is requested for the GE and Cosmology fields. The team is likewise willing to accept Target-of-Opportunity (ToO) observations in all SSP survey fields.

The combination of Subaru HSC and PFS data will deliver a unique legacy value. The team has been developing a science database whereby pipeline products of PFS data, together with the associated HSC images are available[3]. This development is partly funded by a US National Science Foundation MSIP (Mid-Scale Innovations Program in Astronomical Sciences) led by team members at JHU, Princeton and Caltech. The database will have an online image browser interface, extending the existing one `hscMap`, thereby providing a user-friendly environment to browser the extensive combined HSC and PFS dataset. This will bring considerable benefits to facilitate and maximize the science return from both HSC and PFS surveys.

11. CONCLUDING REMARKS

Following more than 15 years of instrument design and construction, scientific planning, software design and both national and international fund-raising, the PFS team is enthusiastically ready to embark on an ambitious, but demonstrably practical, SSP survey that fully utilizes PFS's unique wide-field and massively-multiplex spectroscopic capabilities at the prime focus of the 8.2 m Subaru aperture on Maunakea. Our proposed survey promises unrivalled and dramatic progress in three broad areas: the nature of dark energy and dark matter (including the neutrino mass), the assembly history of the Milky Way and our nearest neighbouring galaxies M31, and a comprehensive census of galaxy properties over a wide range in redshift ($0.7 \lesssim z \lesssim 7$). This program will be an outstanding legacy of the Subaru telescope that will propel further scientific endeavors in the era of Extremely Large Telescopes and next-generation panoramic surveys such as the Vera Rubin Observatory (LSST), ESA's Euclid mission and the NASA Roman Space Telescope.

ACKNOWLEDGEMENTS

We would like to dedicate this proposal to the memory of Profs. Naruhisa Takato and Olivier Le Fèvre, who were crucial individuals in the PFS project. Olivier had a strong scientific vision especially in high-redshift science as well as expertise in instrumentation that made it possible for the dedicated team of engineers at LAM to work on the PFS. Under his leadership, LAM has been making crucial contributions to the developments of spectrograph system and 1D pipeline, aspects at the heart of the PFS endeavor. The PFS project has taken more than 15 years from the launch to completion. The PFS team acknowledges various financial contributions: the Funding Program for World-Leading Innovative R&D on Science and Technology (FIRST program: PI: H. Murayama), contributions from the participating international institutions and groups (ASIAA, Brazilian PFS Participation Consortium, Caltech/JPL, Chinese PFS Participation Consortium, JHU, Kavli IPMU, LAM, MPA/MPE, NAOJ, USA North-East Participation Group, Princeton), the KAKENHI Grant-in-Aid for Scientific Research on Innovative Area (PI: H. Murayama), NSF's

[3] See `https://hscdata.mtk.nao.ac.jp:4443/hsc_ssp/` for the HSC database.

Mid-Scale Innovations Program in Astronomical Sciences (PI: M. Strauss), and KAKENHI Transformative Research Area (A) (PI: H. Murayama).

REFERENCES

Abdalla, E., et al. 2022, Journal of High Energy Astrophysics, 34, 49
Addison, G. E., Bennett, C. L., Jeong, D., Komatsu, E., & Weiland, J. L. 2019, ApJ, 879, 15
Aihara, H., et al. 2018a, PASJ, 70, S8
—. 2018b, PASJ, 70, S4
—. 2019, PASJ, 71, 114
Alam, S., Miyatake, H., More, S., Ho, S., & Mandelbaum, R. 2017, MNRAS, 465, 4853
Alam, S., et al. 2021, Phys. Rev. D, 103, 083533
Allison, R., Caucal, P., Calabrese, E., Dunkley, J., & Louis, T. 2015, Phys. Rev. D, 92, 123535
Amon, A., et al. 2018, Mon. Not. Roy. Astron. Soc., 479, 3422
Amon, A., et al. 2022, Phys. Rev. D, 105, 023514
Annunziatella, M., et al. 2023, AJ, 166, 25
Arnaboldi, M., et al. 2022, A&A, 666, A109
Asgari, M., et al. 2021, A&A, 645, A104
Ata, M., Kitaura, F.-S., & Müller, V. 2015, MNRAS, 446, 4250
Bayer, A. E., et al. 2021, ApJ, 919, 24
Behroozi, P., Wechsler, R. H., Hearin, A. P., & Conroy, C. 2019, MNRAS, 488, 3143
Behroozi, P. S., Wechsler, R. H., & Conroy, C. 2013, ApJ, 770, 57
Belokurov, V., Sanders, J. L., Fattahi, A., Smith, M. C., Deason, A. J., Evans, N. W., & Grand, R. J. J. 2020, MNRAS, 494, 3880
Belokurov, V., Vasiliev, E., Deason, A. J., Koposov, S. E., Fattahi, A., Dillamore, A. M., Davies, E. Y., & Grand, R. J. J. 2023, MNRAS, 518, 6200
Berg, D. A., Erb, D. K., Henry, R. B. C., Skillman, E. D., & McQuinn, K. B. W. 2019, ApJ, 874, 93
Berlind, A. A., & Weinberg, D. H. 2002, ApJ, 575, 587
Bernal, J. L., Verde, L., & Riess, A. G. 2016, J. Cosmology Astropart. Phys., 10, 019
Bianchi, D., & Verde, L. 2020, MNRAS, 495, 1511
Bird, J. C., Loebman, S. R., Weinberg, D. H., Brooks, A. M., Quinn, T. R., & Christensen, C. R. 2021, MNRAS, 503, 1815
Blake, C., et al. 2016, MNRAS, 456, 2806
Blake, C., et al. 2020, Astron. Astrophys., 642, A158
Bolton, A. S., & Schlegel, D. J. 2010, Publications of the Astronomical Society of the Pacific, 122, 248
Boyle, A., & Komatsu, E. 2018, J. Cosmology Astropart. Phys., 3, 035
Bruzual, G., & Charlot, S. 2003, MNRAS, 344, 1000
Burkert, A., et al. 2016, ApJ, 826, 214
Cai, Y.-C., Padilla, N., & Li, B. 2015, MNRAS, 451, 1036
Carnall, A. C., Leja, J., Johnson, B. D., McLure, R. J., Dunlop, J. S., & Conroy, C. 2019, ApJ, 873, 44
Castelli, F., Gratton, R. G., & Kurucz, R. L. 1997, A&A, 318, 841
Chambers, K. C., et al. 2016, arXiv e-prints, arXiv:1612.05560
Chan, H. Y. J., Ferreira, E. G. M., May, S., Hayashi, K., & Chiba, M. 2022, MNRAS, 511, 943
Chevalier, R. A., & Clegg, A. W. 1985, Nature, 317, 44
Chiang, B. T., Ostriker, J. P., & Schive, H.-Y. 2023, MNRAS, 518, 4045
Choudhury, S. R., & Hannestad, S. 2020, J. Cosmology Astropart. Phys., 2020, 037
Chudaykin, A., & Ivanov, M. M. 2019, J. Cosmology Astropart. Phys., 2019, 034
Comparat, J., et al. 2016, A&A, 592, A121
Croton, D. J., et al. 2006, MNRAS, 365, 11
Dalal, R., et al. 2023, Phys. Rev. D, 108, 123519
D'Amico, G., Hamill, T., & Kaloper, N. 2016, Phys. Rev. D, 94, 103526
Dawson, K. S., et al. 2016, AJ, 151, 44
de Blok, W. J. G., & Walter, F. 2000, ApJL, 537, L95
de la Torre, S., et al. 2017, A&A, 608, A44
Deason, A. J., Belokurov, V., Koposov, S. E., & Lancaster, L. 2018, ApJL, 862, L1
Deason, A. J., Bose, S., Fattahi, A., Amorisco, N. C., Hellwing, W., & Frenk, C. S. 2022, MNRAS, 511, 4044
Deason, A. J., Fattahi, A., Frenk, C. S., Grand, R. J. J., Oman, K. A., Garrison-Kimmel, S., Simpson, C. M., & Navarro, J. F. 2020, MNRAS, 496, 3929
DESI Collaboration et al. 2022, AJ, 164, 207
—. 2024, arXiv e-prints, arXiv:2404.03002
Dey, A., et al. 2023, ApJ, 944, 1
Dobos, L., et al. 2024, AJ submitted
Dodelson, S., Kaplinghat, M., & Stewart, E. 2000, Phys. Rev. Lett., 85, 5276
Dubois, Y., et al. 2014, MNRAS, 444, 1453
Durkalec, A., et al. 2015, A&A, 576, L7
Eisenstein, D. J., et al. 2005, ApJ, 633, 560
Erb, D. K. 2008, ApJ, 674, 151
Erkal, D., et al. 2019, MNRAS, 487, 2685
—. 2021, MNRAS, 506, 2677
Escala, I., Gilbert, K. M., Fardal, M., Guhathakurta, P., Sanderson, R. E., Kalirai, J. S., & Mobasher, B. 2022, AJ, 164, 20
Escala, I., Kirby, E. N., Gilbert, K. M., Cunningham, E. C., & Wojno, J. 2019, ApJ, 878, 42
Esteban, I., Gonzalez-Garcia, M. C., Hernandez-Cabezudo, A., Maltoni, M., & Schwetz, T. 2019, Journal of High Energy Physics, 2019, 106
Evans, T. A., Fattahi, A., Deason, A. J., & Frenk, C. S. 2020, MNRAS, 497, 4311
Falcón-Barroso, J., Sánchez-Blázquez, P., Vazdekis, A., Ricciardelli, E., Cardiel, N., Cenarro, A. J., Gorgas, J., & Peletier, R. F. 2011, A&A, 532, A95
Finlator, K., & Davé, R. 2008, MNRAS, 385, 2181
Förster Schreiber, N. M., & Wuyts, S. 2020, ARA&A, 58, 661
Freedman, W. L. 2017, Nature Astronomy, 1, 0121
Frieman, J. A., Hill, C. T., Stebbins, A., & Waga, I. 1995, Phys. Rev. Lett., 75, 2077
Gao, H., & Jing, Y. P. 2021, ApJ, 908, 43
Gao, L., & White, S. D. M. 2007, MNRAS, 377, L5
Garnett, D. R. 2002, ApJ, 581, 1019
Gilbert, K. M., Kirby, E. N., Escala, I., Wojno, J., Kalirai, J. S., & Guhathakurta, P. 2019, ApJ, 883, 128
Gilbert, K. M., et al. 2022, ApJ, 924, 116
Greco, J. P., et al. 2018, ApJ, 857, 104
Greene, J., Bezanson, R., Ouchi, M., Silverman, J., & the PFS Galaxy Evolution Working Group. 2022, arXiv e-prints, arXiv:2206.14908
Hahn, C., & Villaescusa-Navarro, F. 2021, J. Cosmology Astropart. Phys., 2021, 029
Hamaus, N., Cousinou, M.-C., Pisani, A., Aubert, M., Escoffier, S., & Weller, J. 2017, J. Cosmology Astropart. Phys., 7, 014
Hamaus, N., Pisani, A., Choi, J.-A., Lavaux, G., Wandelt, B. D., & Weller, J. 2020, J. Cosmology Astropart. Phys., 2020, 023
Hammer, F., Yang, Y. B., Wang, J. L., Ibata, R., Flores, H., & Puech, M. 2018, MNRAS, 475, 2754
Han, J. J., et al. 2022, AJ, 164, 249
Hart, M. 2019, PASP, 131, 015003
Hayashi, H., & Chiba, M. 2006, PASJ, 58, 835
Hayashi, K., Chiba, M., & Ishiyama, T. 2020, ApJ, 904, 45
Hayden, M. R., et al. 2015, ApJ, 808, 132
Helmi, A., Babusiaux, C., Koppelman, H. H., Massari, D., Veljanoski, J., & Brown, A. G. A. 2018, Nature, 563, 85
Hikage, C., et al. 2019, PASJ, 71, 43
Hirai, Y., Beers, T. C., Chiba, M., Aoki, W., Shank, D., Saitoh, T. R., Okamoto, T., & Makino, J. 2022, MNRAS, 517, 4856
Hirai, Y., Kirby, E. N., Chiba, M., Hayashi, K., Anguiano, B., Saitoh, T. R., Ishigaki, M. N., & Beers, T. C. 2024, arXiv e-prints, arXiv:2405.05330
Ho, S. H., & Martin, C. L. 2020, ApJ, 888, 14
Horowitz, B., Lee, K.-G., White, M., Krolewski, A., & Ata, M. 2019, ApJ, 887, 61
Hui, L., Ostriker, J. P., Tremaine, S., & Witten, E. 2017, Phys. Rev. D, 95, 043541
Ibata, R., et al. 2021, ApJ, 914, 123
Ivanov, M. M., Philcox, O. H. E., Cabass, G., Nishimichi, T., Simonović, M., & Zaldarriaga, M. 2023, Phys. Rev. D, 107, 083515
Jullo, E., et al. 2019, Astron. Astrophys., 627, A137
Kaiser, N. 2004, Pan-STARRS Technical Report, PDSC-002-010-XX
Kashino, D., et al. 2017, ApJ, 843, 138
Kauffmann, G., White, S. D. M., Heckman, T. M., Ménard, B., Brinchmann, J., Charlot, S., Tremonti, C., & Brinkmann, J. 2004, MNRAS, 353, 713
Kereš, D., Katz, N., Weinberg, D. H., & Davé, R. 2005, MNRAS, 363, 2
Kirby, E. N., Cohen, J. G., Smith, G. H., Majewski, S. R., Sohn, S. T., & Guhathakurta, P. 2011, ApJ, 727, 79
Kirby, E. N., Guhathakurta, P., Bolte, M., Sneden, C., & Geha, M. C. 2009, ApJ, 705, 328
Kirby, E. N., et al. 2010, ApJS, 191, 352
Kobayashi, C., Bhattacharya, S., Arnaboldi, M., & Gerhard, O. 2023, ApJL, 956, L14
Kobayashi, Y., Nishimichi, T., Takada, M., & Miyatake, H. 2022, Phys. Rev. D, 105, 083517
Komatsu, E., et al. 2014, Progr. Theor. Exp. Phys., 2014, 06B102
Komiyama, Y., et al. 2018, ApJ, 853, 29
Kraljic, K., et al. 2018, MNRAS, 474, 547
Kreisch, C. D., Pisani, A., Carbone, C., Liu, J., Hawken, A. J., Massara, E., Spergel, D. N., & Wandelt, B. D. 2019, MNRAS, 488, 4413
Kreisch, C. D., Pisani, A., Villaescusa-Navarro, F., Spergel, D. N., Wandelt, B. D., Hamaus, N., & Bayer, A. E. 2022, ApJ, 935, 100
Kriek, M., et al. 2015, ApJS, 218, 15
Kubota, K., Inoue, A. K., Hasegawa, K., & Takahashi, K. 2020, MNRAS, 494, 3131
Kurucz, R. L. 1993, Physica Scripta Volume T, 47, 110
Lacy, M., et al. 2021, MNRAS, 501, 892
Laigle, C., et al. 2018, MNRAS, 474, 5437
Lamareille, F., et al. 2009, A&A, 495, 53
Lan, T.-W., & Mo, H. 2018, ApJ, 866, 36
Laporte, C. F. P., Koposov, S. E., & Belokurov, V. 2022, MNRAS, 510, L13
Le Fèvre, O., et al. 2005, A&A, 439, 845
Leja, J., Carnall, A. C., Johnson, B. D., Conroy, C., & Speagle, J. S. 2019, ApJ, 876, 3

Lesgourgues, J., & Pastor, S. 2006, Phys. Rep., 429, 307
Li, T. S., et al. 2017, ApJ, 844, 74
Li, X., et al. 2023, Phys. Rev. D, 108, 123518
Lilly, S. J., et al. 2007, ApJS, 172, 70
—. 2009, ApJS, 184, 218
Mackereth, J. T., et al. 2019, MNRAS, 489, 176
Madhavacheril, M. S., et al. 2024, ApJ, 962, 113
Maiolino, R., & Mannucci, F. 2019, A&A Rev., 27, 3
Maiolino, R., et al. 2020, The Messenger, 180, 24
Makiya, R., Kayo, I., & Komatsu, E. 2021, J. Cosmology Astropart. Phys., 2021, 095
Makiya, R., & Sunayama, T. 2022, J. Cosmology Astropart. Phys., 2022, 008
Malavasi, N., et al. 2017, MNRAS, 465, 3817
Mashchenko, S., Wadsley, J., & Couchman, H. M. P. 2008, Science, 319, 174
Massara, E., Villaescusa-Navarro, F., Viel, M., & Sutter, P. M. 2015, J. Cosmology Astropart. Phys., 2015, 018
Matsuoka, Y., et al. 2018, PASJ, 70, S35
Mauduit, J. C., et al. 2012, PASP, 124, 714
McMonigal, B., et al. 2016, MNRAS, 461, 4374
Miyatake, H., et al. 2022, Phys. Rev. D, 106, 083520
—. 2023, Phys. Rev. D, 108, 123517
Mo, H. J., Mao, S., & White, S. D. M. 1998, MNRAS, 295, 319
Momcheva, I. G., et al. 2016, ApJS, 225, 27
Murphy, M. T., Kacprzak, G. G., Savorgnan, G. A. D., & Carswell, R. F. 2019, MNRAS, 482, 3458
Murray, N., Quataert, E., & Thompson, T. A. 2005, ApJ, 618, 569
Muzzin, A., et al. 2013, ApJ, 777, 18
Navarro, J. F., Frenk, C. S., & White, S. D. M. 1997, ApJ, 490, 493
Nguyen, N.-M., Huterer, D., & Wen, Y. 2023, Phys. Rev. Lett., 131, 111001
Nidever, D. L., et al. 2024, Early Disk-Galaxy Formation from JWST to the Milky Way, 377, 115
Ogami, I., et al. 2024, arXiv e-prints, arXiv:2401.00668
Oguri, M., & Takada, M. 2011, Phys. Rev. D, 83, 023008
Okamoto, S., Arimoto, N., Tolstoy, E., Jablonka, P., Irwin, M. J., Komiyama, Y., Yamada, Y., & Onodera, M. 2017, MNRAS, 467, 208
Ostriker, J. P., & Steinhardt, P. 2003, Science, 300, 1909
Peacock, J. A., et al. 2001, Nature, 410, 169
Percival, W. J., et al. 2010, MNRAS, 401, 2148
Pichon, C., Pogosyan, D., Kimm, T., Slyz, A., Devriendt, J., & Dubois, Y. 2011, MNRAS, 418, 2493
Pisani, A., Sutter, P. M., Hamaus, N., Alizadeh, E., Biswas, R., Wandelt, B. D., & Hirata, C. M. 2015, Phys. Rev. D, 92, 083531
Pisani, A., et al. 2019, BAAS, 51, 40
Planck Collaboration et al. 2020, A&A, 641, A6
Plez, B. 2012, Turbospectrum: Code for spectral synthesis, Astrophysics Source Code Library, record ascl:1205.004
Prakash, A., et al. 2016, ApJS, 224, 34
Pullen, A. R., Alam, S., He, S., & Ho, S. 2016a, MNRAS, 460, 4098
Pullen, A. R., Hirata, C. M., Doré, O., & Raccanelli, A. 2016b, PASJ, 68, 12
Raichoor, A., et al. 2017, MNRAS, 471, 3955
Read, J. I., et al. 2021, MNRAS, 501, 978
Renaud, F., Agertz, O., Read, J. I., Ryde, N., Andersson, E. P., Bensby, T., Rey, M. P., & Feuillet, D. K. 2021, MNRAS, 503, 5846
Reyes, R., Mandelbaum, R., Seljak, U., Baldauf, T., Gunn, J. E., Lombriser, L., & Smith, R. E. 2010, Nature, 464, 256
Riess, A. G., Casertano, S., Yuan, W., Macri, L. M., & Scolnic, D. 2019, ApJ, 876, 85
Rousselot, P., Lidman, C., Cuby, J. G., Moreels, G., & Monnet, G. 2000, A&A, 354, 1134
Saito, S., de la Torre, S., Ilbert, O., Dubois, C., Yabe, K., & Coupon, J. 2020, MNRAS, 494, 199
Sawicki, M., et al. 2019, MNRAS, 489, 5202
Schaan, E., Krause, E., Eifler, T., Doré, O., Miyatake, H., Rhodes, J., & Spergel, D. N. 2017, Phys. Rev. D, 95, 123512
Schmidt, F. 2017, ArXiv e-prints, arXiv:1709.01544
Schmitt, A., et al. 2019, in Astronomical Society of the Pacific Conference Series, Vol. 521, Astronomical Data Analysis Software and Systems XXVI, ed. M. Molinaro, K. Shortridge, & F. Pasian, 398
Schroetter, I., et al. 2019, MNRAS, 490, 4368
Scoville, N., et al. 2007, ApJS, 172, 38
Silverman, J. D., et al. 2009, ApJ, 695, 171
—. 2015, ApJS, 220, 12
Singh, S., Alam, S., Mandelbaum, R., Seljak, U., Rodriguez-Torres, S., & Ho, S. 2019, Mon. Not. Roy. Astron. Soc., 482, 785
Somerville, R. S., & Davé, R. 2015, ARA&A, 53, 51
Sonnenfeld, A., Jaelani, A. T., Chan, J., More, A., Suyu, S. H., Wong, K. C., Oguri, M., & Lee, C.-H. 2019, A&A, 630, A71
Speagle, J. S., Steinhardt, C. L., Capak, P. L., & Silverman, J. D. 2014, ApJS, 214, 15
Spergel, D. N., & Steinhardt, P. J. 2000, Phys. Rev. Lett., 84, 3760
Steidel, C. C., Strom, A. L., Pettini, M., Rudie, G. C., Reddy, N. A., & Trainor, R. F. 2016, ApJ, 826, 159
Steidel, C. C., et al. 2014, ApJ, 795, 165
Steinhardt, C. L., et al. 2014, ApJL, 791, L25
Strom, A. L., Steidel, C. C., Rudie, G. C., Trainor, R. F., Pettini, M., & Reddy, N. A. 2017, ApJ, 836, 164
Sunayama, T., et al. 2020, J. Cosmology Astropart. Phys., 2020, 057
Sutter, P. M., Pisani, A., Wandelt, B. D., & Weinberg, D. H. 2014, MNRAS, 443, 2983
Takada, M., Komatsu, E., & Futamase, T. 2006, Phys. Rev. D, 73, 083520
Takada, M., et al. 2014, PASJ, 66, R1
Tamfal, T., Mayer, L., Quinn, T. R., Babul, A., Madau, P., Capelo, P. R., Shen, S., & Staub, M. 2022, ApJ, 928, 106
Timlin, J. D., et al. 2016, ApJS, 225, 1
Troxel, M. A., et al. 2018, Phys. Rev. D, 98, 043528
Tumlinson, J., Peeples, M. S., & Werk, J. K. 2017, ARA&A, 55, 389
Valentino, F., et al. 2017, MNRAS, 472, 4878
Valenzuela, O., Rhee, G., Klypin, A., Governato, F., Stinson, G., Quinn, T., & Wadsley, J. 2007, ApJ, 657, 773
Vasiliev, E. 2023, Galaxies, 11, 59
Vincenzo, F., & Kobayashi, C. 2020, MNRAS, 496, 80
Vogelsberger, M., et al. 2014, MNRAS, 444, 1518
Walker, M. G., & Peñarrubia, J. 2011, ApJ, 742, 20
Wang, T., et al. 2016, ApJ, 816, 84
Wardana, M. D., Chiba, M., & Hayashi, K. 2024, arXiv e-prints, arXiv:2404.12671
Wechsler, R. H., & Tinker, J. L. 2018, ARA&A, 56, 435
Weisz, D. R., Dolphin, A. E., Skillman, E. D., Holtzman, J., Gilbert, K. M., Dalcanton, J. J., & Williams, B. F. 2014, ApJ, 789, 147
Wild, V., Heckman, T., & Charlot, S. 2010, MNRAS, 405, 933
Wojno, J. L., et al. 2023, ApJ, 951, 12
Wyse, R. F. G. 2001, in Astronomical Society of the Pacific Conference Series, Vol. 230, Galaxy Disks and Disk Galaxies, ed. J. G. Funes & E. M. Corsini, 71–80
York, D. G., et al. 2000, AJ, 120, 1579
Zahid, H. J., Kewley, L. J., & Bresolin, F. 2011, ApJ, 730, 137
Zhang, G., Li, Z., Liu, J., Spergel, D. N., Kreisch, C. D., Pisani, A., & Wandelt, B. D. 2020, Phys. Rev. D, 102, 083537
Zhang, P., Liguori, M., Bean, R., & Dodelson, S. 2007, Phys. Rev. Lett., 99, 141302

PFS COLLABORATION

Principal Investigator (PI)

Hitoshi Murayama — Kavli IPMU

Co-Principal Investigator (Co-PI)

Naoyuki Tamura — NAOJ

Project Manager/Project System Engineer

Naoyuki Tamura — NAOJ

Survey Scientist

Kiyoto Yabe — NAOJ

Co-Chairs of the PFS Survey Committee

Richard S Ellis — UCL
Masahiro Takada — Kavli IPMU

Co-Chairs of the PFS Science Working Groups

PFS Cosmology WG

Tomomi Sunayama — Nagoya U.
ChangHoon Hahn — Princeton U.

PFS Galactic Archaeology WG

Masashi Chiba — Tohoku U.
Judith Cohen — Caltech
Evan Kirby — U. of Notre Dame
Rosemary Wyse — JHU

PFS Galaxy Evolution WG

Rachel Bezanson — U. of Pittsburgh
Jenny Greene — Princeton U.
Chiaki Kobayashi — U. Hertfordshire
Khee-Gan Lee — Kavli IPMU
Masami Ouchi — NAOJ/U. Tokyo
John Silverman — Kavli IPMU

PFS Steering Committee

S. Arnouts (LAM), Y.-T. Lin (ASIAA), R. S. Ellis (UCL),

T. Heckman (JHU), Y.-.P. Jing (SJTU), E. Komatsu (MPA), D. Marchesini (Tufts U.), H. Murayama (Kavli IPMU), M. Seiffert (JPL/Caltech), L. Sodre Jr. (U. São Paulo), M. Strauss (Princeton), M. Takada (Kavli IPMU), M. Oguri (Chiba U./Subaru Advisory Committee chair), S. Miyazaki (NAOJ/Director of the NAOJ Hawaii Observatory)

Members in the PFS Collaboration

K. Adachi[1], H. Aihara[2,3], M. Akiyama[1], H. Algera[4], S. S. Ali[5], A. Allaoui[6], A. Amon[7], M. Ando[8], J. Arita[3], S. Arnouts[6], G. M. Azevedo[9], C. L. Bennett[10], M. Bethermin[6,11], D. F. Braun[12], V. L. Brun[6], D. Burgarella[6], J. Burnham[13], N. Caplar[14], M. M. Carneiro[71], M. A. Carr[7], P.-Y. Chabaud[6], T.-C. Chang[12,13], A. Chen[2,3], C.-C. Chen[15], Z. Chen[31], Y.-K. Chiang[15], M. Chiba[1], A. L. Chies-Santos[9], R. C. Y. Chou[15], S. Christian[6], L. Clotilde[16], A. P. Cooper[17], S. de la Torre[6], A. C. de Oliveira[18], C. M. de Oliveira[19], L. S. de Oliveira[18], O. Doré[12,13], R. S. Ellis[20], T. Enßlin[21], M. Fabricius[22], R. C. Fernandes[23], D. Ferreira[18], E. G. M. Ferreira[2,3], C. Filion[10], C. Fisher[24], K. Fukushima[25], A. L. Fur[7], H. Furusawa[8], A. Genina[21], R. Gerasimov[26], S. Gezari[10], T. Goto[17], C. Gouin[16], A. D. Goulding[7], J. Gracia-Carpio[22], J. Gross[12], J. E. Gunn[7], R. Hada[27], C. Hahn[7], Y. Harikane[28], N. P. Hathi[29], G. R. Hauschild-Roier[9], Kohei Hayashi[30], Kota Hayashi[2,3], T. Heckman[10], C. Hernández-Aguayo[21], Y. Hirai[1], W. Hong[31], B. Horowitz[2,3], H. Hoshi[32], B.-C. Hsieh[15], K. Ichikawa[25], R. Ikeda[33], O. Ilbert[6], M. Imanishi[8], A. K. Inoue[25], K. Ishida[1], R. Ishikawa[1], T. Ishiyama[34], K. Ito[32], K. Iwasawa[35], C. K. Jespersen[7], H.-Y. Jian[15], L. Jiang[36], Y.-P. Jing[31], S. D. Johnson[37], K. Kakiichi[38], J. Kang[39], N. Kashikawa[32], G. Kauffmann[21], I. Kayo[40], S. Kikuta[32], M. Kimura[15], M. King[12], E. N. Kirby[26], T. Kirihara[41], T. Kiyota[42], C. Kobayashi[43], S. Kobayashi[44], T. Kodama[1], M. Kokubo[8], E. Komatsu[21], Y. Komiyama[45], S. Koshida[5], Y. Koyama[5], K. Kraljic[46], M. Kubo[1], H. Kusakabe[8], P. B. Kuzma[8], R. Laishram[1], T.-W. Lan[46], N. Laporte[6], H. A. N. Le[39], K. Lee[1], J. Leja[47], C. Li[48], Q. Li[31], X. Li[31], Y. Liang[28], V. S. M. Lima[18], L. Lin[15], Y.-T. Lin[15], Y. Lin[31], H.-H. Ling[15], J. Liu[2,3], X. Liu[49], Y. Luo[10], L. A. MacArthur[7], P. H. Mao[12], D. Marchesini[50], N. F. Martin[46], M. Matsubara[44], S. Matsui[32], A. Matsumoto[28], N. Matsumoto[1], Y. Matsuoka[44], J. McCullough[7], P. Melchior[7], T. Melia[2,3], H. Miyatake[51,52], R. Momose[53], R. Monteiro-Oliveira[15], J. Moon[21], C. Morantz[12], K. Morihana[8], T. Morishima[8], Y. Moritani[8] K. Motohara[8], H. Murayama[2], J. Myles[7], K. Nagamine[54], T. Nagao[44], K. Nakajima[8], S. Nakano[2,3], K. Nakashima[52], Y. Nan[2,3], T. Nishimichi[55], A. J. Nishizawa[56], K. Nomoto[2,3], C. A. Norman[10], K. Nose[2], I. Ogami[42], K. Ogura[57], N. Okabe[4], H. Okada[58], S. Okamoto[5], Y. Oku[59], T. Okumura[15], Y. Ono[28], M. Onodera[5], M. Onoue[2,3], K. Osato[34], M. Ouchi[3,8], R. Overzier[60], T. Patrice[6], U.-L. Pen[15], M. M. Pieri[6], A. Pisani[6], P. A. Price[7], T.-S. Pyo[5], C. Qin[39], M. Reinecke[21], W. Ren[39], L. Robbins[50], J. A. Rosa[18], K. Rowlands[10], S. Saga[51], S. Saito[61], A. Sajina[50], K. Sato[42], C. Schimd[6], K. C. Schlaufman[10], F. Schmidt[21], A. Schmitt[6], B. R. Scott[62], M. Seiffert[12,13], M. D. Seiffert[12,13], D. J. Settob[7], Z. Shao[31], J. Shi[2,3], K. Shibata[44], R. Shimakawa[25], K. Shimasaku[32], S. Shimizu[32], Y. Shirasaki[8], H. Siddiqui[7], J. C. Siegel[7], L. G. Silva[19], L. Sodré Jr.[19], T. Storchi-Bergmann[9], M. A. Strauss[7], A. L. Strom[62], Y. Sugahara[25], N. Sugiyama[8], T. Sunayama[63], T. Suzuki[2,3], Y. Suzuki[1], K. Tadaki[64], M. Takada[2,3], Y. Takeda[32], S.-I. Tam[15], N. Tamura[5], T. Tamura[65], M. Tanaka[8], T. S. Tanaka[2,3], T. Taniguchi[2,3], L. A. M. Tasca[6], R. Terasawa[2,3], T. Terawaki[2,3], Y. Toba[8], A. Tokiwa[2,3], N. Tominaga[8], V. L. Torre[50], J. Toshikawa[58], L. Tresse[6], J. R. Trump[66], H. Uchiyama[8], Y. Ueda[67], H. Umeda[28], H. Umehata[52], K. Umetsu[15], D. Vibert[6], M. C. Vicentin[19], B. Vijarnwannaluk[15], Jialai Wang[39], Jiaqi Wang[31], S.-Y. Wang[15], W.-H. Wang[15], Yirong Wang[31], Y-J. Wang[15], Yuting Wang[68], M. D. Wardana[1], K. E. Whitaker[69], S. White[21], L. Wu[39], P.-F. Wu[46], R. Xia[39], X. Xu[62], Y. Xu[28], Y. Xue[39], K. Yabe[5], S. Yamada[70], Y. Yamada[32], M. Yamazaki[2,3], H. Yanagisawa[28], X. Yang[31], N. Yasuda[2,3], J. Yokoyama[2,3], N. Yoshida[2,3], T. Yoshida[44], S. Yuan[68], K. Zaidi[50], N. Zakamska[10], H. Zhang[8], J. Zhang[31], T. Zhang[32], Y. Zhang[8], Z. Zhang[54], G.-B. Zhao[68], H.-M. Zhu[68], Y. Zu[31]

[1]Tohoku University, Japan
[2]Kavli IPMU (WPI), Japan
[3]The University of Tokyo, Japan
[4]Hiroshima University, Japan
[5]Subaru Telescope, NAOJ, Japan
[6]Laboratoire d'Astrophysique de Marseille, France
[7]Princeton University, USA
[8]National Astronomical Observatory of Japan (NAOJ), Japan
[9]Universidade Federal do Rio Grande do Sul, Brazil
[10]Johns Hopkins University, USA
[11]Université de Strasbourg, France
[12]Jet Propulsion Laboratory, USA
[13]California Institute of Technology, USA
[14]University of Washington, USA
[15]Academic Sinica Institute of Astronomy and Astrophysics (ASIAA), Taiwan
[16]Sorbonne Université, France
[17]National Tsing Hua University, Taiwan
[18]Laboratório Nacional de Astrofisica, Brazil
[19]Universidade de Sao Paulo, Brazil
[20]University College London, UK
[21]Max Planck Institute for Astrophysics, Germany
[22]Max Planck Institute for Extraterrestrial Physics, Germany
[23]Universidade Federal de Santa Catarina, Brazil
[24]University of Colorado Boulder, USA
[25]Waseda University, Japan
[26]University of Notre Dame, USA
[27]The Ohio State University, USA
[28]Institute for Cosmic Ray Research, The University of Tokyo, Japan
[29]Subaru Telescope, Japan
[30]National Institute of Technology, Sendai College, Japan
[31]Shanghai Jiao Tong University, China
[32]The University of Tokyo, Japan
[33]The Graduate University for Advanced Studies (SOKENDAI), Japan
[34]Chiba University, Japan
[35]Universitat de Barcelona, Spain
[36]Peking University, China
[37]University of Michigan, USA
[38]University of Copenhagen, Denmark
[39]University of Science and Technology of China, China
[40]Tokyo University of Technology, Japan
[41]Kitami Institute of Technology, Japan
[42]SOKENDAI, NAOJ, Japan
[43]University of Hertfordshire, UK
[44]Ehime University, Japan
[45]Hosei University, Japan
[46]National Taiwan University, Taiwan
[47]The Pennsylvania State University, USA

[48]Tsinghua University, China
[49]University of Illinois at Urbana Champaign, USA
[50]Tufts University, USA
[51]Kobayashi-Maskawa Institute for the Origin of Particles and the Universe, Nagoya University, Japan
[52]Nagoya University, Japan
[53]The Observatories of the Carnegie Institution for Science, USA
[54]Osaka University, Japan
[55]Kyoto Sangyo University, Japan
[56]Gifu Shotoku Gakuen University, Japan
[57]Kobe City College of Technology, Japan
[58]The University of Hyogo, Japan
[59]Zhejiang University, China
[60]Observatório Nacional/MCTI, Brazil
[61]Missouri University of Science and Technology, USA
[62]Northwestern University, USA
[63]The University of Arizona, USA
[64]Hokkai-Gakuen University, Japan
[65]Institute of Space and Astronautical Science, Japan
[66]University of Connecticut, USA
[67]Kyoto University, Japan
[68]National Astronomical Observatories, Chinese Academy of Sciences (NAOC), China
[69]University of Massachusetts Amherst, USA
[70]RIKEN, Japan
[71]Instituto Nacional de Pesquisas Espaciais (INPE), Brazil